Università degli studi di Genova

Doctorate in Sciences and Technologies of Chemistry and Materials

Curriculum: Materials Science and Technology

(XXXV cycle)

Inter-layer adhesion in material extrusion 3D printing: effect of processing and molecular variables

Andrea Costanzo

Tutor: Prof. Dario Cavallo

Table of contents

1 SUMMARY AND OUTLINE

1.1 Summary

3D-printing technology is a layer-by-layer process that is now used in personal and commercial production where prototyping and customization are required. This technique exploits the principle of additive manufacturing (AM) for making three-dimensional complex shape solid objects from a digital file. 3D printing allows fabricating products with complex geometries that would be impossible or very challenging to implement with conventional techniques.[1] The most popular 3- D printing technique is the so called Fused Deposition Modelling (FDM): a solid filament is drawn into a printer nozzle, heated to a temperature where the polymer flows readily, then extruded layer-by-layer onto a build plate.

One of the negative characteristics of 3D printing products is that they are weaker than those obtained using traditional techniques. In particular, it is observed that the overall strength is much smaller when the load is applied in the printing direction with respect to the perpendicular direction. This means that the weak point of the 3D printing products is the contact surface between adjacent layers.[2] The inter-layer welding formation mechanism occurs by diffusion between adjacent chains in different layer, with the eventual formation of entanglements between them. In the case of amorphous polymers, the inter-chain diffusion process is opposed by the rapid temperature decrease and ceases when the glass transition temperature is reached. In the case of semi-crystalline polymers, the welding efficiency is instead linked to the quantity of polymer that managed to diffuse before crystallization occurs.

Fused deposition modeling (FDM) offers many advantages over conventional manufacturing methods, but it is limited by the low number of available materials.

The (3D)-printability of polymers has so far only been determined empirically. In order to derive general principles that control polymer 3D printing and allow a good interlayer welding, a set of data on polymer materials with widely different characteristics would be required. To this purpose, this project aims to study how different molecular features, like molecular weight, chain composition and crystallinity can affect the final quality of the weld, with particular reference to the final mechanical properties.

1.2 Outline

Chapter 2 provides an introduction to 3D printing, with particular attention to filament deposition technology. Subsequently, the phenomenon of interlayer bond formation and the drawbacks associated with it are introduced. Finally, some examples in the literature of the in-situ measurement of the crystallization process during 3D printing are reported.

In Chapter 3 all the materials studied in the various chapters are reported and all the used characterization techniques are presented.

In the fourth chapter, we observe experimentally residual alignment trapped into a single-filament wall. Furthermore, this residual alignment is found to be localized only at filament-filament interfaces (welds). Residual alignment is quantified for varying nozzle temperature and print speed using the molecularly-aware model of McIlroy et al.[3,4] By combining these model results, from a collaboration with the University of Lincoln, with experimental measurements of the weld toughness (measured at the University of Genova), we confirm that reduced weld strength is due to orientation of the polymer molecules that occurs during flow through the nozzle and deposition onto the build plate, rather than poor inter-diffusion. Furthermore, we propose that residual alignment pertains to a partially entangled polymer network[5] and thus can be directly correlated to weld toughness[4], in close agreement with the experimental data.

In Chapter 5, we show that weld strength increases with decreasing average molecular weight, contrary to common observations in specimens processed in more traditional ways, e.g., by compression molding. Using a combination of synchrotron infra-red polarization modulation microspectroscopy measurements and continuum modelling (always from a collaboration with the University of Lincoln, UK), it is demonstrated how residual molecular anisotropy in the weld region leads to poor strength and how it can be eradicated by decreasing the relaxation time of the polymer. This is achieved more effectively by reducing the molar mass than by the usual approach of attempting to govern the temperature in this hard to control non-isothermal process.

In Chapter 6, we investigate how the change is chemistry may affect the inter-diffusive welding process inherent to achieving structural integrity in Material Extrusion (MatEx) in the case of two commercial co-polyesters. Although this change in chemistry modifies the temperature-

dependent rheological behaviour in ways that are expected to be detrimental to the weld strength, by employing a molecularly-aware modelling approach we propose that the polymer chain stiffness is fundamental to ensuring that residual molecular anisotropy in the weld region is limited.

In Chapter 7, we propose to study the crystallization kinetics of two different polyamides used for FDM 3D printing and to link it to the microstructure and properties obtained during FDM. The kinetics are studied both in isothermal and fast cooling conditions, thanks to a home-built device which allows mimicking the quenching experienced during filament deposition. The temperature history of a single filament is then determined by mean of a micro-thermocouple and the final crystallinity of the sample printed in a variety of conditions is assessed by differential scanning calorimetry. It is found that the applied processing conditions always allowed for the achievement of the maximum crystallinity, although in one condition the polyamide mesomorphic phase possibly develops. Despite the degree of crystallinity is not a strong function of printing variables, the weld strength of adjacent layers shows remarkable variations. In particular, a decrease of its value with printing speed is observed, linked to the probable development of molecular anisotropy under the more extreme printing conditions.

Chapter 8 focuses on the implementation of a simple optical setup to follow the crystallization process in-situ. The new setup exploits light scattering generated during filament deposition and cooling. To this purpose, the beam scattered by a growing 3D printed wall geometry is collected on a semi-transparent screen during the deposition for both amorphous polylactide and a semicrystalline polyamide copolymer. While the amorphous polymer scatters light anisotropically and generates a vertical scattering pattern, the semicrystalline polyamide produces isotropic scattering. Moreover, the kinetics of scattering intensity increase follows closely that of filament deposition in the case of polylactide. Instead, it strongly deviates from that for the semicrystalline polyamide. These pieces of evidence suggest that simple light scattering measurements, which are quickly and cost-effectively implemented on a lab-scale, can be further developed to allow a better understanding of polymer structuring phenomena in the highly non-equilibrium conditions of 3D printing.

Finally, in Chapter 9, the main achievements of the conducted experimental research are summarized.

2 INTRODUCTION

2.1 Additive manufacturing

Additive manufacturing (AM), also referred to as three-dimensional (3D) printing, is a group of emerging technologies that create objects based on computer-aided design (CAD) models by adding materials in a layer-by-layer process.[6–8] More specifically, AM is defined by the ISO/ASTM 52900 terminology standard as 'a process of joining materials to make parts from 3D model data, usually layer upon layer, as opposed to subtractive manufacturing and formative manufacturing methodologies'[9]. First introduced in the 1980s to meet the highly specialized needs of model making and rapid prototyping (RP), additive manufacturing (AM) also known as 3D printing has over time established itself as a versatile methodology platform for design computer aided (CAD) and rapid manufacturing.[10] The greatest advantages of additive manufacturing are the freedom of design and customization, allowing the creation of complex geometries that would be impossible to obtain with the constraints imposed by subtractive and formative manufacturing,[11] together with minimum material wastage and reasonable production speed.[12,13] A comparison of subtractive, additive, and formative manufacturing techniques is shown in Figure 2.1.[10]

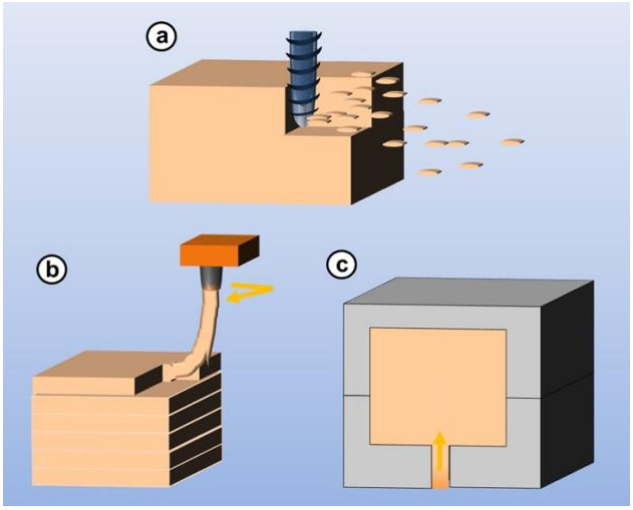

Figure 2.1. Comparison of (a) subtractive, (b) additive, and (c) formative manufacturing techniques.[10]

Figure 2.2 shows an example, schematizing the concept of AM in the simple case of a specimen in the shape of a coffee cup. At first, CAD software are used to create the virtual object of the required shape. The file containing the object is subsequently imported into special programs to be digitally sliced. Objects with overhanging portions (i.e., the coffee mug handle) are designed with temporary support structures to prevent collapse during the build process. Following slicing, the software consequently acquires the spatial coordinates of the object, which will then be used for the correct coordination of the printer motors. Normally, the thickness of the layer can be varied in a range from 500 up to 15 µm.

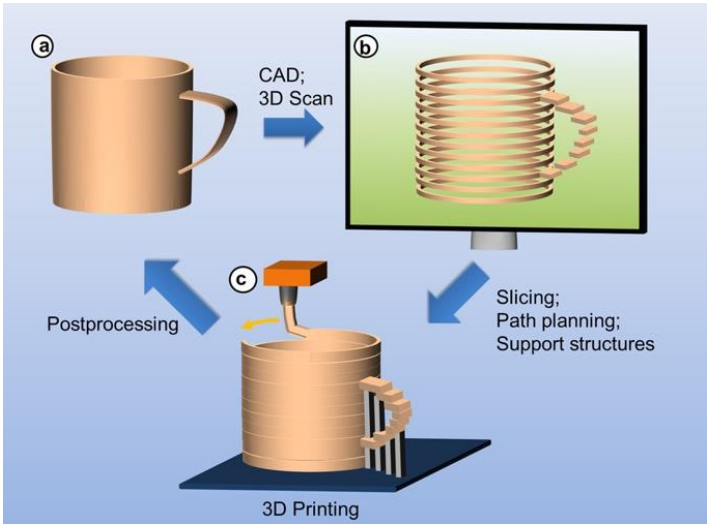

Figure 2.2. Basic principles of additive manufacturing. (a) Design of a model and subsequent transformation into digital format with the use of CAD software; (b) Slicing of virtual model into layered data, insertion of support structures and preparation of instructions to be sent to the printing device; (c) Additive manufacturing of model or product, for example, by melt extrusion, and eventual postprocessing to remove typical artifacts, including support structures and surface roughness due to staircase effects.[10]

The scientific and technological impact of AM has steadily increased since the first commercial instruments were introduced. Figure 2.3 clearly highlights, in fact, how the annual number of scientific publications and patents from 1985 to 2016 using the terms “additive manufacturing” and “rapid prototyping” has been, and continues to be, in great growth over the time. As examples, some of the books and reviews published in this period are cited here.[14–18] With the growing interest in additive manufacturing, at the same time bioprinting (based on AM) has witnessed a comparatively impressive increase in patents and publications over the last 25

years, with a growth that is expected to continue and may in the near future reach the levels of AM.

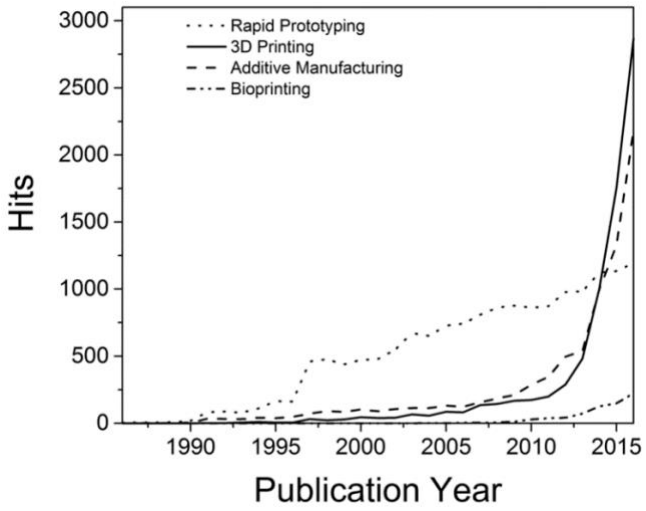

Figure 2.3. Research interest in rapid prototyping, 3D printing, additive manufacturing and bioprinting, as indicated by the number of hits per annum for the respective terms (data from Web of Science, accessed July 27, 2017).[10]

In recent years, the overall market situation for AM was characterized by significant growth rates with revenues from services as well as products which surpassed the value of 5 billion USD in 2015[19] (Figure 2.4). This significant growth spurred a lot of interest in AM-related activities, and major players in the manufacturing industry (aerospace, energy, automotive, consumer products, and medical/dental) have started activities in the field. AM is currently able to fabricate parts made of metals, polymers, and ceramics. For example, as indicated in Figure 2.5, the global additive manufacturing market size for North America was valued at USD 13.84 billion in 2021 and is expected to expand at a compound annual growth rate (CAGR) of 20.8% from 2022 to 2030.[20] Interestingly, the largest fraction of these material sales still goes into photopolymers, powders for laser sintering[21] and polymer filaments for fused deposition modeling, while in 2016 AM metals were sold for a value of only 127 million USD. Polymers are therefore clearly the most widely used material class for AM.

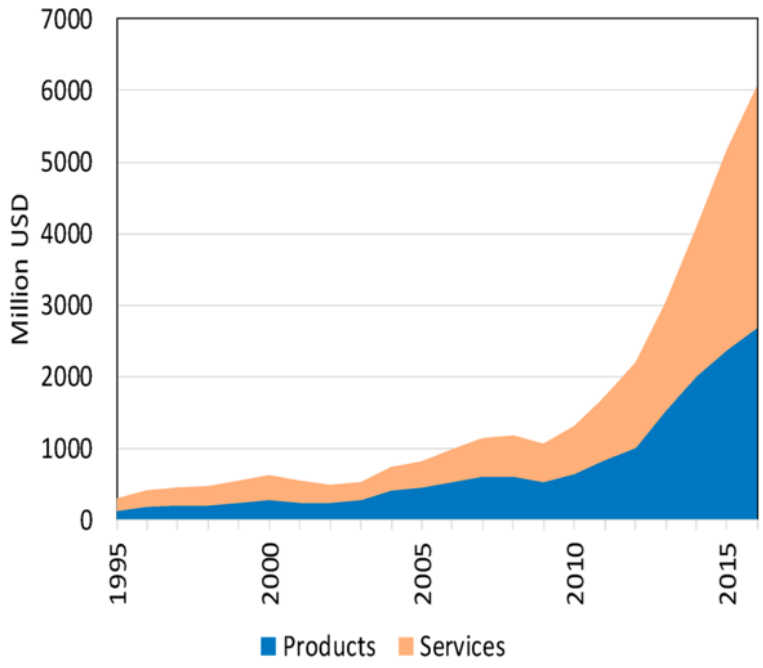

Figure 2.4. Worldwide revenues from AM products and services between 1995 and 2016.

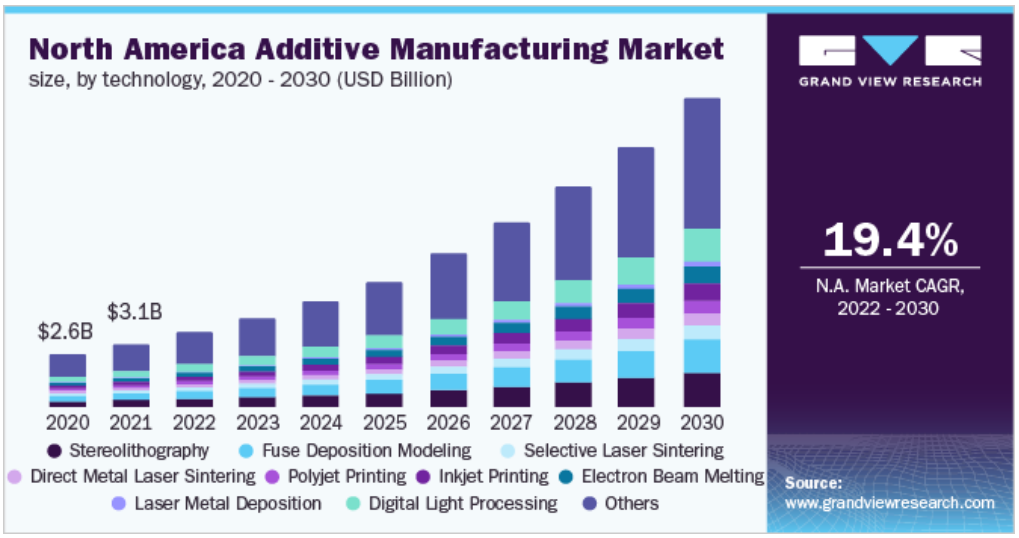

Figure 2.5. Additive manufacturing market size for North America from 2020 to 2030.[20]

Clearly, the cost effectiveness of using additive manufacturing is closely linked to the quantity of parts and the speed with which they are produced. Although, in fact, the technology is not suitable for use in series production, it far exceeds the more traditional subtractive techniques for applications with a high level of individuality. For some clinical applications, such as osteoplasty, dentistry and orthodontics, precise fit implants or supports are often produced by

AM based directly on patients' tomographic data.[22–26] Further fields with commercial relevance include architecture, urban development, and jewelry.[27,28]

With the increasingly widespread use of additive manufacturing, the need for increasingly specific prototypes and the requests for better final performance also increase[29]. However, there are still several shortcomings regarding this technology, and it is on the latter that much of the current research is focusing. The first drawback concerns the production speed: in fact, although AM allows to reduce the time necessary for the validations of the project and allows the production of functional prototypes already in the early stages of development, it remains a production technique that is still relatively slow compared to those mass production, such as injection molding. This aspect makes additive manufacturing suitable for applications that take advantage of its customization flexibility, but makes it currently inadequate for use on an industrial scale. Research to broaden the scope in the future ranges from advanced path planning procedures for SLAs in the 1990s to the development of continuous production of liquid interfaces (CLIP)[14,30].

With the progress of AM technology, it would have been expected to be able to obtain products with performances equal to or superior to those obtained with traditional subtractive and formative techniques. However, in most cases the products obtained from AM exhibit worse mechanical properties. Depending on the specific process employed, this weakness may be due to a limited choice of materials suited for a process (e.g., photocurable vinyl- or epoxy-functional oligomers for photo-polymerization in the case of SLA)[31] or to an unavoidable porosity of parts derived from powder bed fusion or material extrusion.[32,33] Furthermore, given the layer-by-layer deposition process, the artifacts often have anisotropic mechanical properties, with a border region between adjacent layers in which all residual stresses accumulate in applications where good mechanical strength is essential[34]. For example, in the case of FDM technology it has been shown that the anisotropy and therefore final mechanical properties are strictly dependent on the material used and on the process conditions.[35] Anisotropy also occurs in the case of AM lithography, where however it can be mitigated with postcuring treatments.[36] In any case, as shown by recent research, the use of composite materials could represent a solution for improving the final mechanical properties of printing products[37]. Another aspect to consider and which depends on both the specific technique and the material is that of spatial resolution. A low resolution can, in fact, lead to poor quality and functionality of the final products.

Another limitation of AM is the ability to process different materials simultaneously. Commercial multicolor 3D printers have become increasingly common, but are only able to

print different colored filaments of the same type of material.[38] Conversely, processing two or more different materials at the same time is more complicated due to differences in reactivity, thermal and rheological properties and possible incompatibility between the materials themselves.[39]

Almost all additive manufacturing techniques have been modified to allow multimaterial AM (MMAM), but only some of them have been commercialized. For example, MMAM is possible for vat photopolymerization by using multiple vats and transferring the object between vats during building[40,41] and even in powder bed AM by changing powder material for another during printing[42]. However, MMAM techniques are limited due to contamination issues, slow transfer from one material to another, and above all by the fact that material exchange is possible only between layers (1D multimaterial) and not within layers (3D multimaterial). Material jetting MMAM based on drop on demand (DOD) technology, however, allows for rapid exchange between building materials at every 1D point within a 3D printing job.[43] In general, these MMAM techniques plays an important role in AM for bioprinting and applications in medicine and life sciences.

One of the most promising applications of AM concerns the field of personalized medicine where, using information from tomographic images (X-rays, MRI, etc.), it is possible to create customized objects for each patient. AM is in fact already used in surgical planning, for the production of prostheses, in dentistry and for tissue engineering.[44–48]

The use of AM for applications of this type requires particular attention both for the materials and for the technique to be used. For example, acrylates, which are commonly used in all lithographic AM methods (SLA, Polyjet), are cytotoxic but can be replaced by less reactive methacrylates or thiol-ene systems[49,50].

The same PLA, used extensively in FDM and in any case approved by the FDA for human implantation, is not adequate due to its poor mechanical properties[51]. Moreover, FDM is a melt extrusion process and does not allow incorporation of living cells or growth factors. An alternative solution is given by bioplotting, an AM method performing at room temperature with which it is possible to manipulate hydrogels containing cells and growth factors.[52,53]

Even in this case, however, especially using a multi-material approach, the precise control of temperature and other process parameters is still not straightforward.

According to the ASTM International Committee F42 on Additive Manufacturing Technology, we can distinguish between seven types of AM techniques[54,55], including material extrusion (ME), material jetting (MJ), binder jetting (BJ), sheet lamination (SL), vat photo polymerization (VP), powder bed fusion (PBF) and directed energy deposition (DED)[8]. Each AM method has its own characteristics in terms of speed, resolution and cost, thus offering different choices for users[56].

Material extrusion is a manufacturing process in which material is heated inside a high temperature extruder and then distributed through a nozzle. Fused Deposition Modeling (FDM), Fused Filament Fabrication (FFF), 3D Dispensing, and 3D Bioplotting fall into this category.

Material jetting is an additive manufacturing process in which droplets of build material (such as photopolymer or thermoplastic materials) are dropped in a selected area and cured using UV light to produce a layer.[57] Systems based on inkjet-printing fall into this category.

Binder jetting is a process in which a liquid bonding agent (binder) is selectively deposited a powder bed to produce green parts with complex 3D structures.[58]

Sheet lamination is an additive manufacturing process in which sheets of material are bonded together to form an object.

Vat photopolymerization is an additive manufacturing process in which liquid photopolymer in a vat is selectively cured by light-activated polymerization. Many of the lithography-based AM approaches (e.g., multiphoton polymerization (2PP)[59], digital light processing (DLP)[60,61], and stereolithography (SLA)[62,63]) can be grouped into this category.

Powder bed fusion is an additive manufacturing process in which thermal energy, provided by a laser or an electron beam) selectively fuses regions of a powder bed. Selective laser sintering (SLS)[64] and electron beam machining (EBM) fall into this category. These processes are used for metals as well as polymers.

Directed energy deposition (DED) is an additive manufacturing process in which focused thermal energy is used to fuse materials by melting as they are being deposited. This process is currently only used for metals.[65,66]

2.2 Material extrusion: fused deposition modeling

Fused Filament Fabrication or Material Extrusion Additive Manufacturing (MEAM) was patented under the registered trademark Fused Deposition Modeling (FDM) by Scott Crump

and his company Stratasys, Inc. in 1989[1] and it is currently one of the most widely used and fastest growing AM techniques. As with all other additive manufacturing techniques, the manufacturing process begins with the production of a 3D model, obtained using CAD software or from 3D scans[67]. The 3D model, usually in the form of an .STL file, is converted using a preprocessing software which slices the 3D model into separate cross-sectional layers and defines the path that should be followed during printing. A file is then obtained containing all the instructions necessary for printing which can be sent to the FDM device.[57,68]

This technique uses as a feedstock a filament of thermoplastic polymer material that is pushed through a nozzle, heated to a temperature at which the polymer is able to flow, then extruded layer by layer onto a build plate (printing bed). A tripod moves the print nozzle in the horizontal plane (x-y direction) as the material is deposited. The gap between the nozzle and the bed corresponds to the thickness of the produced layer. When one layer is completed, the build plate is lowered in the vertical direction and the next layer is deposited on the one just finished. The molten material exiting the nozzle solidifies during cooling.[1,69]

A schematic representation of the working principle of the FDM process is reported in Figure 2.6 , which also shows some of the key process parameters that can be chosen or adjusted when using this technique.[70]

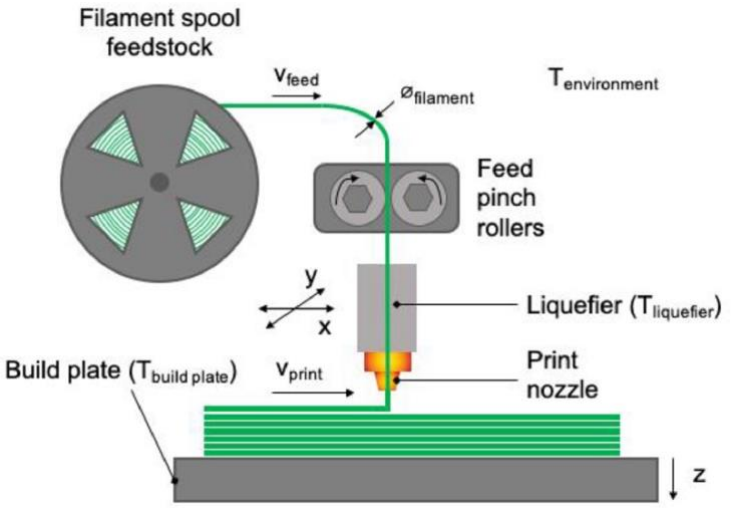

Figure 2.6. Example diagram of the operating principle of an FDM 3D printer and its main components.[70]

Compared to the other main polymer-based AM techniques, FFF is a rather cheap, simple and flexible process[11,71]. Moreover, it still provides the opportunity to process a much wider range of materials than, for example, SLA, which is limited to photopolymers only. Furthermore, the

energy consumption is also lower, in particular when compared to the SLS, whose operation requires the use of a high-power laser.[56]

FDM uses both amorphous and semi-crystalline thermoplastic polymers. The two most widely used and commercially widespread materials are acrylonitrile butadiene styrene (ABS) and polylactic acid (PLA), which are respectively amorphous and semi-crystalline.[10,68,72]

However, the continuous progress of additive manufacturing, with the transition from a simple prototyping technique to one for a real production of functional parts, has required the introduction on the market of new high-performance thermoplastic materials.[73] Specifically, these are engineered and high-performance materials based on semi-crystalline polymers, which however can have more complex processability windows than amorphous ones.[10]

In general, the crystallization process provides these materials with a typical lamellar morphology consisting of polymer chains packed parallel to each other with amorphous regions in between these lamellae. Generally, crystalline fraction provides increased toughness, wear resistance, strength and stiffness, although amorphous thermoplastics results better in impact resistance.[74,75] Moreover, whereas amorphous thermoplastics gradually soften when heated above the material's glass transition temperature, that corresponds to the transition from a glassy to a rubbery state, the crystals in semicrystalline polymers maintain their orderly microstructure up until their melting point at which they pass to the liquid state.[76,77]

For this reason, semicrystalline polymers can thus be employed at higher temperatures compared to amorphous thermoplastics, which typically experience a radical decrease in mechanical properties at glass transition temperature.[75,78] The presence of the crystalline structure also confers better chemical resistance and biocompatibility.[76]

The presence of these dense crystalline regions makes semicrystalline thermoplastics suffer far more severely from shrinkage upon cooling compared to amorphous polymers, which can lead to serious implications in the use of these polymers to produce functional parts that require a specific dimensional accuracy.[76–78]

The applications of semicrystalline feedstocks are mainly situated within three fields, including medicine, electronics, and aerospace and automotive. Polylactic acid (PLA), for example, offering the advantage that its degradation products naturally occur in the human body and can be resorbed again through the metabolic pathway, has already been used to produce scaffolds for tissue engineering applications.[79–82]

Polycaprolactone (PCL), another polyester with high biocompatibility and slow biodegradability which, in addition to the production of scaffolds[83–85], together with PLA is used in the manufacture of medical devices for the controlled release of drugs.[86–88]

Moreover, polyetheretherketone (PEEK) is a high-performance semicrystalline thermoplastic which is biologically inert and is proposed as an alternative for invertebral lumbar cages[89], customized dentistry parts[90] and, together with polypropylene (PP) as a possible material for cranial implants.[91,92]

Another possible application concerns the field of electronics where, for example, PLA blended with fillers such as carbon black, graphene or Cu micro-dust, produces filaments with conductive properties.[93,94]

Moreover, combining polyvinylidene fluoride (PVDF) with multi-walled carbon nanotubes and BaTiO3 it has been possible to obtain enhanced dielectric properties for the fabrication of energy storage devices such as capacitors,[95] while PP has been proposed as a possible material to be used for high and medium voltage insulation systems.[96]

The main polymer that is currently used for FFF applications in aerospace is Ultem, which is the trademarked name for polyetherimide (PEI), an amorphous specialty polymer certified by the US Federal Aviation Administration. In aerospace and automotive the amorphous polymer polyetherimide (PEI), certified by the US Federal Aviation Administration[97], is going to be replaced by high-performance semicrystalline thermoplastics such as PEEK and polyphenylene sulfide (PPS) which have proven their added value in this type of application.[98]

2.3 Mechanical anisotropy

As previously mentioned, the evolution of FDM from a prototyping technique to a production tool is hindered by several still unsolved problems, such as the poor surface quality determined by the size of the nozzle and the viscoelasticity of the polymer[69,88] the low construction speed[7,27] and the limited range of materials available compared to those for traditional processing methods.[99] More specifically, the key limitation that makes FDM unsuitable for practical applications derives from the weak and anisotropic mechanical properties originating from the layer-wise building strategy.[2] The products obtained with FMD by using either common commercial materials or high-temperature engineering polymers are worse in mechanical proprieties as compared to their counterparts produced by conventional processing like injection molding (IM) ,[100,101] with the bond interface between layers as the weakest link in these parts. In particular, the strength along building direction (z direction) is only about 50 –60% of that in printing direction (x-y plane)[102], thus making the parts obtained with FDM the most anisotropic among all additive manufacturing products.[103] Two printing parameters have

the greatest effect on the anisotropy of 3D printed parts, i.e., the raster angle and the build direction. Figure 2.7a reports a schematic illustration of three possible raster angles. Gao et al. showed how with the increase of raster angle from 0° to 45°/- 45° and then to 90°, the tensile strength of polylactide (PLA) parts decreased from 64.3 MPa to 54.2 MPa and then to 25.7 MPa (Figure 2.7b).[100] This behavior occurs for any type of sample printed with FDM, regardless of the type of material used.[101,104–106] The variation of tensile properties with raster angle arises from the fact that raster angle affects the way that load is transferred within the specimens. By soliciting the specimens in parallel to the printing direction (0°), thanks to inter-filament voids that reduce the loading-bear area, tensile strength comparable to those of the counterparts prepared with injection molding (IM) are obtained. With the increase of raster angle, the role of the bond interface between adjacent filaments in carrying the load increases, resulting in a worsening of tensile properties.[107] However, it is possible to eliminate the anisotropic effect of the raster angle on tensile strength by alternating layers aligned symmetrically with respect to the loading direction[108], for example printing with 45°/-45° raster angle.[109]

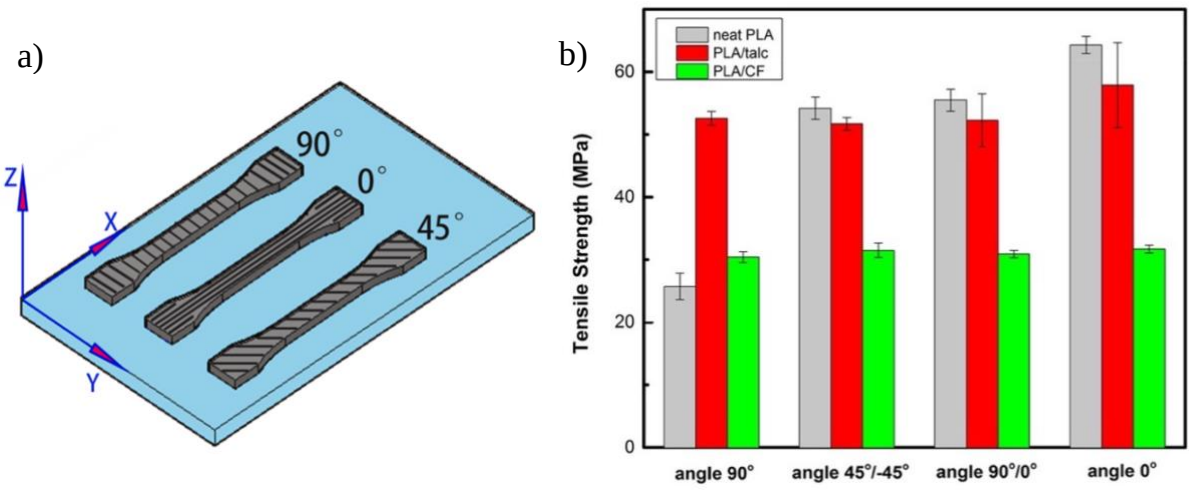

Figure 2.7. (a) Schematic illustration of raster angle; (b) Tensile strength of PLA-based specimens printed with various raster angles.[100]

The anisotropy of the mechanical properties of the parts printed with FFF is also strongly correlated to the orientation of the construction. As shown in Figure 2.8a, there are three possible construction orientations: XYZ, YZX and ZXY. Generally, comparable strength is achieved with the XYZ and YXZ orientations, compared to the ZXY orientation which is the

weakest configuration.[110,111] In recent work by Chacòn et al., the tensile strength of the PLA parts in the XYZ (upright) orientation is approximately 30 MPa, clearly lower than the XYZ (flat) and YXZ (on-edge) orientations (53.0 MPa) (Figure 2.8b).[35]

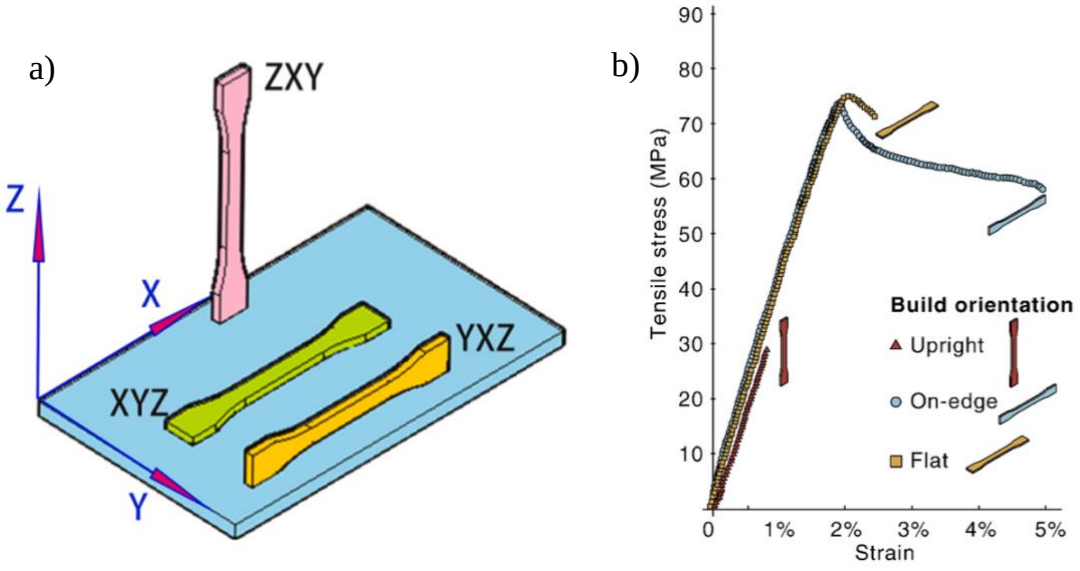

Figure 2.8. (a) Representation of the three possible construction orientations for FDM parts; (b) Stress-strain curves of PLA parts printed at various build orientations: XYZ (flat), YXZ (on-edge), and ZXY (upright) by using a layer thickness and print speed of 0.06 mm and 20 mm/s, respectively.[35]

Anyway, the anisotropy of mechanical properties remains, even if the parts' strength varies with process parameters like feed rate and layer thickness[35,112] or testing temperature.[113] This is due to the fact that samples printed in ZXY exhibit failure at the interlayer bond interface while other samples show raster failure.[35]

Despite the attempt to incorporate fillers into the original materials to improve their mechanical properties[114,115], the composites obtained show a still poorer interlayer adhesion and greater anisotropy than the starting materials.[116–118]

2.4 Interlayer bond formation

The final mechanical properties of polymeric materials strongly depend on the processing methods undergone, during which the polymer undergoes a thermal history and is subjected to certain external forces. In the case of conventional injection molding, the molten material is subjected to high pressures which cause a compact and almost homogeneous structure to be

formed.[119,120] During the FFF process, on the other hand, the molten polymer solidifies and binds with neighboring materials without the intervention of external forces other than the gravitational one.[121,122] The quality of the weld region between adjacent layers with respect to the bulk properties of the print material is a determining factor for the final structural integrity of the parts. The adhesion process between adjacent layers during printing is similar to the welding of polymeric films via reptation. This process is characterized by three distinct phases: 1) surface contact, 2) neck growth guided by surface tension and 3) molecular diffusion and entanglement across the filament interface.[122–124]. Schematic of interlayer bond formation is reported in Figure 2.9a.[125]

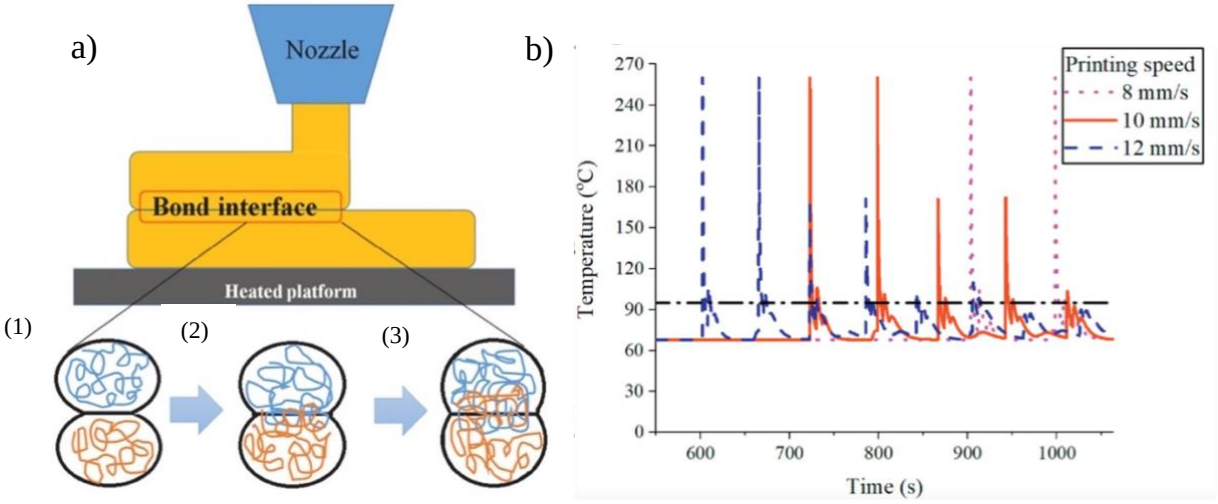

Figure 2.9. (a) Schematic of interlayer bond formation through (1) surface contact, (2) neck growth and (3) molecular diffusion and entanglement formation; (b) Temperature profiles at the filament interface for ABS parts printed at different print speed.[126]

Under isothermal conditions, the weld strength increases with a power-law dependence of weld time (τ) above the glass transition temperature (T_g) of the polymer, where the power law coefficient varies from 0.25 to 0.5 depending on the time scale and the initial configuration of the chain ends at the interface.[127] However, periodic temperature fluctuations due to the intrinsic nature of this type of technology make the process non-isothermal. As determined by thermocouple[121,126] or infrared thermography,[128–130] the interfacial temperature periodically increase to the peak values, and then decrease to the low limit around the buildplate temperature or the environment temperature. As an example, in Figure 2.9b temperature profiles of certain points at the filament interface obtained at different print speeds are shown for ABS parts from a work by Yin et al.[126] As visible, the variation of printing speed mainly shifts the peak of

temperature profiles, but all the profiles still keep the same pattern. As a consequence of the temperature fluctuation, the effective weld time for bonding between adjacent layers is very short, on the order of 1 s.[131] Furthermore, the behavior of polymers with temperature changes in semi-crystalline and amorphous materials.[124,132]

Currently, the formation of the interlayer bond is mainly studied on the basis of a modeling methodology.[122,133–136]

In general, coalescence of neighboring filaments starts instantaneously after surface contact.[137] The process can be traced back to that of the coalescence between two particles, driven by the surface tension, but hindered by inertial forces and the intrinsic viscosity of the fluid involved.[138] In the case of amorphous polymers, the viscous force is the dominant factor because of the high viscosity. For this reason, viscous sintering is the main mechanism for the coalescence of filaments. Bellehumeur et al. applied the Newtonian sintering model in combination with a 1D heat transfer model to predict the evolution of the neck between spherical ABS filaments during printing as follow:

$$\frac{d\theta}{dt} = \frac{\Gamma}{a_0 \eta} \frac{2^{-5/3} cos\theta sin\theta (1-cos\theta)^{1/3}}{(1-cos\theta)(1+cos\theta)^{1/3}} \qquad (2.1)$$

with

$$\theta = sin^{-1}\left({}^{y}/_{a}\right) \qquad (2.2)$$

where y, a_0, η, and Γ represents neck length, initial particle radius, viscosity, and surface tension, respectively.[123] The model reveals that the neck growth process occurs at interface temperatures above 200 °C.[123] However, during the printing process, this condition can be satisfied only for a few seconds until the next upper layer is deposited.[139] As consequence of this, there is not enough time for complete coalescence of the filaments before solidification, resulting in incomplete neck growth and a large amount of voids between filaments in the parts.[140,141] In fact, by combining the results of theoretical models with experimental ones, a clear dependence of the bond strength on the length of the neck is highlighted. In particular, printing parts at higher temperatures or using a lower layer thickness, allows to obtain a lower density of voids and, consequently, a higher quality of the bond.[121,134,142] Molecular weight also plays an important role in relation to the final quality of the bond. According to Equation 2.1 higher coalescence rates are obtained for lower molecular weights, regardless of whether an amorphous or semi-crystalline polymer is being processed.[143–145] Srinivas et al., for example,

demonstrated how the reduction in M_w of PLA from 245 to 148 kg/mol induced a reduction in void fraction (from 0.48% to 0.16%), favoring the coalescence of adjacent filaments.[146]

Once the contact between the surfaces occurs, the diffusion of the macromolecules at the interface continues until the glass transition temperature is reached, at which the polymer chains freeze. From the molecular point of view, Wool et al.[147] proposed a model in combination with transient heat transfer analysis to study the molecular diffusion process during FDM and evaluate the strength of the interlayer bond.[122] The weld strength was found to increase proportionally with $\tau^{0.25}$, which is similar to the non-isothermal healing of polymer films.[127] However, as shown by Seppala et al., typical FDM process provides a very short time for molecular diffusion in the range 0.1–100 ms[139], inducing a binding interface with the interdiffusion length less than the radius of gyration (R_g) of the polymeric material, thus showing a weaker binding quality with respect to the bulk properties.

Notably, neck growth and molecular diffusion processes were studied separately in the previous literature. Among them, Coogan et al. developed a model for predicting the interlayer strength through combining intimate contact, wetting and diffusion models, finding a strong dependence of the quality of the bond on the relaxation time of the material.[148]

On the other hand, McIlroy et al. developed a non-isothermal model involving polymer relaxation, entanglement recovery and diffusion processes to study the bond formation of polycarbonate (PC) during FDM.[3,4] The fracture toughness G_c^w at the bond interface is given by equation as follows:

$$G_c^w \sim \left(1 - \frac{1}{q v_w Z_{eq}}\right)^2 \qquad (2.3)$$

where $q \approx 0.6$[149], v_w is for the entanglement fraction at the bond zone and Z_{eq} is the entanglement number of a melt related to M_w. Due to the high shear rate immediately in the vicinity of the nozzle, an important stretch of the chains in the printing direction is obtained, with the subsequent re-entanglement hindered by the progressive decrease in temperature. The model therefore suggests that the final mechanical properties of the bond are more affected by the re-entanglement density, rather than the interdiffusion length, that surpass R_g at typical printing conditions.[3]

The interlayer bonding process is more complicated in the case of semi-crystalline polymers, since both the growth of the neck and the molecular diffusion are affected by crystallization,[101] especially if there are crystals having a different size than the interdiffusion length.[150,151]

Unlike amorphous materials, in the case of semicrystalline polymers, neck growth can only occur above the crystallization temperature.[145] Below it, the consistent increase in viscosity hinders further neck growth, but does not totally prevent interdiffusion, which still stops at the glass transition temperature.

McIlroy et al., introducing the crystallization kinetics of PCL in the model described above, showed that the time to 10% crystallization at the bond region was larger than the reptation time.[152] Nogales et. al, moreover, by means of real-time x-ray measurements on printed PP, found that the deposition of new layers induced a partial melting of the previous filament surface, allowing a fine welding with interdiffusion length well above R_g.[153] Generally, this means that the interfacial bond strength for semicrystalline polymer parts is typically not limited by interdiffusion. For materials with slow crystallization kinetics, such as PLA, the welding process is similar to what happens in the case of amorphous polymers, although flow-induced crystallization can sometimes occur on the filament surfaces.[154]

A good knowledge of the welding process is therefore essential to be able to control the final mechanical properties of the parts and thus optimize the production process. The main methods currently used to characterize the bond region concern the study of mechanical properties[155–157]and meso- or microstructures.[158,159]

The most used mechanical tests are tensile tests[156,157], three point bending[121,160] and impact tests.[161] Tensile test is the most direct method to measure the weld strength, since other methods can induce load modes like compression and shear.[155] One of the most used and representative methods to characterize interlayer welding is the Double cantilever beam (DCB) Mode-I fracture test.[161–163] The test specimens with a pre-crack are printed by depositing the filaments parallel to the specimens' longitudinal direction, in order to favor the development of the crack along the interlayer bond interface.[164,165] At this point, the Mode-I loading is applied at the end of two arms to detect the critical load at crack initiation and the load-displacement curves of DCB specimens. The fracture energy is then obtained by relating the maximum load with the sample thickness and the initial crack length.[166]

Other mechanical tests, such as Mode III fracture method[139,167] and T-Peel method[156,168] are also applied to characterize the interfacial bond quality. It also must be remembered that, since there are no ASTM standards for additive manufactured parts, testing of FDM parts should conform to the ASTM or ISO standards used for conventional processing methods,[103]

correcting the nominal cross-sectional surface for the actual cross-sectional area or the void fraction to obtain the normalized interlayer weld strength.[156]

Information on the quality of the interlayer bond can also be obtained from mesostructures, which can also be predicted using numerical simulations of computational fluid dynamics in combination with a surface acquisition algorithm.[169] Experimentally, it is possible to study the mesostructures of FDM printed samples using optical microscope[121,158,161] or scanning electrical microscopy (SEM)[125,164,170] in order to evaluate the contact length (L) between adjacent filaments and road height (h) (see Figure 2.10a). Indeed, Abbott et al. showed that the interface strength between adjacent layers grows proportionally with the ratio L/h.[155] The improvement of the bond quality occurs only up to the limit value of L/h=0.6 (Figure 2.10b). This occurs because L affects only the physical contact between the filaments but is not directly responsible for the interdiffusion.[156]

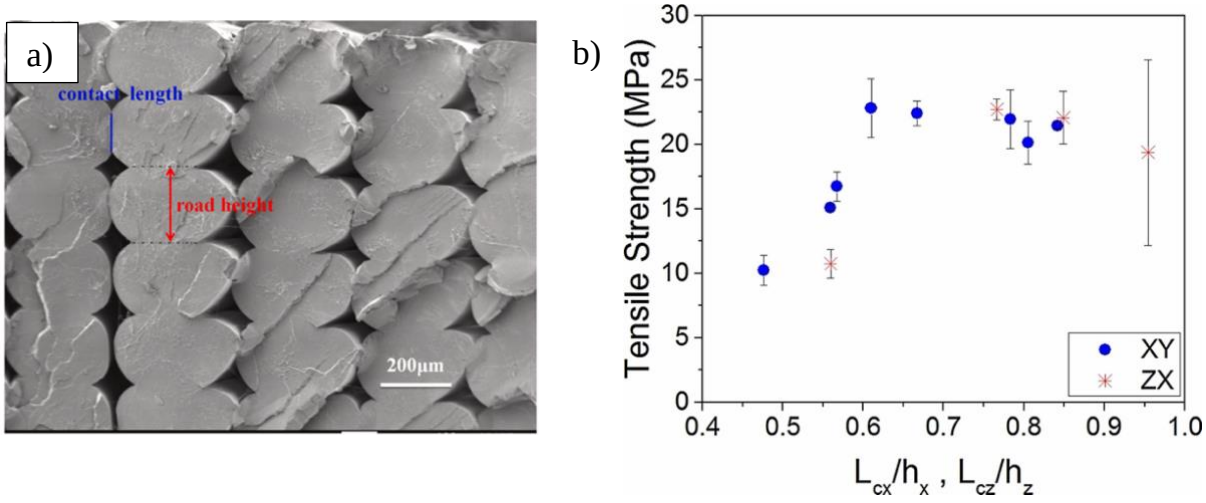

Figure 2.10. (a) Mesostructures of PLA parts printed in XYZ direction; (b) Interfacial tensile strength as a function of normalized contact length for PLA samples printed XYZ and ZXY directions.[155]

Finally, the microstructure, including chemical composition, chain configuration and crystal structure, can also influence the final quality of the weld. Wang et al., for example, combining optical microscopy and measurements with SEM, detected the presence of interfacial crystals of PLA by printing using low layer heights, and highlighted how these samples have much better impact properties than the counterparts obtained with IM.[158] Shmueli et al., in another paper, detected in-real time the evolution of the crystalline structure of printed PP using X-ray measurements.[130] It was verified that, despite the initial formation of kebab-structures, the partial re-fusion of the filament due to the deposition of subsequent layers induces a less

crystalline bond interface, and allows for complete molecular diffusion between adjacent filaments.

To overcome the problem of the weakness of the interlayer region it is therefore necessary to carefully control the process conditions and an adequate choice of feedstocks. In a recent work, Bhandari et al. propose a series of methods used to improve the bond interface for FDM-printed parts. These include microwave heating, infrared re-heating, optimization of printing parameters, and annealing.[171]

The process conditions are fundamental as they determine the temperature history undergone by the material and consequently, actively influence the quality of the bond between the adjacent layers. In particular, the increase in the nozzle temperature, allowing the material to remain above the glass transition temperature for longer, gives the polymer a longer time interval to form the weld.[136] As seen in the literature, by combining the time-temperature superposition principle with the rheological properties of the materials, it is possible to calculate the effective weld time.[72,135] Seppala et al. showed that the weld time for ABS parts increased from 0.01 s at T_N=210 °C to 0.1 at T_N=270 °C, while it remained substantially constant as the deposition rate varied (Figure 2.11a).[139] Particularly, the nozzle temperature is the parameter most able to optimize the quality of the bond compared to the others. Gao et. al showed how for parts printed in PA1012 there is an increase of tensile strength over 50% by increasing T_n from 200 °C to 220 °C (Figure 2.11b).[172] More generally, it must be considered that at high temperature the viscosity of polymeric materials decreases considerably, thus facilitating, in the case of our interest, the formation of the neck and the subsequent molecular interdiffusion.[155,167] On the other hand, bed and environment temperature determines the minimum temperature (T_{min}) polymers are maintained following the deposition. Consequently, a T_{min} above Tg means that there is a longer period for molecular diffusion between adjacent filaments.[173] Yin et al. showed how the increase of Tb significantly improved the interfacial weld strength between TPU and ABS from 0.86 MPa at 30 °C to 1.66 MPa at 68 °C.[126] Moreover, for semicrystalline polymers, a higher minimum temperature is useful both to improve the interfacial bond strength and in helping for the stress relaxation which often causes warpage phenomena.[174,175] However, when working at high temperatures, the possible degradation of the materials must not be neglected, which would lead to a net deterioration of the final mechanical properties and loss of dimensional accuracy.[104]

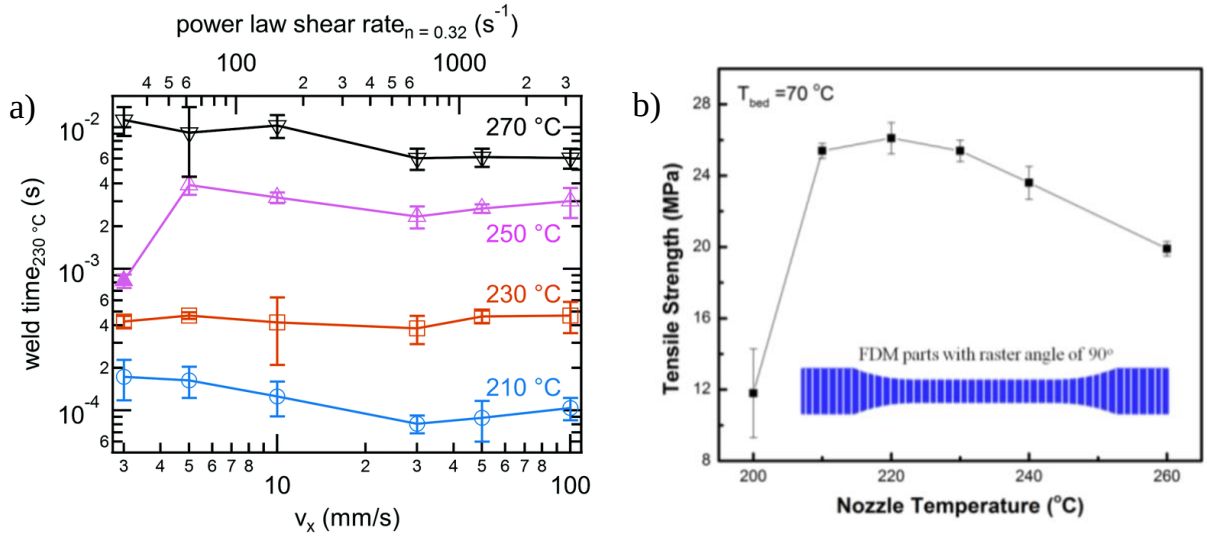

Figure 2.11. (a) Equivalent isothermal weld time at different nozzle temperature as a function of print speed. Weld time has been calculated by numerical integration of $1/a_T$ *profiles determined from WLF fit to* a_T *values and temporal weld temperature profiles for all printing conditions studied;*[139] *(b) Intralayer bond strength of PA1012 parts with 90° raster angle as function of nozzle temperature.*[172]

Deposition rate can influence the quality of the bond interlayer, too. By reducing the print speed, the heat flow provided by the print head and polymer melt induces local annealing at relatively high temperatures and long time-scales, allowing the melt to remain above the minimum temperature for a longer time, thus favoring interdiffusion.[146,167] The same effect can be achieved by decreasing the layer height. Small layer heights, in fact, contribute significantly to increasing the exit contact pressure, which is responsible for forcing the new layer into intimate contact with the previous layer.[135,176,177] Actually, it was found that the effect of layer height on the binding interface is highly dependent on the orientation of the print.[35,155] By comparing ABS-printed parts, it was found that the increased layer height provides greater tensile strength for the XYZ orientation as this increases the contact length between neighboring filaments. Conversely, a smaller layer height is preferred for the ZXY orientation due to the greater compaction between layers which promotes longer contact lengths.[155] However, in the case of PLA samples printed in ZXY direction, better tensile and flexural strengths were obtained by using higher layer height.[35] Nevertheless, these contradictory results could be related to the different methods of characterization of the mechanical properties of the interfacial bond, in which the specimens had different geometries and therefore were subject to different thermal histories during printing, but also by the different melt viscosity and crystallization behavior of the starting feedstock.[178] It is however necessary to remember that

the formation of the bond interlayer is in competition with the achievement of dimensional accuracy for FDM-printed parts. Conditions that favor a good welding can lead, in fact, to a loss of the surface quality of the products. As the average product temperature increases, preservation of print resolution as the number of layers in the z direction increases is progressively challenged by excessive flow and insufficiently fast solidification. Parts with lower layer thickness or low print speed,[179] sometimes as a result of cold-crystallization process, too.[146] A possible in-process solution could be the use light sources as an energy source to re-heat the deposited strands during printing in order to increase the temperature at the filament interface. Desphande et al, for example, proposed an in-process laser local pre-deposition heating (LLPH) method to increase the inter-layer interface temperature during printing to nearly twice as high as that without assisted heating.[180] As a result, interpenetrating inter-layer diffusion is achieved to a larger extent, allowing to increase interlayer bond toughness up to 77%. In a similar work, Striemann et al., integrated an infrared preheating system (IPS) into the FDM set-up for printing a carbon fiber-reinforced polyamide.[162] In addition to the improvement of the bonding quality obtained with the quasi-static standard tests, the mechanical tests under cyclic loading highlighted the opportunities to improve the lifetime performance of AM polymer with the IPS. Generally, an increase in the power of the laser or IR lamp allows for better welding quality. However, the use of excessive power and too long treatment times can cause problems in dimensional control, leading to polymer degradation and viscous flow.[166,180,181] The solution to these drawbacks is given by the use of ultrasound as shown by Tofangchi et al., who achieved an increase of up to 10% in the bond strength of ABS parts thanks to ultrasonic vibrations-induced decrease in polymer viscosity.[168] Another post-processing method to promote inter-strand molecular diffusion and thus improve the quality of the interlayer bond is given by annealing. As shown by Bhandari et al., post-processing via annealing was found to be effective in increasing the interlayer tensile strength of 3D printed PETG-CF and PLA-CF composites increased three-fold and two-fold, respectively, reaching values typical of their neat polymer counterparts.[171] Similarly, in the case of semi-crystalline polymers, annealing can lead to an increase in the degree of crystallinity.[182–184] For example, in a Papon et al.'s study on PAN-based milled carbon fibers, the annealing process post printing doubled the degree of crystallinity enhancing the mechanical properties significantly.[182] For amorphous polymers, an effective annealing temperature should be above glass transition temperature, while for semicrystalline ones, annealing temperature should be carefully chosen based on printing materials. For the latter, improvement in the interlayer bond is usually obtained when annealing is carried out between the T_g and the cold crystallization temperature

(T_{cc}) of the polymer since annealing above T_{cc} has no contribution to the interfacial strength, as the increase in crystallinity hinder molecular diffusion across the interface.[171] However, there are some cases in which it is possible to increase strength and modulus by annealing at T_{cc}, as found by Fitzharris et al. studying the mechanical properties of FDM-printed parts with polypropylene sulfide.[185] Finally, an innovative and promising post-processing method is microwave-induced local heating. In a recent work, Sweeney et al. prepared PLA parts with carbon nanotubes (CNTs) localized at the interlayer interface.[186] Upon exposure to radio frequency (RF), CNTs were selectively and locally heated to promote molecular diffusion and entanglements between adjacent layers, increasing the interfacial fracture strength by 275% over the untreated FDM-printed parts.

Chemical and physical modifications are other possible solutions to improve bond strength. Davidson et al. synthesized a partially cross-linked terpolymer consisting of furan-maleimide Diels− Alder (fmDA) adduct as the mending agent and then blended it with a commercial PLA material.[187] Following the heating in the nozzle, the mending agent thermally depolymerized and repolymerized upon cooling after deposition, generating chemical bonds even between neighboring layers. A net increase in the interfacial bond strength of 88% and 130% were observed for PLA parts containing 10% and 25% mending agent, respectively. In comparison, the physical modification, i.e., blending organic or inorganic additives with the polymer matrix is a highly efficient and low-cost way to strengthen the bonding interface and functionality of FFF molded parts. Usually, the composites obtained have a lower viscosity than the starting materials and therefore allow to obtain resistant parts with a low anisotropy. Previous work showed how it was possible to enhance the intra-layer bond strength from 25.7 MPa for neat PLA to 52.6 MPa for PLA/talc[172] or improve the interlayer bond strength of ABS specimens by 18–60% with the addition of calcium carbonate (CaCO3) nanofillers.[188] To sum up, it is evident that in order to obtain printed products of good overall quality, a profound knowledge of the molecular dynamics of the materials used, in the needed processability window, is required.

2.5 In-situ crystallization measurements

As mentioned above, for the interlayer bonding of semicrystalline materials, the knowledge of the crystallization temperature at printing conditions would be highly required. Researchers have developed a good knowledge of the structuring of semicrystalline polymers in classic

manufacturing techniques during the last decades. To this end, several methods to measure the crystallization of polymers during actual processing or under processing-like conditions (e.g., rapid cooling, shear flows) have been fundamental. Most results were retrieved applying synchrotron X-rays measurements to various processing technologies, [189]including pilot-scale processing units such as film blowing, extrusion casting, or fiber spinning.[190–193] Besides, experiments exploiting light-matter interaction have been coupled to lab-scale setups mimicking processing conditions to detect the phase transition more simply. For instance, Lamberti et al. correlated transmitted laser intensity and its depolarized component to thin polymer film's thermal history during a rapid cooling process.[194] Their set-up was able to quickly cool thin polymeric films and simultaneously record: i) the thermal history of the sample and ii) the total laser light intensity and its depolarized component passing through the sample of isotactic PP, allowing to monitor the evolution in time of the degree of crystallinity (Figure 2.12a). The interactions between the light beam and the crystallizing material were modeled taking into account the phenomena of absorption and scattering. The proposed model was able to reproduce the experimentally observed trend of light intensities (Figure 2.12b) and was validated by comparing it with a conventional DSC analysis. The evolution of crystallinity from DSC measurements was very similar to that calculated from the light intensity measurements, thereby confirming the internal consistency of the model.

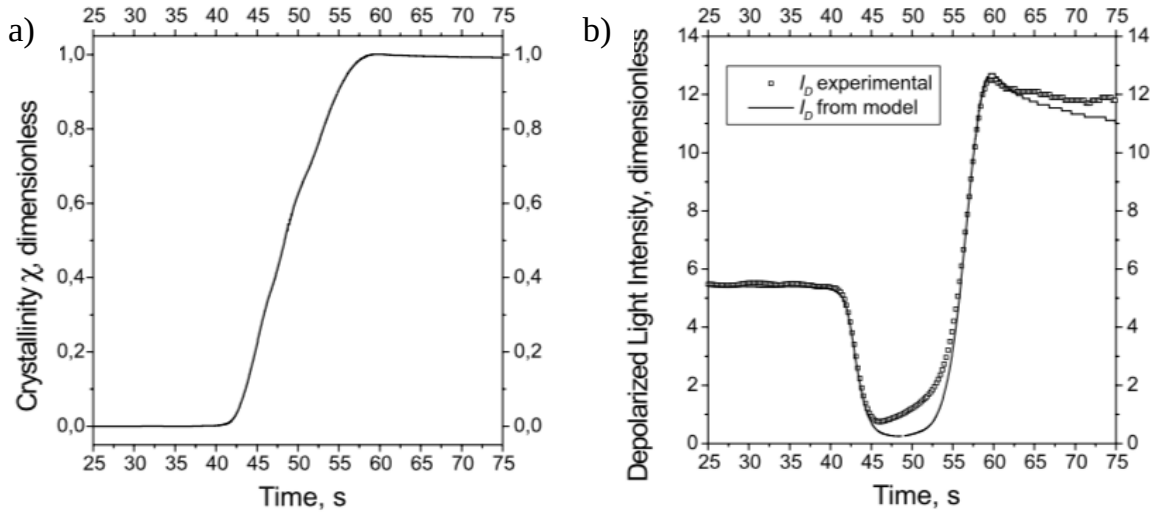

Figure 2.12. (a) Evolution of the degree of crystallinity over time obtained from the measurement of the overall intensity of light transmitted; (b) Trend of depolarized light over time according to the model and experimental data.[194]

Also, De Santis et al. followed a similar approach to monitor the evolution of crystallinity for an isotactic polypropylene resin by measuring transmitted light intensity during temperature

quenching.[195] The rapid cooling cycles were carried out by means of an innovative apparatus combined with an optical set-up constructed as follows: a Helium-Neon laser beam placed before a polarizer crossed the polymer film while this was subjected to the cooling treatment (Figure 2.13a). The apparatus was able to perform simultaneous measurements of the temperature and intensity of the depolarized beam, downstream of the film being analyzed. Furthermore, in order to monitor both the depolarized and the overall light intensity, beyond the sample, the beam was split into two beams: the first beam hit the first light sensor (the AlGaAs LED array in Figure 2.13a after passing through a crossed polarizer), the other beam struck directly the second light sensor (detector "O" in Figure 2.13a, a conventional silicon pin photodiode, in order to measure the intensity of the overall transmitted light.). The intensities of the depolarized light of the photoreceiver initially show almost constant values. At 120 °C, when crystallization begins, the intensity of the depolarized light decreases reaching a minimum and then rises to a maximum, reaching a new constant level with small oscillations, reasonably correlated to the end of crystallization. The out-of-center photodiode signal, on the other hand, is zero before crystallization and immediately increases with its onset, until it reaches an almost constant value (Figure 2.13b). The latter signal therefore reflects the broadening of the transmitted beam due to the increase in the scattering of light when the polymeric film becomes crystalline. The graph also shows the thermal history monitored by the thermocouple. Obviously, the temperature drops dramatically at the start of the cooling process due to the large temperature difference between the cooling medium and the sample.

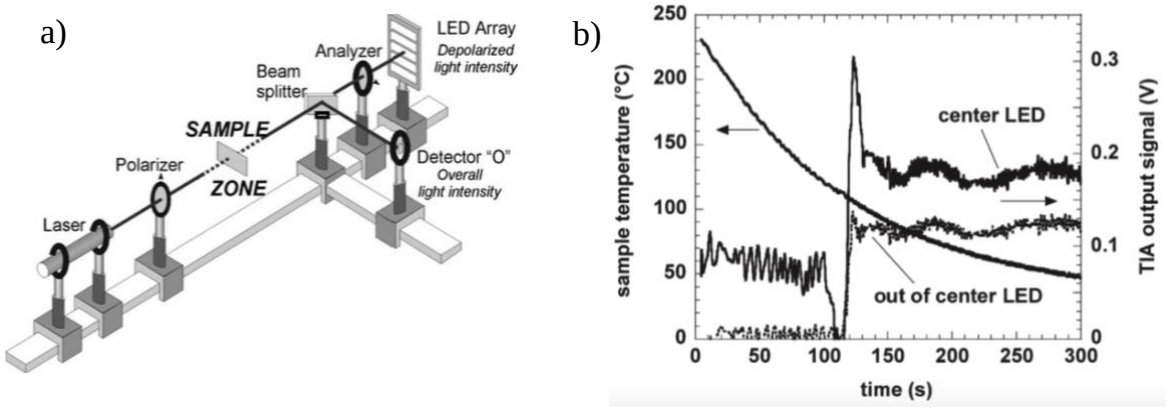

Figure 2.13.(a) Set-up used for optical measurements; (b) Variation of the polymer temperature and of the photosignal of the central and external LEDs of the AlGaAs LED array.[195]

On the other hand, shear or elongational flows applied to the semicrystalline polymers can significantly alter the crystallization kinetics and the morphology of the crystallites, affecting the properties of the material. Indeed, when the flow conditions are strong enough, the formation of fibrillar nucleation precursors increases the crystallization kinetics by orders of magnitude, generating highly oriented crystallites and drastically changing the final morphology.[190,196] The effects of shear flow were investigated systematically in different works on isotactic polypropylene. Fernandez-Ballester et all., for example, in a study based on isotactic polypropylene blends, used a pressure-driven shear cell coupled to an optical setup to measure birefringence and synchrotron X-rays.[197] The apparatus was able to access a high stress regime, such as to induce highly oriented crystallization under well-defined flow conditions, and also allowed independent control of the temperature history imposed on the polymer. After being heated to eliminate the previous thermal history, the melt was cooled to a shear temperature reached where a strong shear impulse lasting a few seconds was applied. The sample was kept at this temperature for about 20 minutes to be finally cooled to the final crystallization temperature. At the time of temperature reduction (Figure 2.14a), there was an increase in the growth rate of the oriented crystallites. Crystallite growth manifested as changes in the optical retardance, transmitted light, WAXD, and SAXS measurements (Figure 2.14).

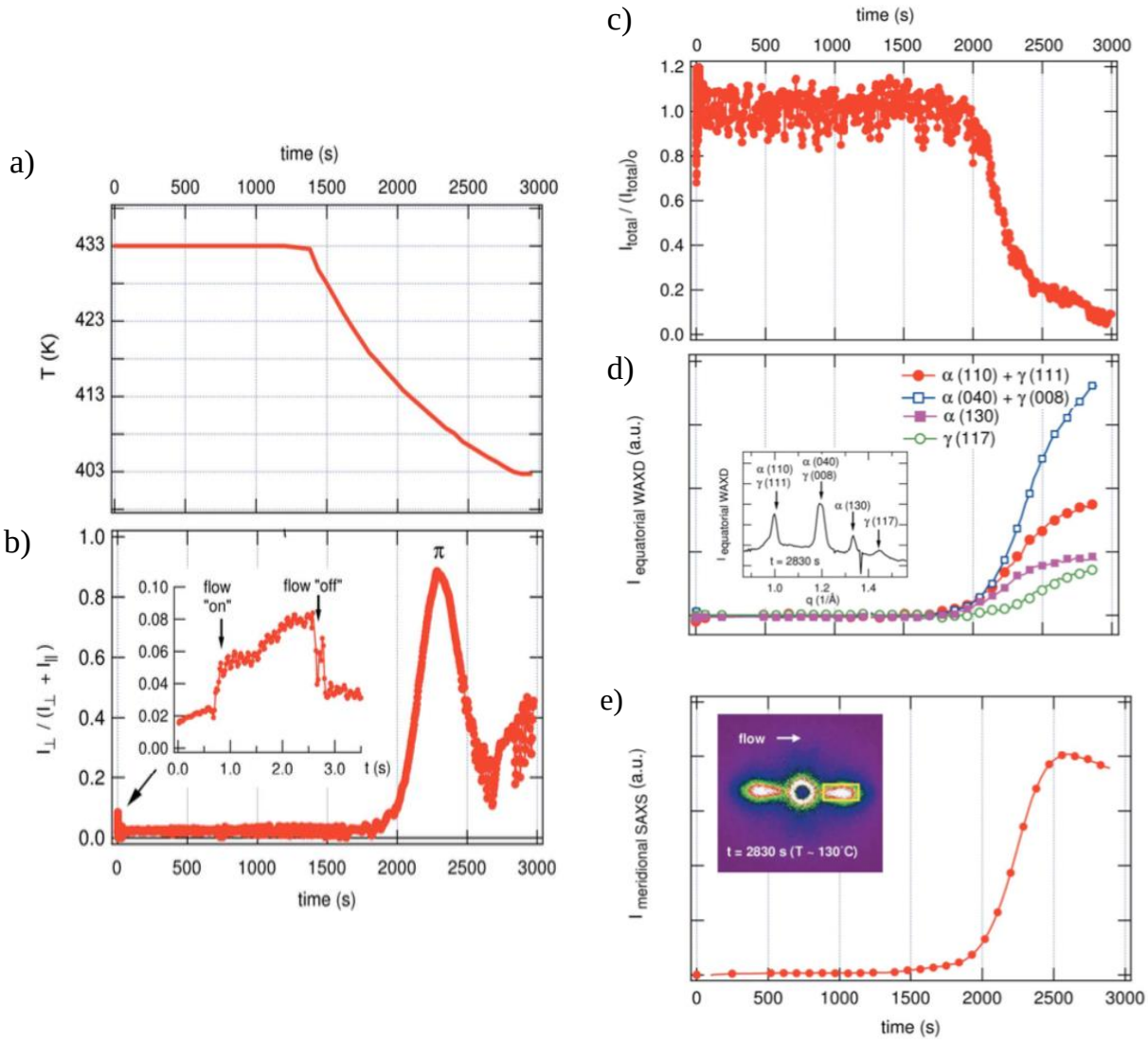

Figure 2.14. (a) Temperature evolution (b) intensity of visible light transmitted to crossed polarizers (c) intensity of transmitted visible light (d) intensity diffracted at selected high angles in the equatorial plane and (e) scattered intensity over a range of small angles in the southern region recorded for an experiment with cut at 0.093 MPa for 2 seconds at 433 K.[197]

In the case of birefringence, there is an increase due to the orientation of the melt flow, a decrease at the end of the shear application and a subsequent rise when the crystallization temperature is reached (Figure 2.14a-b). This is due to the fact that the oriented nucleation precursors generated at high temperature, and surviving in the melt at the crystallization temperature, serve as "templates" for the growth of oriented crystallites in which the polymer chains are preferentially aligned along the flow direction. Furthermore, during the crystallization of the sample there was a scattering of light due to the formation and growth of spherulite crystals. Therefore, the degree of turbidity, calculated as the ratio between the total intensity at a certain time and the initial one, was used to qualitatively monitor the progress of

crystallization (Figure 2.14c). Further information was obtained from X-ray diffraction analyzes at high angle (WAXD), regarding the crystalline unit cell, and low angle (SAXS), regarding the order of the inter-lamellar periodicity, or "long period" (Figure 2.14d-e).

Similarly, in FFF technology, understanding the effects of the processing conditions on the crystallization kinetics is necessary to develop better models for the process control. Recently, useful information has been obtained thanks to the use of synchrotron radiation. Indeed, Nogales et al. demonstrated that simultaneous small-angle and wide-angle X-ray scattering (SAXS and WAXS) measurements could be used to characterize in-situ crystal structure, crystallinity, and orientation effects for polypropylene printed using FFF technology.[153] Nogales also showed that the degree of crystallinity is larger in the bulk than on the surfaces of a single printed filament (Figure 2.15). The formation of this profile is caused by the effect of the top free surface and the welding zone on the time evolution of crystallinity.

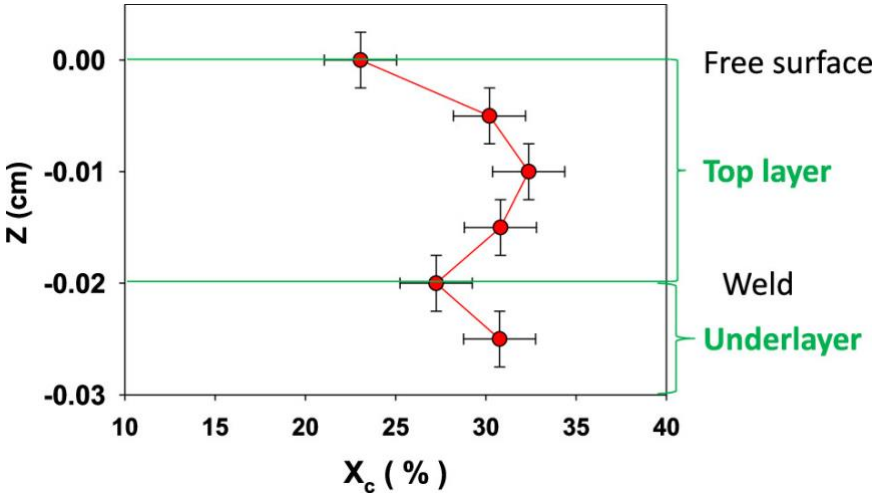

Figure 2.15. Final crystallinity values as a function of Z position below the free surface in a five-layer sample.[153]

Later on, Shmueli et al. coupled infrared thermography for temperature monitoring and the combination of SAXS and WAXS measurements to map crystallinity in polylactic acid FDM-printed parts.[130] The results highlighted the importance of the temperature profiles during printing on the structure/property relationships of the samples. Printing along the short axis of the product resulted in increased thermal retention and higher degrees of crystallinity and mechanical strength relative to samples printed along the long axis (see Figure 2.16).

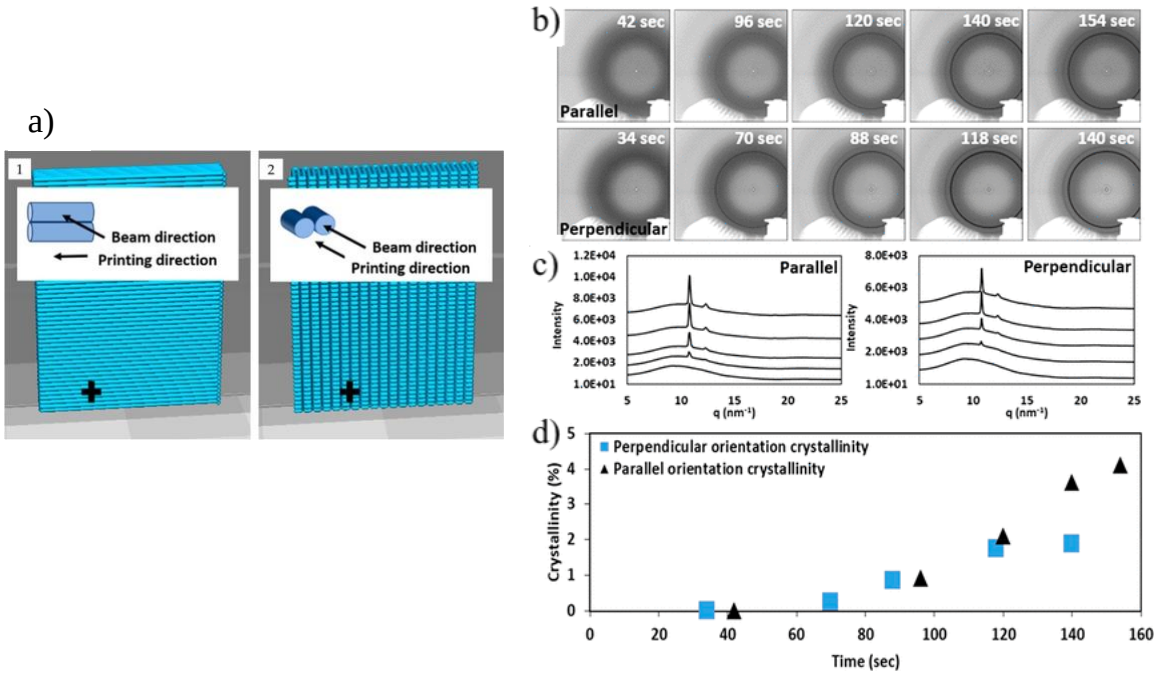

Figure 2.16. (a) The two modes that were used for printing the structures relative to the X-ray beam direction. Insitu WAXS measurements were performed irradiating the structure at the position marked with a plus sign (+); (b) 2D WAXS patterns obtained as a function of time from the location marked with the (+) in (a) above, at the positions (top) parallel to beam and (bottom) perpendicular to beam; (c) Evolution of the crystalline structure in 1D sections corresponding to the 2D images from Figure b parallel to beam (left) and perpendicular to beam (right); (d) Percentage of crystallinity in the samples, as a function of time, calculated from the WAXS curves in Figure b in the parallel (▲) and perpendicular (■) orientations.[130]

McIlroy et al. combined material characterization and on-line crystallization measurements with a flow-accelerated crystallization model in non-isothermal conditions, showing that the flow applied to the material during the printing process can influence the morphology of the crystals in the case of polylactic acid.[154] Although X-ray measurements using synchrotron light are successful in characterizing crystallinity, it is essential to extend the possibilities of study in this field to simpler laboratory techniques that do not require high energy radiation sources. In this context, Northcutt et al. combined infrared thermography and Raman spectroscopy to demonstrate the effects of different processing parameters (nozzle temperature and feed rate) on polycaprolactone crystallization kinetics.[132] In particular, they found how an high wall shear rate (calculated by modeling the printing process as extrusion through a capillary die) enhance the crystallization kinetics at lower nozzle temperatures, and how the effect of shear is much less pronounced when extruding at higher nozzle temperatures (Figure 2.17a). Complementary IR thermography measurements indicate rapid cooling of the extrudate outside the nozzle with a cooling rate that is independent of the filament feed rate (Figure 2.17b).

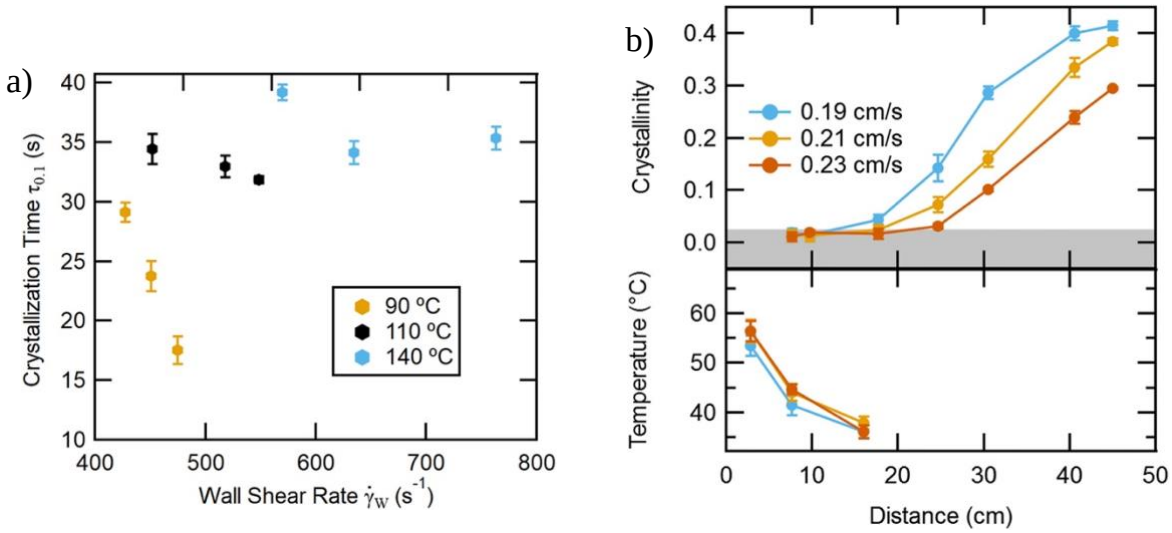

Figure 2.17. (a) Crystallization time as a function of the estimated wall shear rate for three nozzle set temperatures; (b) Evolution of crystallinity and temperature of PCL extrudate as a function of distance for the printer operating at 110 °C and different feed rates covering a wall shear rate range of (450–550) s^{-1}. The gray shaded region indicates crystallinities that are within measurement noise.[132]

3 MATERIALS AND METHODS

3.1 Filament materials

Different materials were used in the various chapter of the present work. In particular:

- In Chapter 4 the material used for the study is a poly(L-lactide) (PLA), indicated with the commercial name 4043D,[198,199] and with a content of D-isomer of about 4% in the form of pellets and as a spool of 1.75 mm filament for MatEx. The material was characterized by DSC has and presents a glass transition temperature, T_g, of about 60 °C and a melting temperature of about 151 °C. We note that upon standard cooling at a rate of 10 °C/min, the material can barely crystallize and is almost totally amorphous, with a crystallinity index less than 1%. The molar mass distribution was measured by means of Size Exclusion Chromatography (SEC), using a Waters 717 autosampler with a differential refractometer (Waters 2410), a pump (LC-20A Shimadzu) and three Waters Styragel columns (HR2, HR4 and HR6). Tetrahydrofuran (THF) was used as a solvent at a flow rate of 1 mL/min and a temperature of 35 °C. The values obtained are *Mn*=79 kg/mol and *Mw*=173 kg/mol for the number and weight average, respectively.

- The Chapter 5 compares the behavior of six different polylactide filaments having different molar mass and D-lactide comonomer content. In general, the considered materials contain either low, intermediate, or high content of D-lactide comonomer. The approximate percentages are indicated, for the sake of simplicity, as 0, 4, and 12 mol%. Table 1 shows the list of materials used with the indication of their molecular characteristics, including the average number of entanglements per chain (the molar mass of a chain section between entanglements is M_e= 9 kg mol^{-1}).

Table 1. Materials

Adopted name	**Molar mass (g/mol)** M_w	**Approx. D-Lactide content (mol %)**	$Z_{eq} = M_w/M_e$
PLA_0_94k	94.000	0	10
PLA_0_190k	190.000	0	21
PLA_4_160k	160.000	4	17
PLA_4_200k	200.00	4	20
PLA_12_117k	117.000	12	13
PLA_12_180k	180.000	12	20

- The work reported in the Chapter 6 compares the behavior of two co-polyesters feedstock materials, named commercially as NGEN and HT, respectively. As for NGEN is a copolyester which include typical monomers such as dimethyl terephthalate (DMT) and dimethyl isophthalate (DMI), while the dialcohol unit can include ethylene glycol (EG) and 1,4-cyclohexanedimethanol (CHDM), in agreement with the measured glass transition temperature value (85 °C). Its weight average molar mass is around 19000 g/mol. HT, on the other hand, possesses a Mw of about 18000 g/mol and the constituent comonomers are CHDM and 2,2,4,4-Tetra-methyl-1,3-cyclobutanediol (TMCD), while the diester unit is constituted by DMT. The structures of the monomers composing the different repeat units are shown in Figure 3.1.

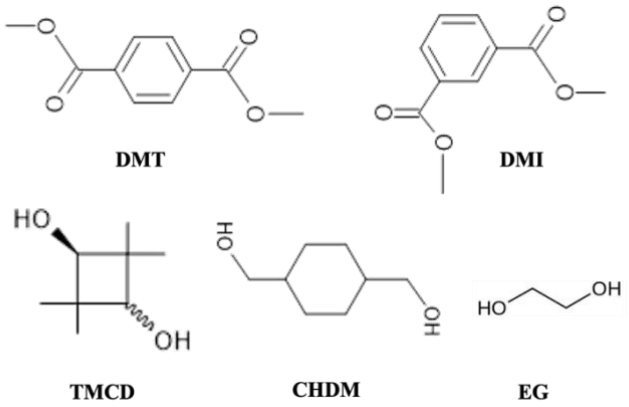

Figure 3.1. Structures of the comonomers constituting the NGEN and HT copolyesters. Top row diesters, bottom row dialcohols.

- The materials used in Chapter 7 are marketed by DSM under the names Novamid ID 1070 and ID 1030, which are a polyamide-6 homopolymer and a polyamide6-6,6 copolymer respectively.[200,201] As reported in the corresponding technical data sheets, when heated at 10°C/min they have melting temperatures of 220 and 200 °C respectively.

- The study reported in Chapter 8 compared Novamid 1030 (DSM), a crystallizable copolymer consisting of Nylon-6 and Nylon-6,6 co-units[200,201] with PLA 4043D as an amorphous reference. Both the polymer filaments did not contain any dye that would interfere with the optical measurement. PLA is indeed transparent, while Novamid 1030

is opaque owing to light scattering from the crystallites. To remove from the feedstocks any trace of humidity, before printing the samples the spools were dried in an oven overnight at 80 or 40 °C for polyamide and polylactic acid, respectively.

3.2 3D printers and sample geometries

The printer used to prepare the specimens in Chapter 4, 5, 6 and 7 is a Intamsys Funmat HT (Shanghai, China), equipped with a nozzle of 0.4 mm for Chapter 4 or 0.2 mm for the rest of the work (Figure 3.3a). To simplify as much as possible the preparation of the samples in view of the subsequent measurements, the chosen printed geometry is that of a free-standing square tube (4 cm × 4 cm × 4 cm in size) consisting of a single-filament stack with layer height of 0.4 or 0.2 mm (Figure 3.2a-b). This means that, within each layer, the nozzle moves along a square path and extrudes a single polymer filament. In this way problems of inter-layer voids are eliminated, and the mechanical test probes a single weld surface only.

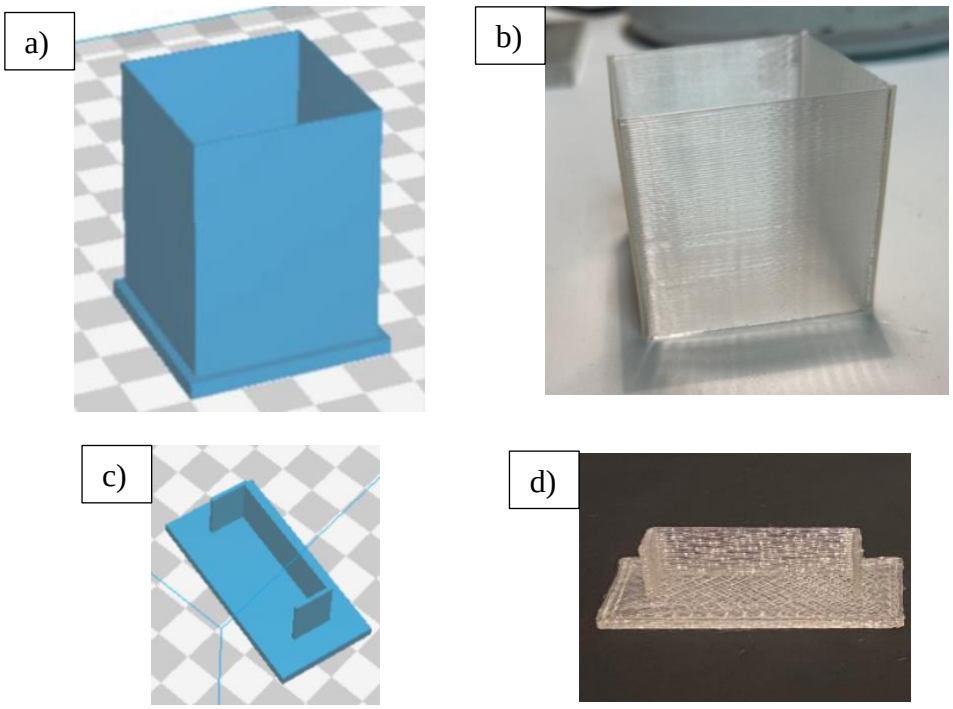

Figure 3.2. (a-b) Sample geometry consisting in a free-standing square tube (4 cm × 4 cm × 4 cm in size) constituted by single layers superimposed with layer height of 0.4 mm. In particular, (a) shows the model inside the software Cura before slicing, while (b) shows a test part printed with PLA 4043D. (c-d) Sample geometry used for light scattering measurements. In particular, (a) shows the model inside the software Cura before slicing, while (b) shows a test part printed with PLA 4043D.

Sample with the described geometry was designed with the software Tinkercad and subsequently converted into an STL format file for printing. The software (Ultimaker, Utrecht, The Netherlands) Cura was used to generate G-code and to set up the processing conditions through a slicing process on the original file.[202]

In Chapter 8, the necessity to fit the optical setup in the experiment did not allow to use of a printer with an adjustable temperature chamber. Therefore, we used an open frame FFF 3D printer, Creality® Ender 3, with a nozzle temperature up to 260 °C and a deposition plate temperature up to 100 °C (Figure 3.3b). The print head is able to move along the x direction and translate upwards on the z axis. The bed plate moves along the y-axis. This printer model allowed us to set the feed rate on a relative scale between 0 and 100% (where 100% stands for the maximum deposition rate of the 3D printer). Moreover, we had to choose to print a small object designed with simple and practical geometry to perform the optical measurements. The design consists of three vertical walls made with a single filament thickness (Figure 3.2c): the central wall is flat and about 2 cm wide, allowing an easy alignment of the laser beam, with two smaller supports at the sides. The print direction of the nozzle was alternating between each layer. Figure 3.2d shows an example of this geometry printed with PLA 4043D.

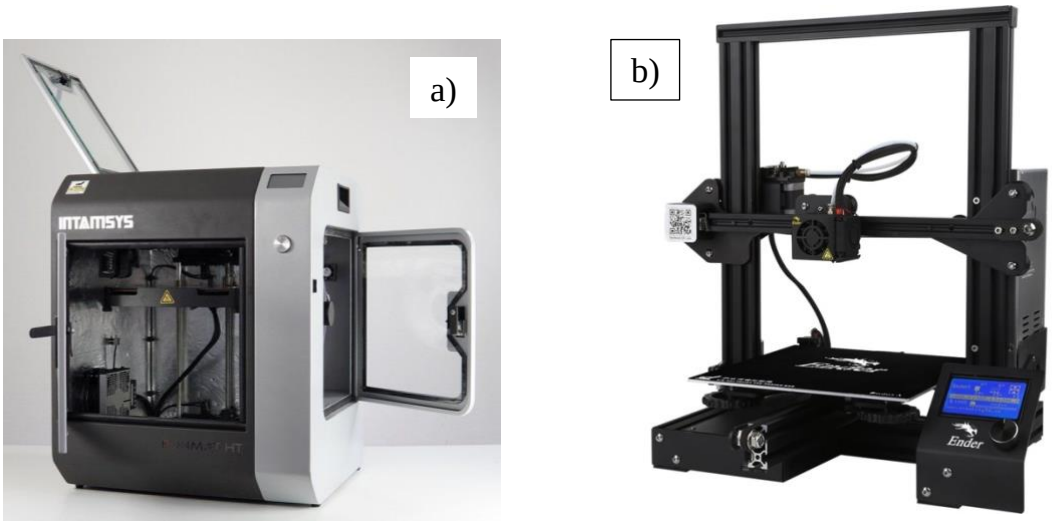

Figure 3.3. (a) Intamsys Funmat HT 3D printer (Shanghai, China); (b) Creality® Ender 3 3D printer.

3.3 Differential scanning calorimetry (DSC)

All the materials were initially subjected to heating-cooling-heating cycles to highlight their intrinsic characteristics. The power compensated differential scanning calorimeter used is the model DSC 250 from TA Instruments (New Castle, DE, USA) (Figure 3.4), calibrated with indium and operating under a flow of 50 mL/min of nitrogen. For all materials, samples with mass between 3-5 mg were prepared in aluminum pans and subjected to the respective thermal ramps.

In Chapter 4, the PLA 4043D feedstock was first molten at 210 °C and the subjected to a cooling cycle at 10 °C/min down to 20 °C, followed by a subsequent heating, in order to evaluate its intrinsic crystallinity.

In Chapter 5, all the six different PLAs were submitted to the same thermal history as that of PLA 4043D in Chapter 4.

In Chapter 6, the two co-polyesters were first molten at 250 °C and then subjected to a cooling until 20°C and subsequently to a second heating to confirm their amorphous microstructure. To verify the sole existence of the amorphous structure even after the 3D printing process, printed samples of both co-polyesters were subjected to heating ramps at 10°C/min from 20 up to 250°C.

In Chapter 7, both polyamides Novamid 1030 (DSM) and Novamid 1070 were first molten at 250 °C and subsequently subjected to cooling until 20°C and subsequently to a second heating to study their different degree of crystallinity. Furthermore, to study how the different process conditions can influence the crystallinity of the materials, samples of both polyamides were subjected to heating ramps at 10°C/min from room temperature to 250 °C after printing.

In Chapter 8, PLA 4043D and Novamid ID 1030 (DSM) were molten at 210 °C and 250 °C respectively, to eliminate the previous thermal history and then subjected to a cooling until 20°C and subsequently to a second heating.

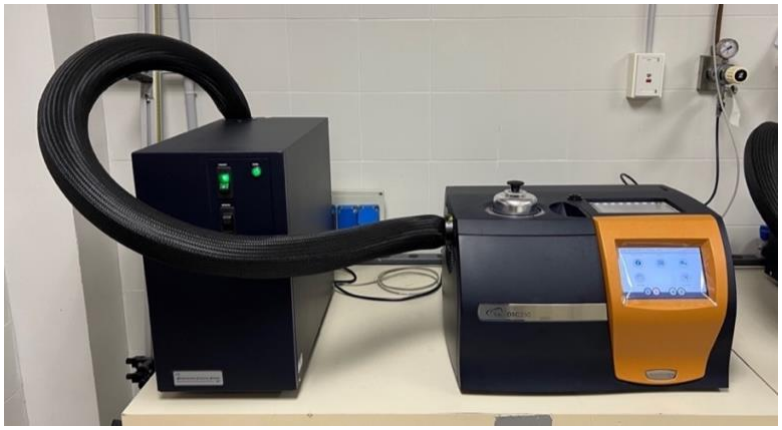

Figure 3.4. Differential scanning calorimeter DSC 250 from TA Instruments (New Castle, DE, USA).

3.4 Birefringence measurements

In Chapter 4, the polymer chains orientation in the printed samples was determined by measuring the birefringence. The measurements were made using a polarized light optical microscope Reichert 350241, coupled with an Ehringaus compensator (Figure 3.5). Single printed walls were positioned on the rotating object plate, under crossed polarizers condition. The sample was rotated until the printing direction (which coincides with the optical axis of the birefringent printed walls) reached an orientation of 45° with respect to the polarizer transmission directions.

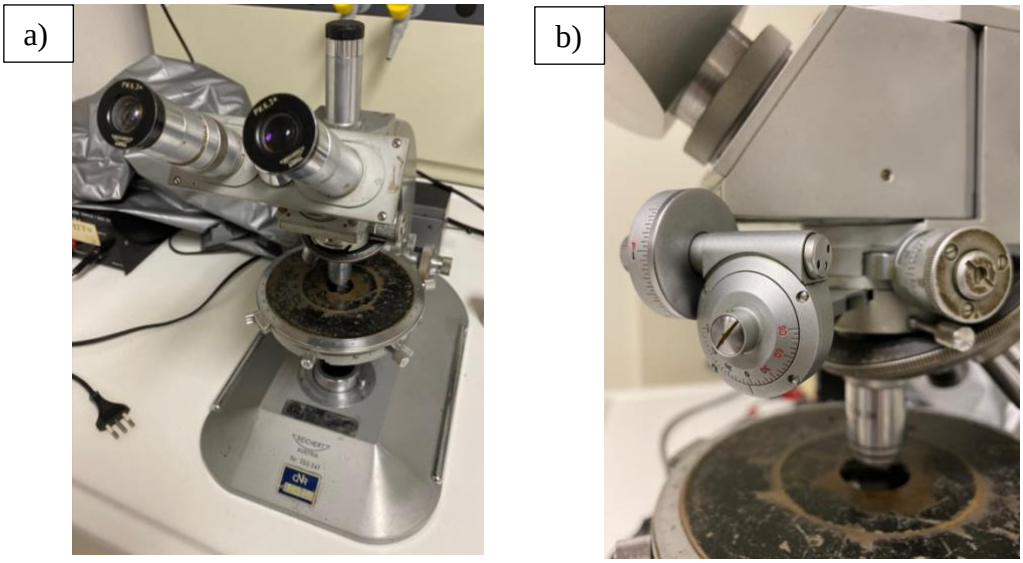

Figure 3.5. (a) Polarized light optical microscope Reichert 350241 used for birefringence measurements and (b) Ehringaus compensator used in conjunction with the microscope.

In order to measure the birefringence of the sample, the Ehringaus compensator was inserted in the optical path, and rotated around its optical axis until the extinction of the light transmitted by the printed object was achieved. Thanks to the known relation between the compensator crystal's rotation angle and its optical retardation (φ), the unknown birefringence of the sample (Δn) with a thickness d, can be determined according to $\Delta n = \varphi/d$. We note that in the case of the printed walls, the total thickness, measured with digital micrometer, has been used. Since this value does not generally correspond to the actual thickness of the oriented (and birefringent) region, it is more correct to indicate the reported values as 'apparent birefringence'.

3.5 Rheological tests

Rheological analyses were performed using a HR 10 rheometer from TA Instruments (New Castle, DE, USA)(Figure 3.6). At first, materials were prepared in the form of films with a compression molding press. Then, after amplitude sweep tests to identify the linear viscoelasticity regime, were subsequently subjected to frequency sweep tests at different temperatures, consistently with the respective recommended processing ranges.

- In the fourth chapter, measurements on PLA 4043D were carried out in a range of angular frequencies frequency range from 0.5 to $3*10^5$ rad/s, in an amplitude strain range of 1-4%, repeating the measurement at different temperatures in the range 110-200 °C.
- In the fifth chapter, measurements on the PLAs were carried out in a range of angular frequencies from 0.1 to 100 rad/s, with an amplitude strain of 2% in the linear viscoelastic regime, repeating the measurement at six different temperatures for each material, in the range 150-200 °C. The rheological measurements for the PLA_0_94k material were performed at a higher temperature range with respect to the others due to its incipient crystallization at lower temperatures.
- For the copolyesters described in the sixth chapter, the rheological measurements were carried out in a range of angular frequencies from 0.1 to 50 rad/s, with an amplitude strain of 3% in the linear viscoelastic regime, repeating the measurement at six different temperatures for each material (from 190 °C to 240 °C for NGEN and from 230 °C to 280 °C for HT).

Figure 3.6. HR 10 rheometer from TA Instruments used for the rheological characterization of the materials.

3.6 In-situ temperature history measurements

To measure the temperature history during filament deposition, we used a micro-thermocouple (type K) placed directly on the plate of the printer, in correspondence with the material deposition area. The thermocouple was linked directly to a Hi-Speed USB acquisition unit (NI USB-9162) (National Instruments) and the related software allowed to monitor the thermal profile in real time.

3.7 Polarization modulated infrared spectroscopy

In the fifth chapter, to measure the molecular orientation in the printed specimens, we made use of modulated polarization spectroscopy. The experiments were conducted at the IRIS Infrared beamline of the Helmholtz-Zentrum Berlin synchrotron facility BESSY II. The setup is composed of a Nicolet Nexus 870 FTIR spectrometer coupled to a Nicolet Continuum infrared microscope and a Hinds PEM-90 II photoelastic modulator (PEM) unit to generate the orthogonally polarized light. The PEM consists of a ZnSe crystal which, when stretched and compressed, creates birefringence of infrared light in the material, inducing a periodic rotation

of the polarization plane from 45° to 0° and 90° at a high frequency. In this way, the doubly modulated IR beam containing alternating polarization is focused on the sample and collected at the dual channel detector of the microscope. The signals of the two orthogonal polarization states are split from the modulated interferogram by a demodulator generating the difference (II - ⊥) and sum (II + ⊥) interferograms. With the Fourier transform of this two interferograms one gets the normalized differential absorbance spectrum, or so-called polarization modulated dichroic difference (PMDD), defined by:

$$I_{PMDD} = \frac{I_{II} - I_{\perp}}{I_{II} + I_{\perp}} \qquad (3.1)$$

where I_{II} is the intensity at the detector when the incident light is polarized parallel to the reference axis of the sample, and $I_{\perp}$ the intensity at the detector when the light is polarized perpendicular with respect to the sample. For more details about this set-up, readers can refer to.[203,204]

By changing the two orthogonal polarization states and obtaining the differential absorbance spectra, it is possible to determine the local orientation of dipoles, and therefore the local chain orientation. All measurements were performed in transmission mode using two IR reflective objectives (Schwarzschild, 0.65 N.A.) and a MIR liquid nitrogen cooled HgCdTe detector. Spectra were taken in the range from 650 cm^{-1} to 4000 cm^{-1} with an aperture size of 50 x 50 μm and 6 cm^{-1} spectral resolution. Each point was accumulation of 256 scans. The intrinsic sample reference axis was chosen to be the printing direction.

The specimens on which polarization modulation spectroscopy measurements were carried out were printed with a rectangular shape and dimensions 1.5 cm x 1 cm x 0.5 cm, maintaining the same deposition direction for each layer. Part of these samples were cut to a size which could fit the sample holder of a manual microtome (Leica RM2235), and then cut at room temperature in the direction parallel to that of printing. The final thickness of the obtained slices was 5 μm, an optimal size for avoiding saturation of the polylactic acid absorption bands.

Using the Omnic software, a rectangular map of 80 points was selected on each sample. The map consisted of 4 lines containing 20 points each with 20 μm step size between the points.

The analyzed sample slices were large enough to allow the observation of at least one interface between different printed layers and thus have information on the possible distribution of the orientation.

3.8 Mechanical tensile tests

In Chapter 4, 5, 6 and 7 the samples were subjected to a tensile test (ASTMD1938) to determine the strength of the weld as a function of the printing conditions. The printed shapes (square tubes) were first cut along the four side walls using scissors. Then, three rectangular shaped tensile specimens for each printing condition were punched from each side wall with a pneumatic press, with the direction of deposition of the layer oriented at a 90° angle to the cutting direction. The tested samples have the following dimensions: 40 mm in height, 13 mm in width and approximately 0.45 mm in thickness. Tensile tests were carried out using an Instron 5565 S/NO H1505 (Figure 3.7), with an initial distance between the clamps of 12 mm and a separation speed of 6 mm/min.

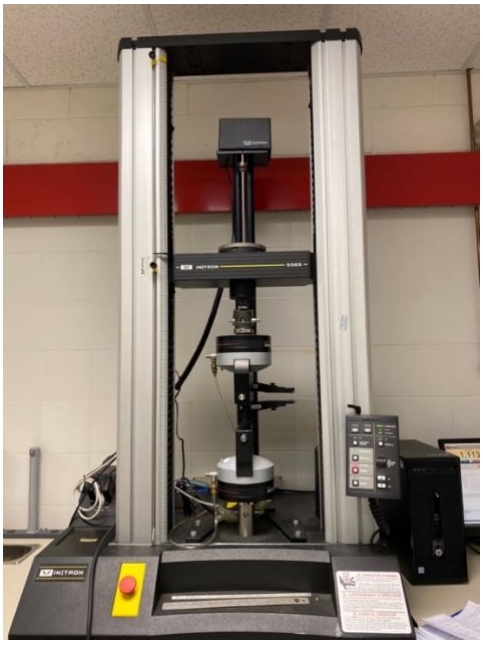

Figure 3.7. Instron 5565 S/NO H1505 used for mechanical tensile tests.

Rectangular shaped (single-stranded wall) samples are chosen, rather than a traditional dog bone shape, due to the geometric constraints imposed by the print size and the blade available to cut the sample. To derive the tensile strength the actual cross-section of the specimen must be known; for our test geometry derived from 3D-printed walls, this is the weld-area, i.e., the interface between two adjacent printed filaments. While one of the weld widths is considered equal to sample's width (13 mm), the weld-length of such cross-section has been measured using a stereoscope. For each printing condition, three specimens were observed with a Leica stereomicroscope, using a OptikalB5 Digital Camera to capture images of the weld-line. The

exact weld-length was obtained via image analysis with the ImageJ software, after calibration with standard microscope ruler. An average of at least 5 measurements was computed for each sample.

3.9 Light scattering set-up

Figure 3.8a shows two examples of the geometry printed for the work of Chapter 8 with the two materials. The print direction of the nozzle was alternating between each layer. The different optical appearance of amorphous and semicrystalline polymers is evident. The setup for light scattering measurements (Figure 3.8b) consists of a 633 nm continuous wave laser source (He-Ne, 10 mW) impinging perpendicularly on the printing object. The laser source and the printing part were aligned with two adjustable laboratory jacks, and a variable iris and a linear polarizer were placed in the optical path between them. The polarizer was set at 45° off the 3D printer's x-axis. The laser beam impinging on the 3D printing object had a diameter of about 3 mm, which corresponds to the thickness of slightly less than 10 printed layers (layer thickness 0.4 mm). Therefore, the collected signal represents the average of several layers. A second polarizer set at -45° off the x-axis was placed after the build platform to observe possible oriented morphologies arising from the flow deposition process. Last, a semi-transparent screen sheet was placed at 20 cm from the printed wall to collect the scattered light. The scattered intensity was then captured using a Hamamatsu C5405-51 CCD camera with 752 x 582-pixel resolution, placed a few centimeters from the screen, and equipped with an objective lens. The camera was connected to a computer with a data acquisition unit controlled by a LabVIEW® application (National Instruments, Austin, TX, USA) for frame acquisitions. Frames at set time intervals of 40 ms were then extracted with the software VideoMach. All the frames were then analyzed with the software ImageJ to integrate both transmitted and scattered light intensities. The measurements were carried out in a dark room to increase the signal to noise ratio.

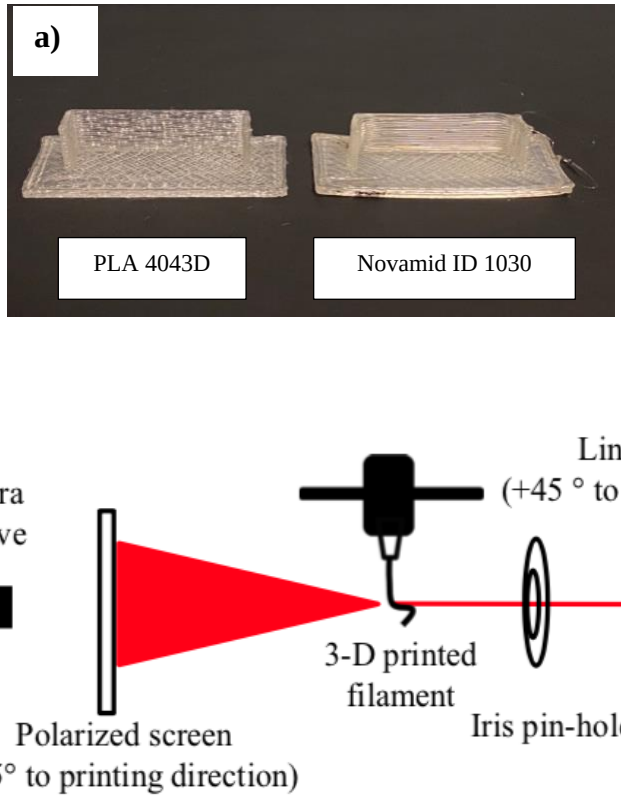

Figure 3.8. (a) Printed samples: PLA 4043D (left), and Novamid ID (right). Note the difference in opacity; (b) Schematic of the light scattering measurement set-up.

4 EFFECT OF RESIDUAL ORIENTATION ON WELD STRENGTH

4.1 Introduction

In this chapter, we measure molecular alignment in a simple FDM-printed object using birefringence. In particular, residual orientation of the polymer chains due to the printing flow is found to be localized to the weld regions between printed filaments, while the bulk of each filament is isotropic. By comparing experimental results with the ones obtained with a molecularly aware modeling, we find a net reduction in weld strength for strong printing conditions that is due to orientation of the polymer molecules that occurs during flow through the nozzle and deposition onto the build plate, rather than to poor inter-diffusion.

4.2 Thermal characterization

Using differential scanning calorimetry (DSC), we found that upon standard cooling at a rate of 10 °C/min, the material can barely crystallize (Figure 4.1) and is almost totally amorphous, with a crystallinity index lower than 1%. Since the cooling rate in MatEx in generally much faster, it follows that the 3D-printed wall is amorphous.

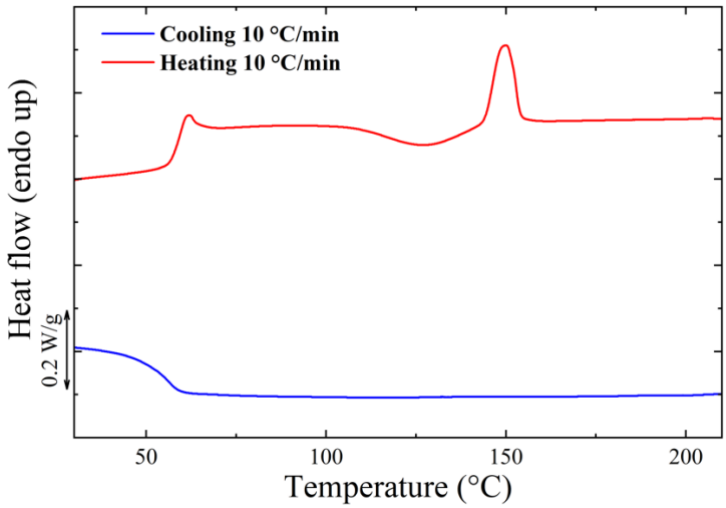

Figure 4.1. DSC cooling and second heating curves for PLA 4043D, measured at the rate of 10 ° C/min.

4.3 Numerical model

The numerical model has been previously developed and employed elsewhere.[3,4,152,205] Thus, here we provide only a brief overview of the model and the governing equations.. In this work, the temperature model has been adapted to account for the dependence of the cooling rate on the print speed, as detailed in Chapter 4.2.3.

4.3.1 Overview

In summary, the model assumes isothermal steady-state flow through an axisymmetric nozzle of radius R_N at some extrusion speed U_N and uniform nozzle temperature T_N. Flow through the nozzle is followed by fast deposition onto a build plate, moving at transverse speed U_P, into an elliptically shaped filament of thickness H, and width W. The extrusion and transverse print speeds are related to the filament geometry through conservation of mass via

$$\pi R^2 U_N = \frac{\pi}{4} H W U_P \qquad (4.1)$$

The temperature is assumed to remain uniform during deposition and is therefore independent of print speed during flow. The model is molecularly-aware in the sense that polymer stresses are suitably accounted for via a constitutive model (single-mode Rolie–Poly[206]) that considers both the stretching and orientation of the polymer molecules within an entangled network. Entanglements due to neighboring polymer molecules are represented by a hypothetical tube region[207], which restricts the diffusive motion of a polymer chain to along the tube's contour length (Figure 4.2). Thus, there are two characteristic time:

- the reptation time τ_d, which is the time taken for the polymer to diffuse along the tube contour length and governs the time taken for chain orientation/alignment to relax,
- the Rouse time τ_R, which is the time taken for the polymer chain to relax within the tube region and governs stretch relaxation.

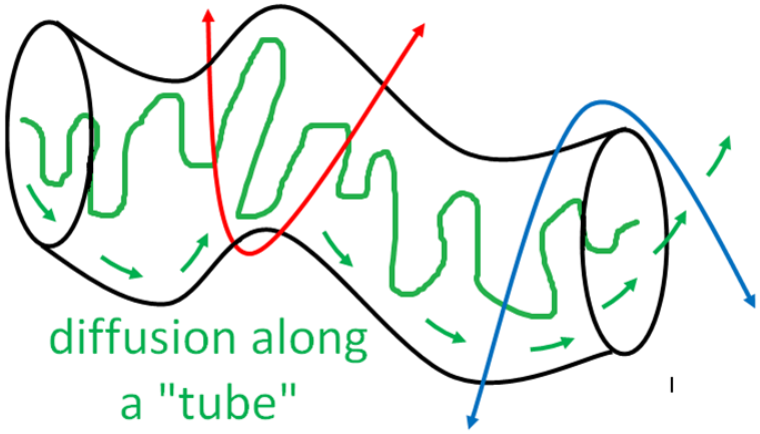

Figure 4.2. A hypothetical tube region represents constraints due to entanglements. The polymer chain must diffuse (reptate) along the tube to relax.

Explicit formulae are given for and τ_R in the next section. For typical nozzle geometries, print conditions and print materials, the residence time in the nozzle is found to be similar to the polymer reptation time[4]; hence the assumption of steady flow in the nozzle.

The melt is typically characterized by a dimensionless entanglement number

$$Z = \frac{M_w}{M_e} \qquad (4.2)$$

where M_w is the mass-averaged molecular weight of the melt and the entanglement molecular weight, M_e, is determined from linear rheology as shown later. It has been suggested that flow can disentangle a melt, thus reducing Z.[5,208] This effect is discussed in section 4.4.2.

After deposition, any flow-induced deformation of the polymer begins to relax in the absence of flow gradients. Now the deposited filament is exposed to the surrounding air and begins to cool. The model assumes axisymmetric cooling of the filament to some ambient temperature T_a according to a prescribed boundary condition at the filament surface. The boundary condition is defined by some prescribed cooling rate β. The temperature decay couples to the constitutive model via the polymer relaxation times; since diffusion is arrested at solidification, τ_d and τ_R both diverge at the glass transition temperature T_g.

For amorphous materials, if the glass transition occurs before the polymer has time to fully relax to equilibrium, then the model predicts a degree of residual alignment. The polymer configuration is characterized by tensor

$$\boldsymbol{A} = \frac{< \boldsymbol{RR} >}{2R_g} \qquad (4.3)$$

where **R** is the end-to-end vector of the polymer chain and R_g is the polymer radius of gyration. The trace of **A** defines the stretch of the polymer chain and the off-diagonal elements of **A** define the polymer's orientation. At equilibrium **A**=**I**. In a polar coordinate system, A_{rs} denotes alignment of the polymer in the flow direction. (Note that $\hat{r}$ is directed out from the centre of the filament, and $\hat{s}$ is directed in the direction of the flow.) Since A_{rs} evolves over time, we denote the time to reach the glass transition tg and the residual alignment that locked in at the glass transition is denoted

$$A_{rs}(t = t_g) = \bar{A} \qquad (4.4)$$

Determining the temperature dependence of the polymer relaxation times, as discussed in the next section, is key to calculating residual alignment. It is also clear that the molecular weight, or Z (Equation 4.2) plays a crucial role in the presence of residual stresses.

4.3.2 Rheology characterization

The model relies on only three parameters to predict the non-linear flow behavior of the melt. That is,

- the elastic plateau modulus, G_e,
- the entanglement molecular weight, M_e, and
- the relaxation time of a polymer chain segment between entanglements, τ_e.

These three parameters can be determined from linear viscoelasticity measurements as follows. The values of the parameters are given in Table 4.1.

Table 4.1
Model parameters for polylactic acid (TTS=Time-Temperature-Superposition; LVE=Linear Visco-Elastic; GPC= Gel-Permeation Chromatography)

Parameters	Notation	Value	Method
WLF parameters	C_1	2.88 °C^{-1}	TTS
	C_2	133.10 °C	TTS
	T_0	200 °C	TTS
Plateau modulus	G_e	4.44 x 10^5 Pa	LVE model
Entanglement molecular weight	M_e	9.0 kg/mol	LVE model

Entanglement time (at T_0)	τ_e^0	2.0 x 10^{-6} s	LVE model
Entanglement number	Z	19	GPC + LVE model
Polydispersity	p	2.2	GPC
Thermal diffusivity	α	5.8 x 10^{-8} mm^2/s	Ref[209]

Shift factors obtained from time–temperature superposition of the storage and loss moduli, G' and G'', respectively, are assumed to take the form of the Williams–Landel–Ferry (WLF) equation

$$a(T) = \exp\left(-\frac{C_1(T - T_0)}{C_2 + T - T_0}\right) \qquad (4.5)$$

where T_0 is the reference temperature, and C_1, C_2 are constants.[210] This shift factor governs how τ_d and τ_R diverge near to the glass transition; thus it is not necessary to explicitly define T_g in the model. Then, the linear rheology master curve (G', G'' at T_0) is fit to the Likhtman–McLeish theory[211] using RepTate software[212] to obtain G_e, M_e, and the entanglement time at the reference temperature, denoted τ_e^0. Note that the predicted M_e is in line with that reported in the literature.[213] The entanglement molecular weight is then used to determine the entanglement number, Z, via Eq. (2). Once the entanglement time scale is established, the temperature-dependence of the reptation and Rouse times is given by

$$\tau_R = Z^2 \tau_e^0 a(T) \qquad (4.6)$$

$$\tau_d = 3Z^2 \tau_e^0 \left(1 - \frac{3.38}{\sqrt{Z}} + \frac{4.17}{Z} - \frac{1.55}{\sqrt{Z^3}}\right) a(T) \qquad (4.7)$$

where $a(T)$ is given by Equation 4.5.

4.3.3 Temperature modeling

Axisymmetric cooling of the deposited filament is determined by solving heat equation:

$$\frac{\partial T}{\partial t} = \alpha \frac{1}{r} \frac{\partial}{\partial r}\left(r \frac{\partial T}{\partial r}\right) \qquad (4.8)$$

for thermal diffusivity α. The initial condition is $T = T_N$ (i.e., we assume the temperature remains uniform during the nozzle and deposition flow). We prescribe the boundary condition at the filament surface to be

$$T_s(t) = \frac{T_N - T_a}{2} exp(-\beta t) + T_a \qquad (4.9)$$

for some cooling rate β. This approach has been applied in previous works[3,152,205] and shows quantitative agreement with infra-red imaging measurements. Note that when the filament first touches the build plate, the temperature at the filament surface is assumed to be the average of the nozzle and bed temperature i.e. $T_s(t = 0) = (T_n + T_a)/2$.

We find empirically (Figure 4.3) that the cooling rate is related to the transverse velocity according to

$$\beta = b_1\sqrt{b_2 U_p} + b_3 \qquad (4.10)$$

for some constants b_1, b_2, b_3. This is the expected functional form for convection-driven cooling;[214] faster print speeds increase convection and therefore have a faster cooling rate.

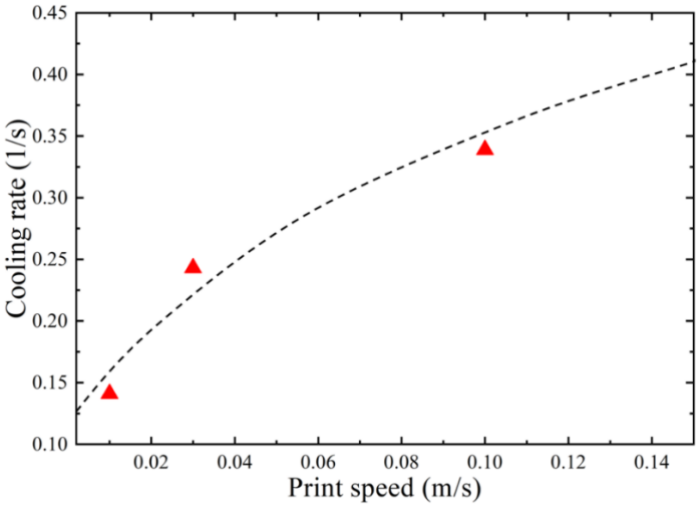

Figure 4.3. Experimentally measured (using infra-red imaging[205]) cooling rate of a deposited PLA filament of similar dimensions as a function of transverse print speed U_P. The data is fit to the functional form given in Eq. (4.10), used to represent convective cooling. We find that $b_1 = 0.39\ s^{-1}$, $b_2 = 5.28\ s^{-1}$ and $b3 = 0.06\ s^{-1}$.

4.4 Results

Here we demonstrate how increased print speed reduces the weld strength at filament-filament interfaces, as measured via the uniaxial tensile test described in Chapter 3.8. We attribute this reduced strength to residual alignment, denoted $\overline{A}$ (Equation 4.4). We present our observations of residual alignment within a printed wall of PLA, as measured using the birefringence technique discussed in Chapter 3.4, alongside the predictions from our MatEx model (Chapter 4.1). Further details of the correlation between weld strength and residual alignment are deferred to Chapter 4.4.

4.4.1 Reduced weld strength

Figure 4.4 demonstrates that the weld strength is less than the bulk strength of the material for all printing conditions. Moreover, there is a clear reduction in the weld strength as a function of print speed, and weld strength can be improved by increasing the nozzle temperature. Not only does increasing the temperature give more time above the glass transition temperature, it enables the polymers to relax faster. Thus, it is expected that filaments printed at higher temperatures are more isotropic and consequently have stronger welds. Birefringence measurements enable us to explore this hypothesis experimentally.

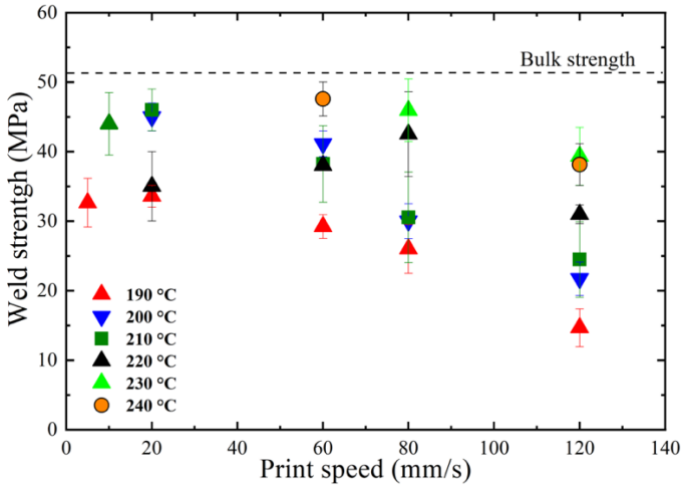

Figure 4.4. Weld strength measured using uniaxial tensile test (ASTMD1938) as a function of print speed for a range of nozzle temperatures, Weld strength decreases with increased print speed and reduced nozzle temperatures.

4.4.2 Observation of residual alignment

Figure 4.5 shows a polarized optical microscopy image of a single filament printed wall; the image focuses on 5 filaments. Bright regions correspond to filament–filament interfaces and indicate that the polymer is oriented near to the welds. On the other hand, dark regions in the centre of each filament indicate that the polymer is isotropic. There is a small difference in the width of the oriented region, with the lower-temperature case showing a wider birefringent area.

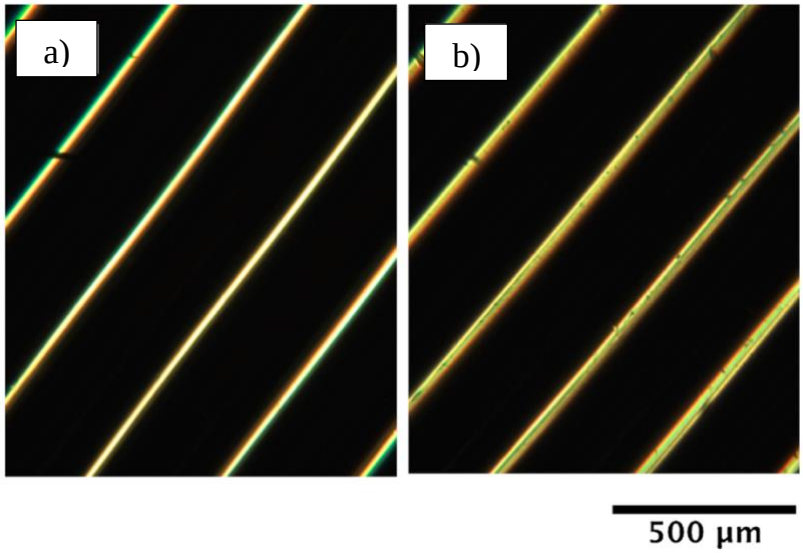

Figure 4.5. POM micrograph, under crossed polarizers of several printed filaments for (a) T_N = 240 °C, U_N = 120 mm/s and (b) T_N = 190 °C, U_N = 120 mm/s. Bright regions indicate polymer orientation, and correspond to filament-filament interfaces, whereas dark regions indicate isotropy at the centre of the printed filaments.

Figure 4.6 shows the degree of apparent birefringence for a range of printing conditions. At low nozzle temperatures (T_N = 190–210 °C), the apparent birefringence increases linearly with print speed. For higher nozzle temperatures, lower apparent birefringence values are obtained and there is little dependence on print speed.

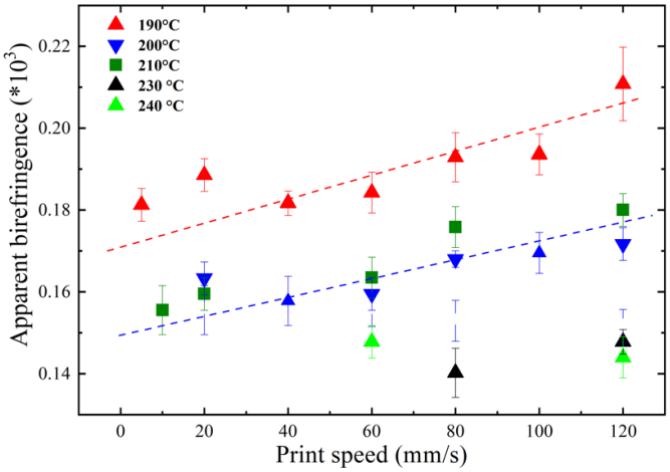

Figure 4.6. Apparent degree of birefringence in the weld as a function of print speed for a range of different nozzle temperatures. Increased birefringence corresponds to an increase in residual alignment at fast print speeds and low nozzle temperatures.

Since birefringence traces molecular orientation, it is evident that anisotropy persists in the weld region. To verify that the observed birefringence is related to the presence of amorphous oriented chains, rather than crystal fractions, calorimetric analysis was carried out on the printed samples to determine the sample crystallinity. These tests showed the presence of approximately 2–3% crystal phase by weight, over the total quantity of material, which may possibly be induced by the flow.[152,205] However, by comparing the thickness of the birefringent region with respect to the filament, we find that the oriented region typically represents more than 12% of the total thickness (unlike the 2–3% of the crystallinity identified at the DSC).

4.4.3 Model predictions

Figure 4.7 shows the predicted residual alignment locked in the glass transition within a filament cross-section, as predicted by our numerical model. We show results for two print speeds, U_N = 20 and 120 mm/s, at nozzle temperature T_N = 190 °C. Although the polymers at the centre of the filament are isotropic at solidification, there is insufficient time for polymers near to the filament surface to relax to equilibrium before the onset of the glass transition. Thus, we observe a thin boundary layer of residual alignment, which is more prevalent at the bottom of the filament (due to the 90 degree turn during deposition[4]). Moreover, a larger degree of alignment can be seen for the faster print speed. This is in agreement with the birefringence results shown in Figure 4.6. Since we are interested in how this anisotropy affects welding, next we present how this alignment evolves during cooling within the weld region, defined to be at z = 0. Figure 4.9 shows the evolution of the temperature, the polymer stretch

$$\Lambda = \sqrt{trA/3} \qquad (4.11)$$

and the alignment A_{rs}. First, we note how filaments printed at faster speeds cool faster due to the imposed boundary condition (Equation 4.10) which represents increased convection for faster print speed. Next, we note how faster printing imposes a greater initial polymer stretch and degree of alignment. Stretch relaxes on the order of the Rouse time (Equation 4.7) and has sufficient time to equilibrate before the glass transition. However, reptation is much slower and reorientation of the polymers is arrested by the glass transition, even for the slowest print speed, leading to residual alignment in the weld region. It is clear that the increased residual alignment with print speed is due to two factors:

1. a greater initial degree of alignment during flow through the nozzle and deposition, and
2. faster cooling leading to less time above the glass transition temperature.

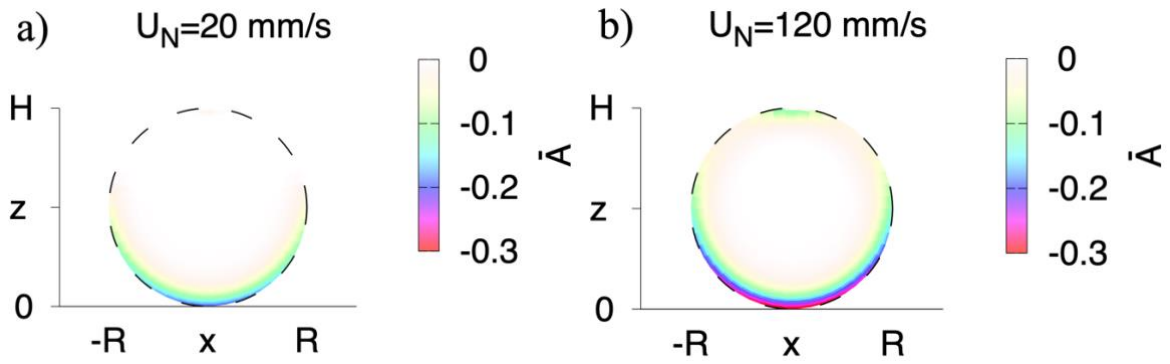

Figure 4.7. Degree of residual alignment, A_{rs} locked in at the glass transition over the cross-section of a deposited filament printed T_N = 200 °C for print speed (a) U_N = 20 mm/s and (b) U_N = 120 mm/s. The model predicts that the residual stress is localized in a thin boundary region near to the filament surface and increases with print speed.

Figure 4.8 shows the final degree of alignment $\overline{A}$ at the weld as function of print speed for three nozzle temperatures T_N = 190, 200 and 210 °C. The trends we observe with respect to the print conditions are evidently similar to those we report in terms of weld strength (Figure 4.4) and birefringence (Figure 4.6). That is, there is an increase in $|\overline{A}|$ and the degree of birefringence with increased print speed suggesting that increased residual anisotropy reduces weld strength; this effect can be reduced by increasing the nozzle temperature.

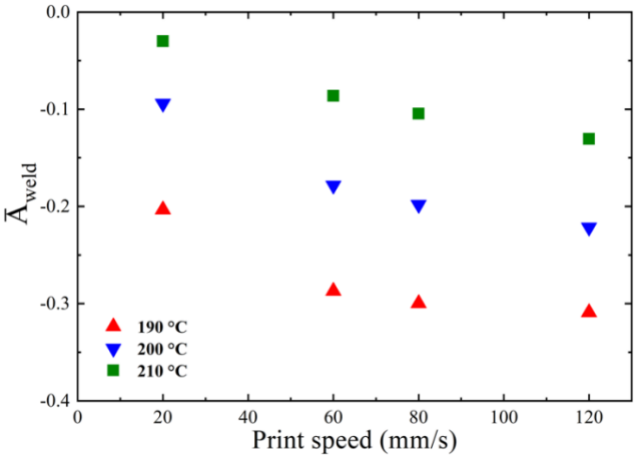

Figure 4.8. Final degree of alignment in the weld region (at z = 0) locked in the glass transition as a function of print speed for various nozzle temperatures.

4.5 Discussion

Here we discuss the correlation between $\overline{A}$ and the experimentally measured apparent birefringence and weld strength. We also discuss additional factors, namely the inter-diffusion depth and entanglement fraction, which may also contribute to a reduced weld strength.

4.5.1 Alignment vs strength

Figure 4.10a clearly shows a linear relationship between $\overline{A}$ and the degree of apparent birefringence, Δn, in general agreement with the stress optical rule; we find that the shear stress $\sigma = G_e\overline{A}$ is related to the degree of apparent birefringence via

$$\Delta n \; \alpha \; C_0|\sigma| \qquad (4.12)$$

where $C_0 \approx 0.3$ GPa^{-1}. This is lower than the stress optical coefficient reported in the literature for PLA films.[215,216] However, discrepancies may be expected due to relating the measured apparent birefringence for this 3D-printed wall geometry to the actual birefringence value at the weld.

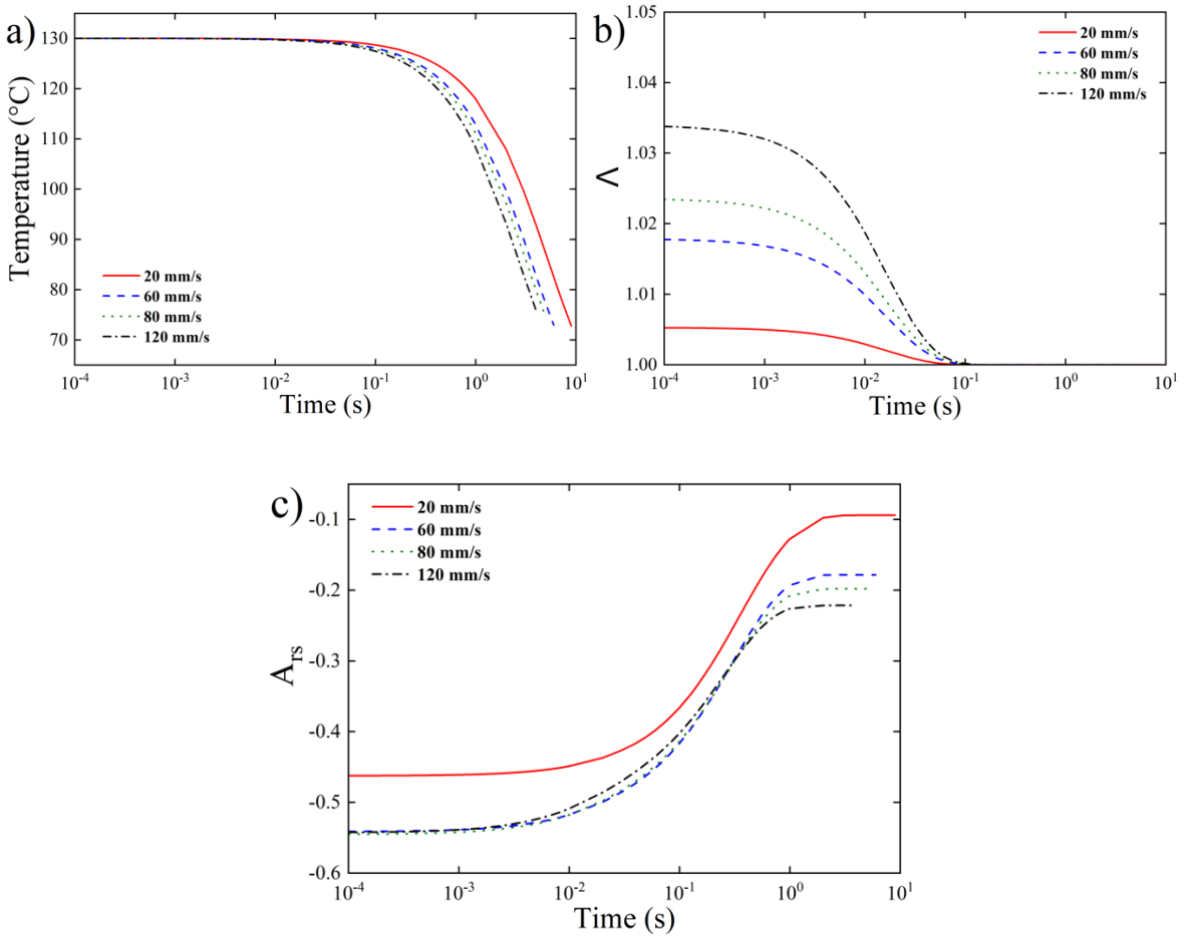

Figure 4.9. Evolution of (a) temperature, (b) the polymer stretch and $\Lambda = \sqrt{trA/3}$ *and (c) the orientation component,* A_{rs} *at the weld (z=0) predicted by the numerical model for increasing print speed at fixed nozzle temperature* T_N*= 200 °C.*

Furthermore, the degree of birefringence is shown to reduce weld strength linearly (Figure 4.10b). This suggests that even a small degree of residual alignment will reduce the strength at the weld, which we can predict via this empirical relation. These correlations between $\overline{A}$, the degree of birefringence and the weld strength form a basis for developing more advanced theories to relate residual alignment to mechanical properties. It is clear from our results that slower print speed and higher nozzle temperatures are favorable for preventing the entrapment of orientation at the glass transition. However, practically higher nozzle temperatures can lead to degradation, and slower print speeds reduce productivity. Thus, there is precedent for employing a post-printing thermal annealing process[205,217] to remove these residual stresses. The appropriate annealing time and temperature can be chosen by inspection of the tube model parameters (Table 4.1), in particular the reptation time.

On the other hand, in some instances polymer alignment may be a desirable property for an FFF-printed part to tune electrical and mechanical properties. Furthermore, since PLA is a

semi-crystalline polymer, thermal annealing under the correct conditions can also be employed to enhance crystallinity[205]; alignment from the printing flow leads to 'templated' flow-enhanced nuclei, which grow into smaller spherulite structures that exhibit more ductile fracture.

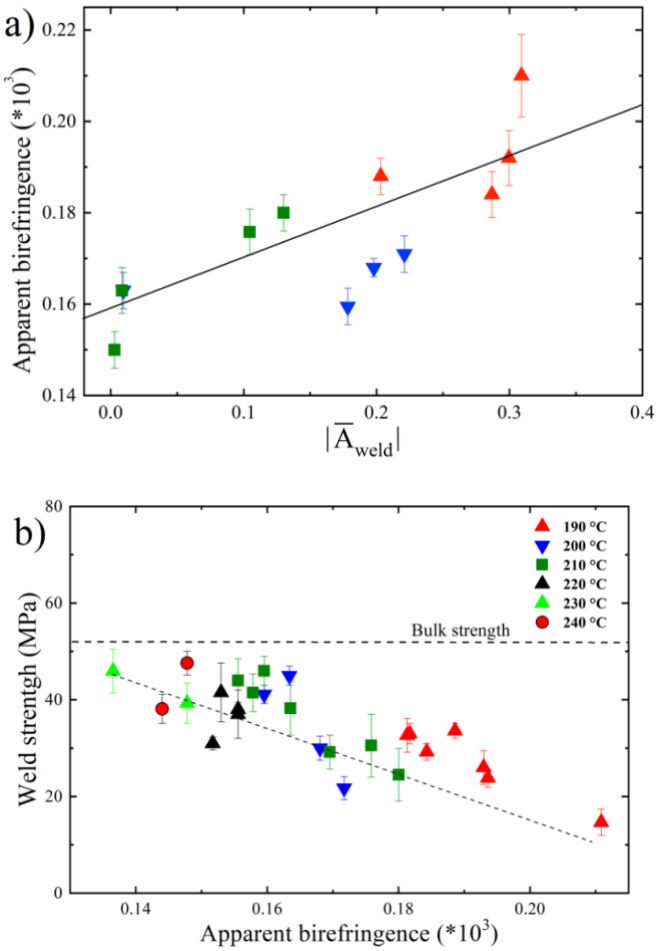

Figure 4.10. (a) The degree of apparent birefringence measured experimentally, Δn, plotted against the final degree of alignment, $\bar{A}$, in the weld region predicted by the model (as in Figure 4.8). The line of best fit is linear. (b) Experimentally measured weld strength, G (as in Figure 4.4), as a function of the degree of apparent birefringence (as in Figure 4.6). Line shows best fit. Bulk strength is approximately 52 MPa.

4.5.2 Interdiffusion and entanglements

Successful welding in MatEx is first and foremost reliant on diffusion of the polymer molecules across the filament-filament interfaces. This interdiffusion process creates interfacial entanglements, which increase the strength across the weld line.[218] Here we denote the final interpenetration depth defined at the glass transition by $\bar{\chi}$. It is expected that if the polymer

diffuses its radius of gyration during cooling, i.e., $\bar{\chi}/R_g > 1$ then bulk strength will be achieved in the weld region. It has previously been shown that the interpenetration depth can be approximated by[3]

$$\frac{\overline{\chi}}{R_g} = \left(36 \int_0^{t_g} \frac{1}{\tau_d\big(T(t)\big)} \big(1 - (A_{rr}(t) - 1)\big) \right)^{\frac{1}{4}} \qquad (4.13)$$

The term containing A_{rr} accounts for anisotropic diffusion due to alignment in the flow direction in the weld region (z = 0). Figure 4.11a shows the model predictions for $\overline{\chi}$ as a function of print speed and temperature). We see that for this material, and the range of print conditions considered here, there is always sufficient time prior to the glass transition to achieve adequate diffusion. Similar behavior has also been predicted for polycarbonate.[3] Thus, we propose that reduced weld strength is not due to insufficient diffusion depths, but to the configuration of the entanglement network itself. Indeed, as described in the introduction, generally fracture of glassy polymers is governed by the number of 'interfacial' entanglements that act to anchor chains across the tear.[219] Here we consider the recently proposed mechanism of flow-induced disentanglement of the network due to convective constraint release (CCR). In the tube model, CCR is the mechanism of neighboring chains reptating away due to thermal motion and thereby "releasing a constraint". At equilibrium, chains that reptate away are readily replaced by new chains, thus the number of entanglements remains constant. On the other hand, under flow there is an argument for CCR leading to a reduction in the number of entanglements.

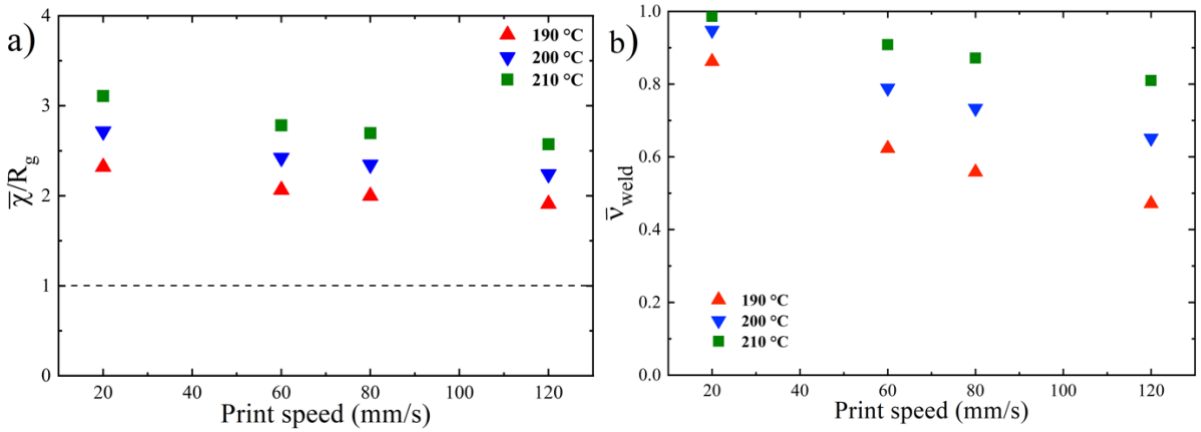

Figure 4.11. (a) Final interpenetration depth, $\bar{\chi}/R_g$, as estimated by Equation 4.13 at solidification as a function of print speed for various nozzle temperatures. Bulk strength is expected for $\bar{\chi}/R_g > 1$. (b) Final degree of entanglement,$\bar{v}$, predicted by the model in the weld region (at z = 0) at solidification.

A previous work[3] employed the model of Ianniruberto[5] to account for changes in the entanglement fraction, denoted v, due to the flow field. MatEx printing flow is found to significantly disentangle the polymer network, i.e., $v \ll 1$. Moreover, there is an insufficient time for entanglements to recover to equilibrium ($v = 1$) during typical cooling. This leads to a partially-entangled melt at solidification, which is expected to be weaker than the bulk material. Figure 4-11b shows the predicted results when flow-induced disentanglement followed by recovery during cooling is incorporated for the PLA material and printing conditions considered here. In particular, we find that the entanglement fraction locked in at the glass transition within the weld region (z = 0) decreases with increasing print speed and reduced nozzle temperature. Having a prediction of the reduced entanglement fraction within a MatEx-printed weld, we refer to the molecular interpretation of the toughness of glassy polymers.[220,221] Typically glassy polymers fail in the crazing regime, where the toughness is shown to vary with the density of entangled chains per unit of craze area. Since the failure we observe in this work is brittle (showing no large plastic deformation), we propose a similar mechanism for PLA. Future work will focus on confirming this via a morphological investigation into the failure mechanism of printed PLA. Thus, we modify this classic result[220,221] to account for a partially entangled network prior to fracture; the final degree of entanglement at the weld can be related to the weld fracture toughness via Equation 2.3. This approach has been applied in previous work[3], but a comparison to experimental data is not made. Figure 4.12 shows the predicted weld fracture toughness for the conditions considered in this work (lines). These results are quantitatively similar to that measured experimentally (points).

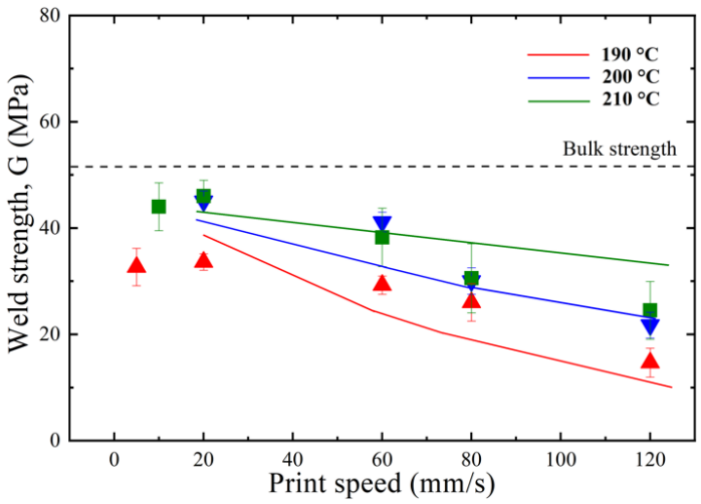

Figure 4.12. Weld fracture toughness, G as predicted by the model (Eq. (13) with q = 0.35) (lines) and measured experimentally (points) as in Fig. 3. Results are shown as a function of print speed for various nozzle temperatures. Bulk toughness is approximately 52 MPa.

4.6 Conclusions

For the first time, we have measured molecular orientation in a simple MatEx-printed object using birefringence. In particular, residual orientation of the polymer chains due to the printing flow is found to be localized to the weld regions between printed filaments. In contrast, the bulk of each filament is isotropic. There is a distinct decrease in weld strength with the increase of birefringence measured at the weld, which can be improved by increasing the nozzle temperature or reducing the print speed.

Our birefringence measurements can be directly linked to an alignment factor predicted by a molecularly-aware non-isothermal model of the MatEx process.[3] The model confirms that polymer chains become oriented in the flow direction due to shear in the nozzle combined with the subsequent deposition process. Since the filament center experiences less severe velocity and temperature gradients, flow- induced deformation can fully relax prior to solidification. On the other hand, the filament surface is subject to greater shear and cooling rates and there is insufficient time for any flow-induced orientation to relax before the onset of the glass transition. We find that the predicted residual alignment factor at the weld, $\overline{A}$, is linearly proportional to the measured degree of apparent birefringence, Δn, in agreement with the stress-optical rule.

Furthermore, contrary to what is commonly expected, our model shows that weld strength is not limited by inter-diffusion of the polymer molecules across filament-filament interfaces; instead weld strength is affected by the (non-equilibrium) configuration of the entanglement network itself. By relating the degree of residual alignment to partial entanglement of the polymer chains at solidificationi[5], we can predict the measured weld toughness via a modification to classic fracture theory of glassy polymers.[220,221] Thus, this model may be used as a tool for choosing appropriate printing conditions based on a toughness threshold.

Interestingly, the trend of decreasing weld strength with increasing print speed is not apparent for ABS.[139] Unlike PLA, which can be characterized as a linear polymer and obeys classic Doi-Edwards tube theory, ABS has a more complex microstructure that includes cross links and contains rubber nano-particles. Indeed, the rheology shown[139] is consistent with some very slow relaxing material in this sample. We'd expect this element of the material to behave affinely (or very close to this) under flow, leading to no dependence on the flow rate. The PLA material investigated here behaves very differently because its relaxation rates are comparable to the flow rates during printing. In future work, we will extend our analysis to other thermoplastic materials and consider the effect of molecular weight.

4.7 Appendix

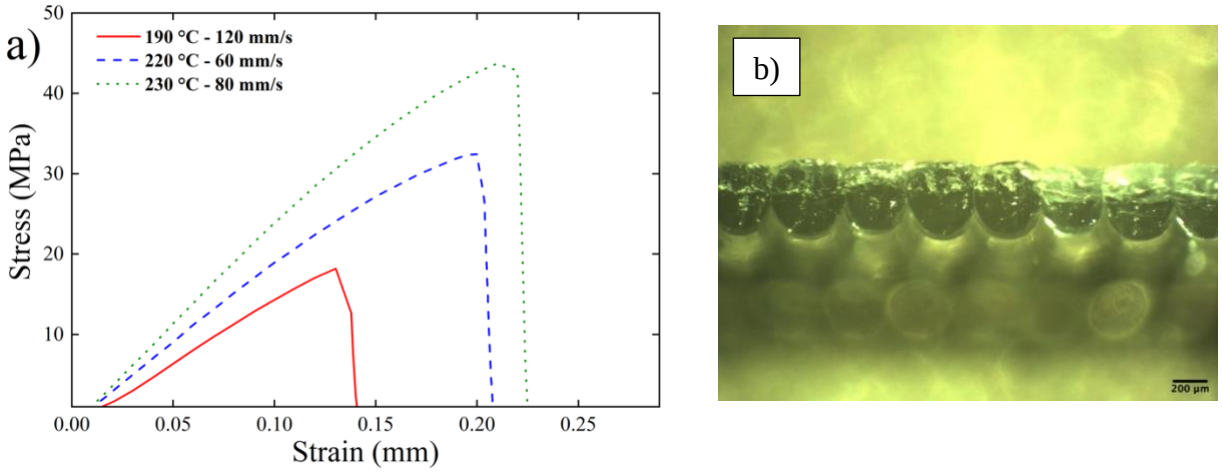

Figure 4.13. (a) representative stress- strain curves for PLA 4043 for different printing conditions demonstrating that the maximum stress and stress at break are equivalent in this case; (b) An example of a micrograph of the contact thickness obtained at the stereoscope for a PLA 4043D samples printed at 210 °C and 20 mm/s.

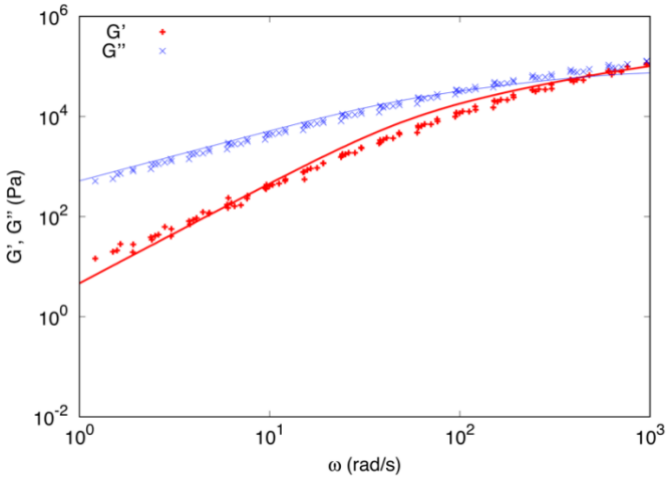

Figure 4.14. Linear rheology master curve for PLA 4043D measured at reference temperature T_0 = 200 °C (points) is fit to Likhtman-McLeish theory (lines).

5 EFFECT OF MOLECULAR WEIGHT ON WELD STRENGTH

5.1 Introduction

In this chapter, we investigate the interlayer strength achieved for a range of poly-lactic feedstock with varying average molar mass, confirming that molar mass has a strong effect, with strength decreasing significantly with increasing entanglement number. By using a combination of infrared-microspectroscopy and a continuum modeling, we find that this difference is due to the presence of molecular anisotropy at the weld region for the high molecular weight material, while the low molecular mass materials show isotropy.

5.2 Thermal and rheological characterization

DSC cooling and heating ramps at 10 °C/min for all the investigated materials (see Chapter 3.3) are reported in Figure 5.1. As demonstrated by the DSC calorimetric analysis, these materials exhibited a different behavior as the percentage of D-lactide comonomer varied. A higher percentage of monomer, in fact, strongly limited the possibility of the materials to crystallize, making their structure totally amorphous upon standard cooling condition.

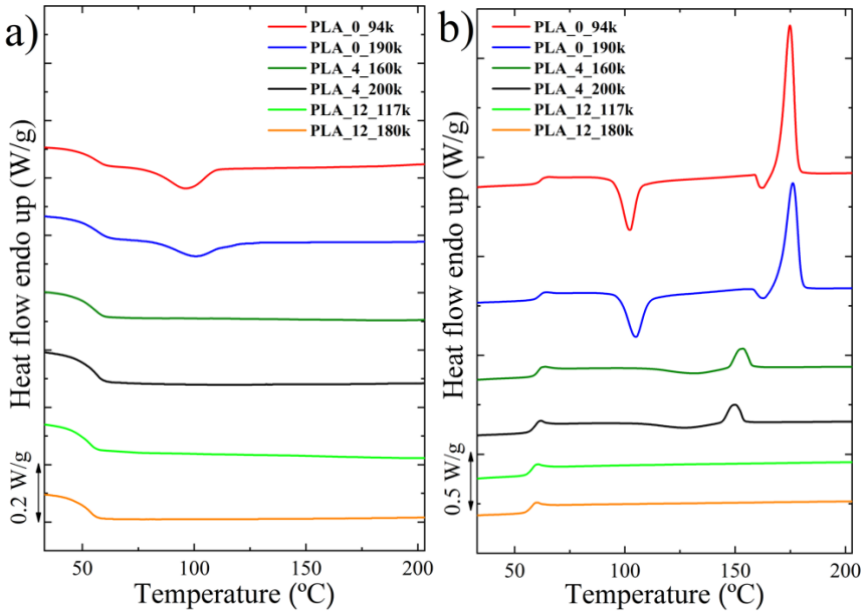

Figure 5.1. Cooling ramp (a) and heating ramp (b) obtained by DSC calorimetric analysis for the six materials.

Conversely, the absence of D-lactide monomer units in the polylactic acid chains allowed obtaining a semi-crystalline structure. The final degree of crystallinity thus decreased with increasing comonomer amount. On the other hand, at the same comonomer level, a variation of the molar mass did not meaningfully affect the thermal behavior of the material.

Complex viscosity curves obtained with temperature–time superposition analysis at the reference temperature of 190 °C for all materials are reported in Figure 5.2a.

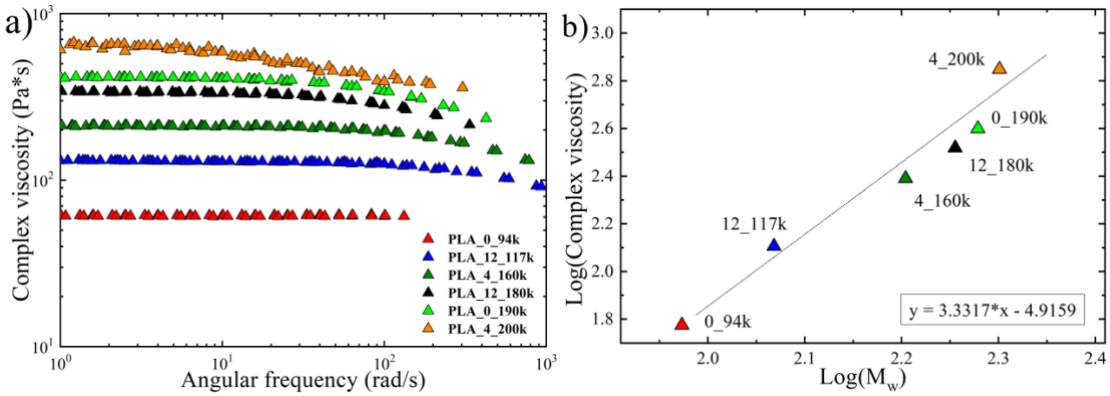

Figure 5.2. (a) Complex viscosity obtained with temperature-time superposition analysis at the reference temperature of 190 °C as a function of the angular frequency for all materials, (b) Logarithm of the Newtonian viscosity as a function of the logarithm of molar mass.

It can be observed that for all materials the complex viscosity initially remains constant as the angular frequency varies (Newtonian plateau), up to a certain value after which the viscosity begins to decrease. As expected, viscosity increases with molecular mass, while the D-lactide content does not seem to influence its behavior. This can be verified when the logarithm of the Newtonian viscosity is plotted as function of the logarithm of molar mass. As can be seen in Figure 5.2b, the data approximately follow one straight line with a slope close to 3.4, confirming that molar mass is the relevant variable which governs the viscosity, in agreement with previous literature.[222–224]

5.3 Mechanical testing

Figure 5.3a shows an example of stress/strain curves for PLA_4_200k samples printed with a nozzle temperature of 200 °C and different print speeds. The stress to which the samples are subjected is calculated by dividing the for the area of the weld region previously measured for each sample by using a stereoscope. It is evident that, under the chosen nozzle temperature

conditions, the elongation at break and the stress at break decrease with increasing printing speeds. Figure 5.3b shows two examples of broken samples after mechanical testing, related to PLA_4_200k and PLA_0_94k both printed at 210 °C and at similar rates (20 mm/s and 60 mm/s, respectively). In the case of the high molar mass polylactide, the breaking occurs completely along the weld line, so the tensile test can be considered as representative of the weld strength. In the second case, for low molar mass polylactide, the fracture line seems to resemble a bulk-type breaking, spanning more than one weld line, and beginning in the area of the clamps. These pictures are representative of the prevailing failure mechanism of high and low molar mass samples, respectively.

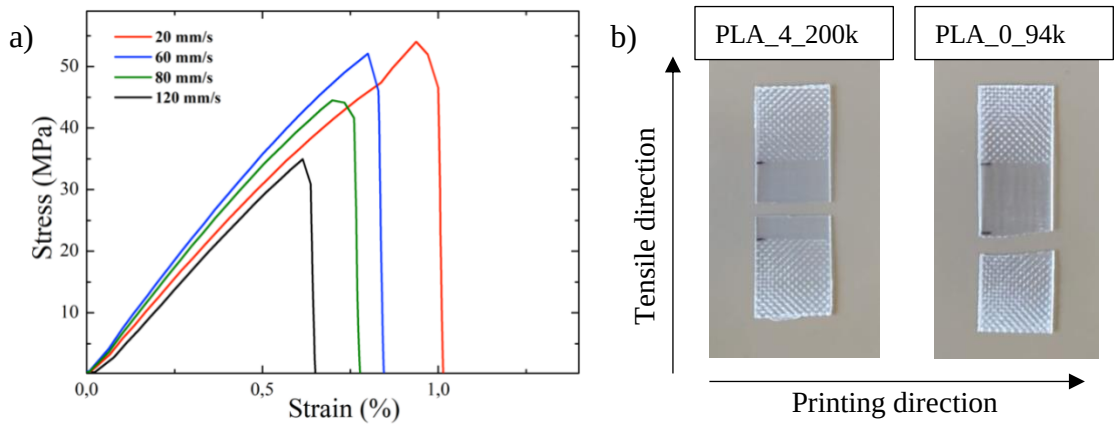

Figure 5.3. (a) Examples of stress/strain curves for PLA_4_200k samples printed at 200 °C at different print speeds and for the sample obtained by compression molding; (b) Examples of fractured samples following mechanical tensile testing for PLA_4_200k and PLA_0_94k.

Figure 5.4 summarizes, as examples, the weld strengths, i.e., the maximum stress in the stress-strain curves, for PLA_0_94k, PLA_12_117k and PLA_4_200k measured at different printing conditions. The shaded yellow areas in each graph corresponds to the range of bulk strength values measured using dog-bone shaped specimens obtained by compression molding.

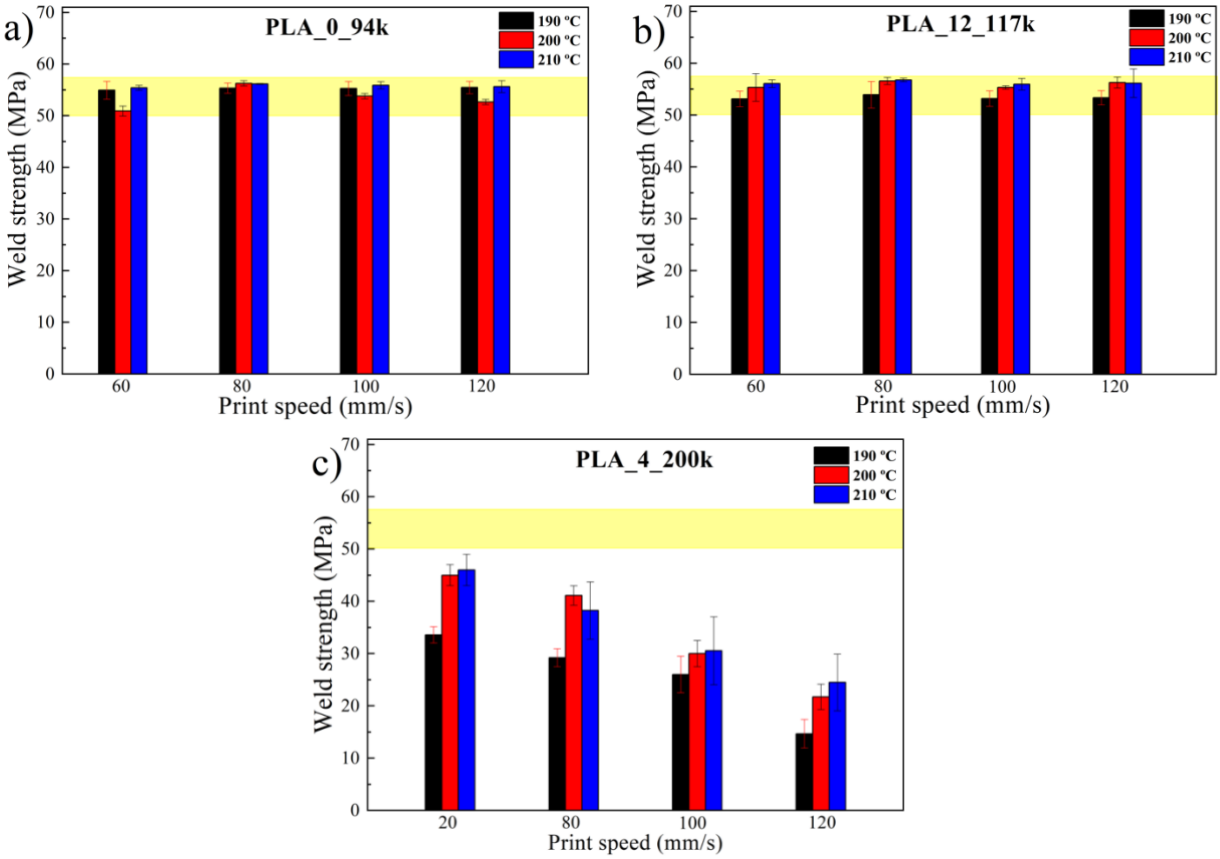

Figure 5.4. Weld strengths as a function of printing conditions for (a) PLA_0_94k, (b) PLA_12_117k and (c) PLA_4_200k. The shaded yellow areas in each graph corresponds to the range of bulk strength values measured using dog-bone shaped specimens obtained by compression molding.

Observing the plots (comparing Figure 5.4a and 5.4b), it is easy to see that the percentage of D-lactide monomer has little influence on the final mechanical properties. The weld strength is instead closely related to the molecular mass of the material. In fact, the weld strength of the low molecular weight materials does not seem to be influenced by the processing conditions: in the case of PLA_0_94k, the weld strength values are approximately constant with extrusion temperature and print speed. This contrasts to the sample of highest molecular weight, PLA_4_200k, for which there is a distinct decrease in mechanical properties with stronger printing parameters (lower nozzle temperatures and higher deposition rates); it can be seen that increasing the nozzle temperature improves the adhesion strength.

Since the bulk strength of a polymer is known to typically increase with molar mass[225,226],and in general we observe that low molecular weight samples achieve a greater tensile strength, this suggests that the printing process is affecting the underlying microstructure within the weld region. We propose that the decrease in weld strength we observe is caused by residual chain

orientation at the interface, as discussed in Chapter 3. Indeed, residual orientation at the glass transition is expected to increase with molar mass and print speed, and to decrease with increasing nozzle temperature. To test our hypothesis, in the next section we measure the anisotropy in the weld region using polarization modulated infrared microspectroscopy. These results are further supported by model predictions of residual alignment in the weld, which we then compare directly to our weld strength measurements.

5.4 Measuring weld anisotropy

To confirm that the decay of the tensile stress as a function of print speed for high molar mass sample is due to a residual orientation of polymer chains at the interface between the layers, polarization modulated infrared microspectroscopy was used. These measurements were carried out on two materials possessing the highest and the lowest molar mass, namely PLA_4_200k and PLA_0_94k, respectively.

Figure 5.5a shows a representation of the microtoming cut made on the two printed samples. The samples were microtomized in a direction parallel to that of printing, thus obtaining slices of filaments with a thickness of 5 μm. It should be underlined that the manual microtoming procedure, with the difficulties of handling the small samples, did not allow to cut the printed objects exactly through the center of each layer. As such some uncertainty in the vertical position of the slice within the layer exist, which forces us to take measurements from three slices per sample to obtain representative results. Figure 5.5b shows an example of visible light image of a microtomed section from PLA_4_200k printed at 20 mm/s and 210 °C seen under the confocal IR microscope before the PM-IR scan.

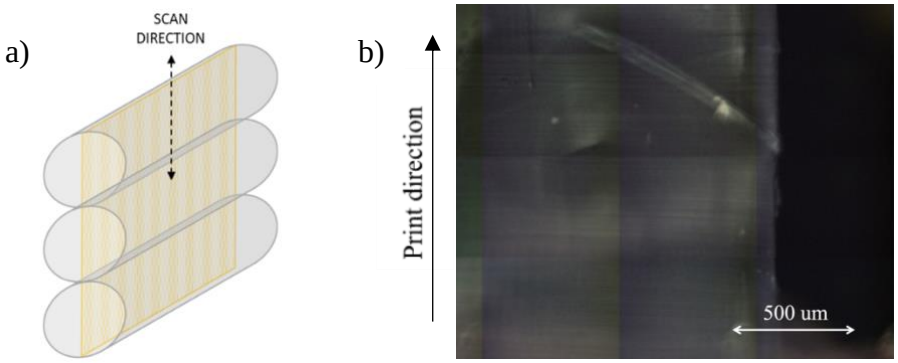

Figure 5.5. (a) Sketch of the microtoming operation that has been adopted for preparing the samples for the PM-IR measurements; (b) an example of a PLA_4_200k sample printed at 20 mm/s and 210 °C to be scanned with PM-IR.

Figure 5.6 shows an example of two polarization modulation dichroic difference spectra measured for a sample of PLA_4_200k and one of PLA_0_94k printed at 210 °C using a speed of 20 mm/s and 60 mm/s, respectively. It is evident that the PMDD differential absorption spectra are very different for the two materials. For the low molecular weight material, the PMDD intensity remains close to zero for all the measured range of wavenumbers. In contrast, the spectrum of PLA_4_200k shows more anisotropic absorbance as evident by stronger intensity positive and negative bands at precise wavenumbers, which indicate the presence of molecular anisotropy. The peak appearing at approximately 1383 cm^{-1}, which corresponds to the symmetric deformation of the CH_3 group,[227] is chosen as a reference band to evaluate the PMDD intensity in different regions, due to its sensitivity to molecular orientation.

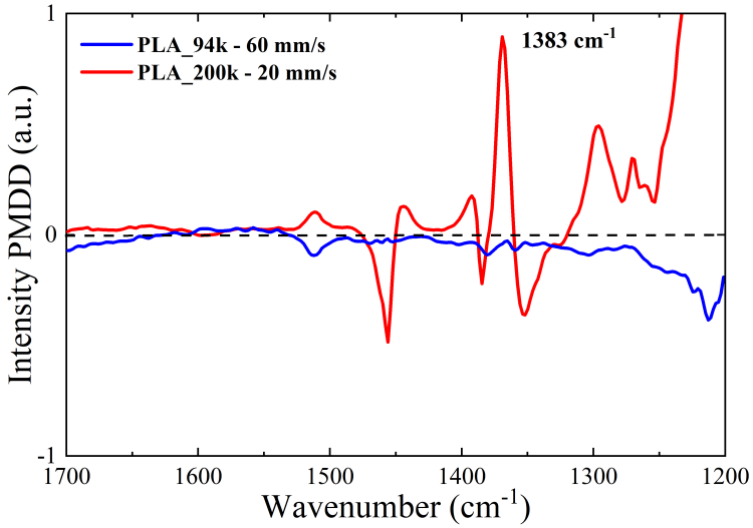

Figure 5.6. Comparison of the PMDD spectra acquired for PLA_4_200k and PLA_0_94k.

Figure 5.7 reports the PMDD intensities calculated for the two materials as a function of the position in the sample. In both cases the acquisition of the spectra started from outside the sample, thus presenting a clear separation surface between the air and the material itself. For the case of PLA_4_200k (Figure 5.7a) it can be noted that, moving towards the central region of the sample, there is a net increase in intensity, which remains at high levels for a length of about 200 µm, and then falls again. This behavior, on the other hand, does not occur in the case of low molar mass PLA, for which, throughout the thickness analyzed, there is no meaningful variation in intensity (Figure 5.7b).

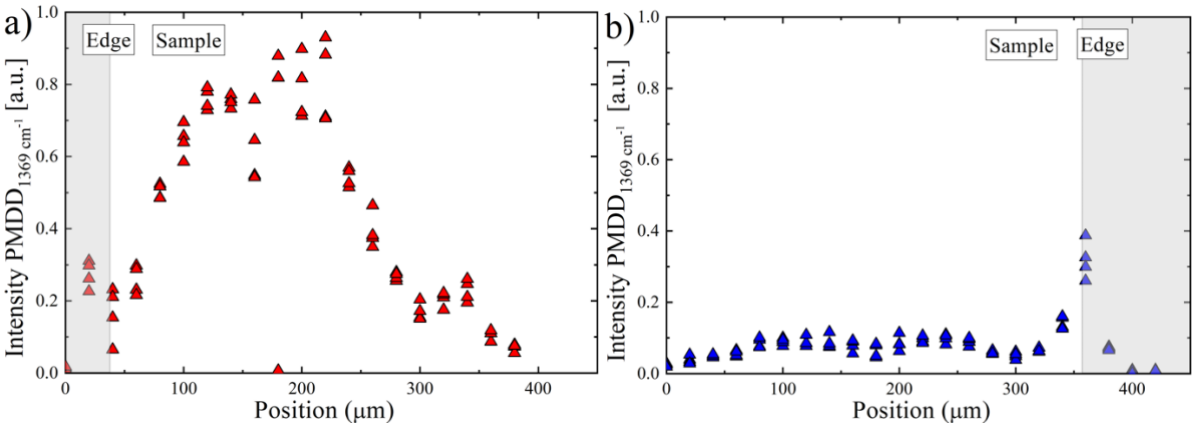

Figure 5.7. PMMD intensity for (a) PLA_4_200k and (b) PLA_0_94k as a function of position in the sample. Dark areas highlighted on the plots correspond to the air-sample interface.

The results of these measurements allow us to highlight the different degree of molecular anisotropy that develops in the two materials during the printing process and is frozen in at solidification. For the lower molar mass PLA_0_94k sample, no residual orientation is measured after the printing process, while for PLA_4_200k a measurable and spatially dependent degree of anisotropy is observed. We expect that this highly oriented region corresponds to the interface between the different layers (as predicted by the model), however due to the imprecision in the microtoming process, this is difficult to be confirmed.

5.5 Modelling weld anisotropy

To support our hypothesis, molecularly aware modelling of the FFF processing of our selected materials subject to the chosen printing conditions was carried out; here we show results for fixed print speed 120 mm/s and the temperature range 190-210 ˚C. We refer the reader to previous works for full details of the model, which has been applied to various materials.[3,4]

In summary, we model flow through the heated nozzle followed by deposition of a single cylindrical filament with an appropriate constitutive equation (Rolie-Poly) that captures the dynamics of a linear monodisperse polymer melt. This flow deforms the microstructure so that the polymers become stretched and aligned in the direction of deposition; we assume that this alignment reduces the entanglement of the polymer network. As the flow is dominated by shear

in the nozzle, the model predicts higher degrees of deposition near the surface of the deposited filament.

Upon deposition, the filament is cooled by employing the heat equation with an axisymmetric boundary condition. This boundary condition is determined from experimental measurements of a typical cooling profile according to the material and printing conditions. Here the velocity gradients cease, the flow-induced deformation begins to relax and entanglements reform according to the constitutive model. We infer that the polymers will begin to diffuse at a layer-layer interface via reptation. Once the glass transition temperature is reached, this diffusion/relaxation/re-entanglement process is arrested. This is captured in the model via a simple WLF dependence of the polymer relaxation times with the equation 4.3.

At this point we probe the state of the weld region (i.e., the surface of the deposited filament) via three molecular features: the degree of alignment, the degree of entanglement and the degree of interdiffusion (not reported). We find that the degree of interdiffusion always exceeds the polymers' radius of gyration for all the values of Z_{eq} (corresponding to the different molar masses). The degree of alignment and the degree of entanglement are plotted in Figure 5.8 for our samples of varying molecular weight for print speed 120 mm/s and a range of nozzle temperatures. The molecular weight of the material corresponds to an equilibrium entanglement number of the melt $Z_{eq} = M_w/M_e$, where M_e is the molecular weight of a single section between entanglements, which is obtained from fitting the rheological master curve to the Likhtman-McLeish theory via RepTate software.[212] We find that the degree of alignment and therefore the degree of disentanglement increases strongly with increasing molecular weight. This is a direct consequence of polymer reptation time scaling with the entanglement number via

$$\tau_d \propto Z_{eq}^3 \qquad (5.1)$$

That is, higher molecular weight samples (e.g., $Z_{eq} = 22$) have a significantly longer reptation time, meaning that not only do they deform more during the deposition flow, but the time to relax back to an isotropic state is much longer. Consequently, a greater degree of molecular anisotropy is trapped in at solidification. This is in contrast to low molecular samples (e.g., $Z_{eq} = 10$), which have sufficient time to fully relax before the onset of the glass transition, so that the weld region is isotropic on solidification. The print temperature has the biggest influence on this behavior. As shown in Figure 5.8, the degree of molecular anisotropy in the

weld region can be significantly reduced by increasing the print temperature. This is due to the temperature dependence of the reptation time:

$$\tau_d \propto a(T) \qquad (5.2)$$

which diverges exponentially near to the glass transition temperature according to the WLF equation. As the reptation time is not affected by shear, print speed has only a small effect on these results. By comparing Equations 5.1 and 5.2, clearly it is more effective to control the polymer reptation time, and therefore anisotropy in the weld, by adjusting the entanglement number of the melt via the molecular weight opposed to managing the temperature profile during this hard to control non-isothermal process.

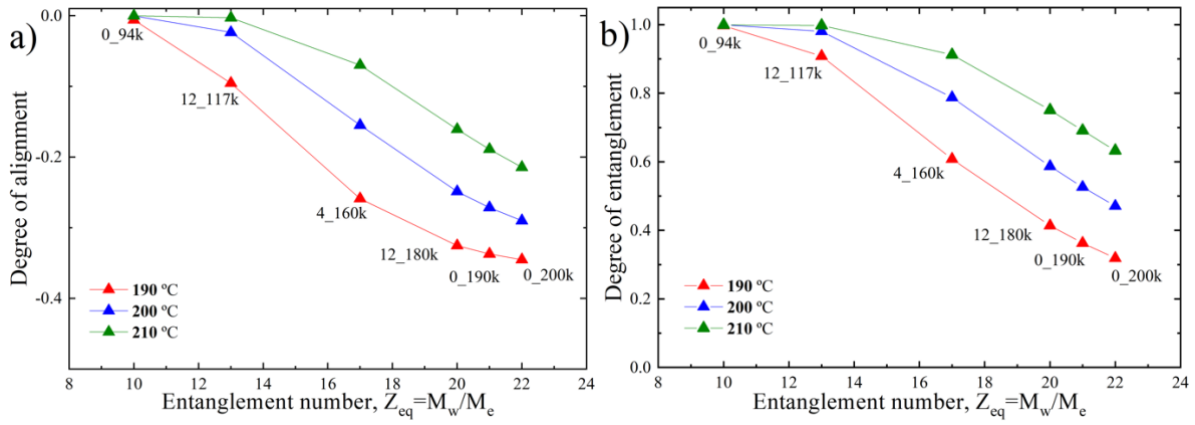

Figure 5.8. (a) Degree of alignment and (b) degree of entanglement calculated for different nozzle temperature as a function of $Z_{eq} = M_W/M_e$.

5.6 Modelling vs experiments

Figure 5.9a reports the weld strength for samples measured at 200 °C and 120 mm/s as a function of the entanglement number $Z_{eq} = M_w/M_e$ for all the investigated materials. The observed trend confirms that high molar mass PLAs are characterized by a lower weld strength than lower masses. Moreover, the trend is in line with the degree of entanglement calculated by the model and displayed in Figure 5.9b. It is therefore possible to attribute the decrease of weld strength for higher molar mass to the presence of residual chain alignment at the weld region.

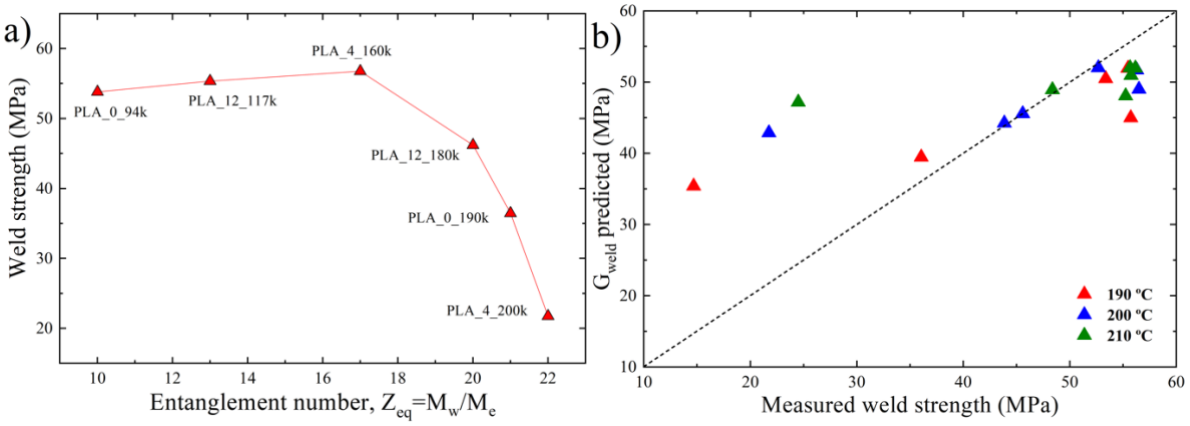

Figure 5.9. a) Weld strength measured for samples printed at 200 °C and 120 mm/s as a function of $Z_{eq} = M_w/M_e$); b) Gweld predicted with the model as a function of measured weld strength for all the explored nozzle temperatures and print speed.

The PM-IR molecular orientation measurements in the two materials shown in Figure 5.7 corroborate the modeling results reported in Figure 5.8a. In fact, the material with the highest molar mass and Z_{eq} number show the larger degree of chain alignment in the printing direction, while the residual alignment is negligible for the low molar mass sample, due to the intrinsically faster dynamic which allows the relaxation of any orientation before cooling below the glass transition temperature. Therefore, the counter-intuitive molar mass dependence on molecular weight shown in Figure 5.9a is captured by the molecularly aware-model, and is attributed to residual molecular alignment, as confirmed by PM-IR measurement on selected samples.

A comparison between the measured and predicted values of weld strengths is shown in Figure 5.9b. By assuming a fracture mechanism based on crazing,[228] the values of weld strength G_{weld} are calculated according to the Equation 4.3.

Figure 5.9b shows that there is good agreement between the model predictions and the experiments for the middle range of weld strength corresponding to the middle range of entanglement numbers. However, there is some discrepancy at the extremes.

There could be several reasons for this deviation.

1. The High Strength Regime. The model clearly underestimates the high strength regime, corresponding to the lowest molecular weight samples. This can be attributed to the

experimental temperature profiles employed by the model. Temperature measurements were carried out on the first deposited layer, which serve as an axisymmetric boundary condition in the model and provide the most extreme cooling profile experienced during the build. However, breaking occurs always at layers deposited at intermediate heights in the sample, where the cooling rate is less affected by the buildplate.

2. The Low Strength Regime. On the other hand, the model overestimates the weld strength in the low strength regime corresponding to the high molecular weight samples. This may be indicative of the unsuitability of the crazing model to properly describe the failure of PLA welds with frozen-in orientation. Another possible reason is the existence of a low degree of crystallinity at the weld, which could effectively decrease the strength of the inter-layer bonding.[202,229]

Despite this, the qualitative and semiquantitative agreement between Figure 5.8a and 5.9b suggests that the physics behind the phenomenon is correctly captured.

5.7 Conclusions

We investigated the interlayer strength achieved from a range of poly-lactic feedstock ranging in D-lactide content and average molar mass. Mechanical testing confirmed that molar mass has a strong effect, with strength decreasing significantly with entanglement number, whereas the effect of the D-lactide content is small. These measurements contrast expectations that increasing the number of entanglements increases the strength of a polymer, as evident in samples processed by more traditional methods, e.g., compression molding. Since, geometrically, all samples were similar, we conclude that the printing process alters the microstructure of the weld.

We used a combination of experimental polarization modulated infrared microspectroscopy measurements and continuum modelling to show that a significant degree of molecular anisotropy is frozen into the sample upon solidification for high-molar-mass samples (Figure 5.7a), whereas low-molar-mass samples exhibited isotropy. The model suggests that this residual anisotropy is localized near to the surface of a deposited filament, as seen in the previous work, resulting in a partially entangled weld region that reduces interlayer strength. This prediction is in qualitative agreement with the experimental measurements of the weld strength.

Achieving molecular isotropy in the weld is clearly an interplay between molecular weight and temperature. However, whilst print temperature is commonly implemented as a control parameter, varying the molecular weight of the feedstock is often overlooked and may be more effective, as demonstrated in this work. Thus, we propose that molecular weight should be considered as a key control parameter in the MatEx process; provided that $Z_{eq} > 6$, lowering the molecular weight of the feedstock will achieve stronger builds due to isotropy in the weld.

5.8 Appendix

Figure 5.10 shows the weld strength as a function of different printing conditions for (a) PLA_4_160k, (b) PLA_12_180k and (c) PLA_0_190k.

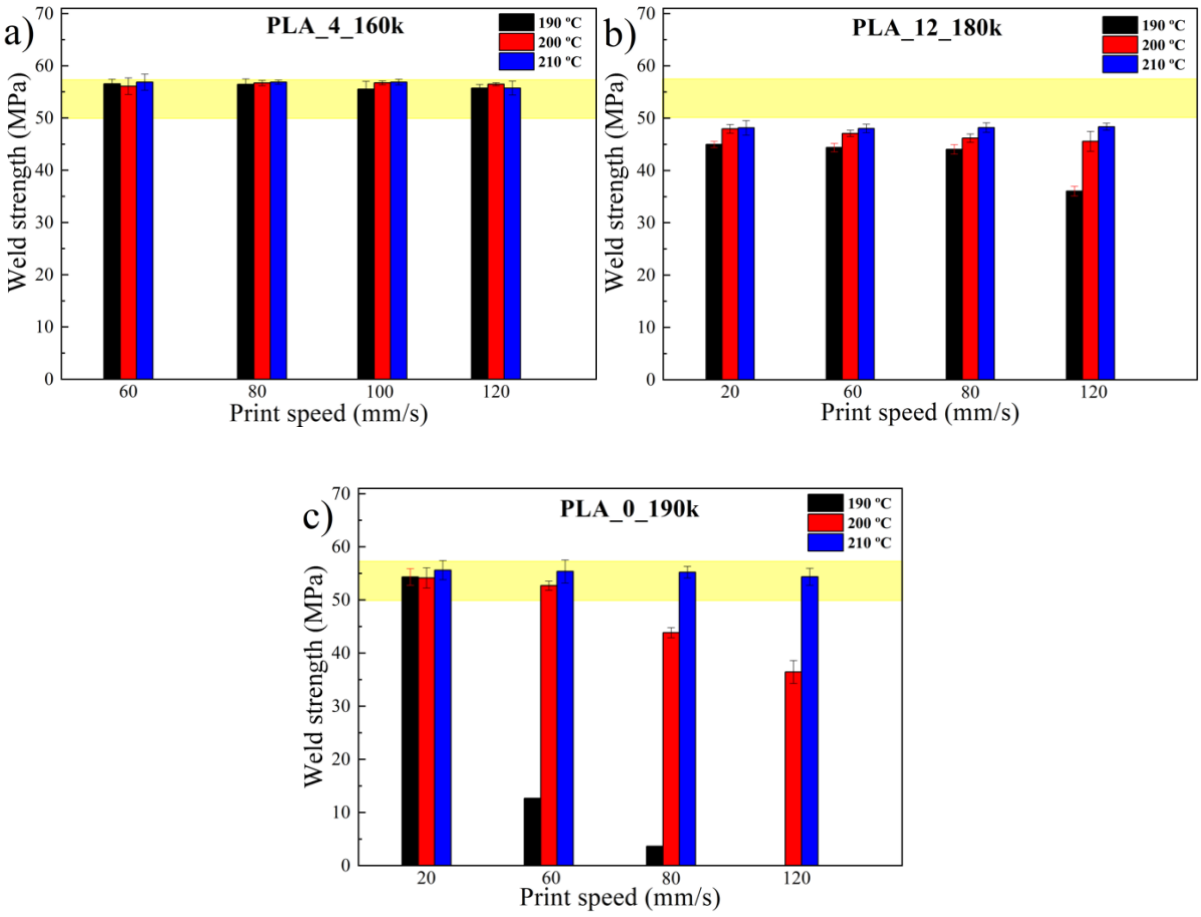

Figure 5.10. Weld strength as a function of different printing conditions for (a) PLA_4_160k, (b) PLA_12_180k and (c) PLA_0_190k.

6 EFFECT OF CHAIN RIGIDITY ON WELD STRENGTH

6.1 Introduction

Since chain stiffness guarantees a high glass transition temperature and consequently a greater mechanical performance at high temperature, this chapter aims to study the effect of chain stiffness on the interlayer weld quality. In particular, we investigate for the first time how the change in the chain chemistry for two commercial co-polyesters may affect the molecular inter-diffusive welding process inherent to Fused Deposition Modeling technique. Although this change in chemistry modifies the temperature-dependent rheological behavior in ways that are expected to be detrimental to the weld strength, by employing an established continuum polymer modeling approach we propose that increasing the polymer chain stiffness is fundamental to ensuring that residual molecular anisotropy in the weld region is limited, and thus weld strength is maintained.

6.2 Calorimetric analysis

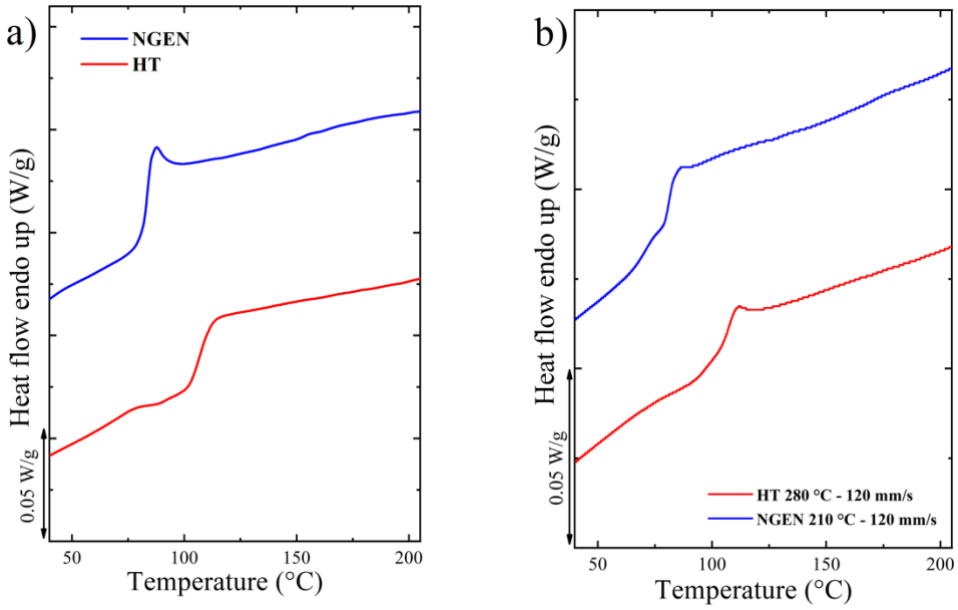

Figure 6.1. (a) Second heating ramps at 10 °C/min for the two materials obtained by DSC calorimetric analysis; (b) Heating ramp at 10 °C/min at DSC for two materials samples after printing.

Since both copolyesters (see Chapter 3.1) are hygroscopic, both filaments were kept drying at 55 °C for 4 h before proceeding with the printing of the samples. Thermal characterizations obtained by differential scanning calorimetry (DSC) analysis is reported in Figure 6.1 and reveals that both samples are completely amorphous both before and after printing.

6.3 Rheological characterization

Figure 6.2 shows the G', G'' master curves for the two materials at reference temperature 230 °C (a) and the corresponding shift factors (b) used to obtain the master curve via time-temperature superposition. The shift factors are fitted according to the Williams-Landel-Ferry (WLF) equation (Equation 4.5).

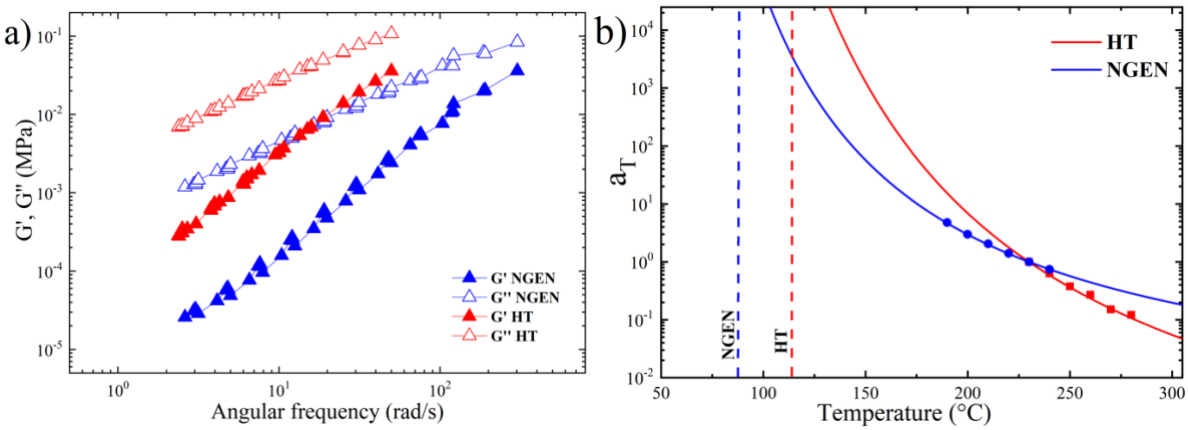

Figure 6.2. (a) Master curves for NGEN and HT obtained at the reference temperatures of 230 °C and (b) rheological shift factors as a function of temperature. The vertical dashed lines in graph b correspond to the glass transition temperatures of the two materials as measured by DSC.

Figure 6.2a demonstrates distinct differences in the rheology of the two materials, with the HT master curve shifted to higher frequencies compared to the NGEN. Since the molecular weights of the two materials are similar, this indicates that HT polymers have longer rheological time scales than NGEN; specifically, a longer polymer reptation time, which governs the inter-diffusive welding process that we are interested in here. For both materials a variation in the slope of the G 'curves is evident as the frequency decreases. This is probably an indication of a degradation of the two polymers.[230] Furthermore, for both co-polyesters, we were not able to observe the crossover frequency between the two moduli, which is therefore located at higher angular frequencies.

To interpret the rheology master curve and extract the material parameters required for our molecularly-aware model, we employ the Likhtman-McLeish model for entangled polymer melts[211] using RepTate software.[212] Although this analysis should be used with caution for short molecules, the method yields an entanglement molecular weight of $M_e = 8\,000$ g/mol for both materials, in line with other model predictions for polyesters.[231,232] In terms of classical tube theory, this gives $Z = 2$ for the number of entanglements in the melt and corresponding entanglement time scales $\tau_e(T = T_r) = \tau_e^0 = 1 \times 10^{-3}$s and 5×10^{-3}s, for NGEN and HT, respectively. The polymer reptation time is related to this entanglement time via

$$\tau_d(\mathrm{T} = \mathrm{T_r}) = \tau_\mathrm{d}^0 \approx 3\tau_e^0 Z^3 \qquad (6.1)$$

and the temperature-dependence of the reptation time is obtained by applying the WLF equation:

$$\tau_d(T) = \tau_d^0 a(T) \qquad (6.2)$$

Thus, for both materials, the reptation time diverges at the respective glass transition temperature, as determined by the WLF equation (Figure 6.2b). Physically, this means that interdiffusion is arrested at Tg and the material can be considered solid. Compared to NGEN, the HT WLF equation diverges more rapidly near the glass transition and the reptation time of the HT polymer is increased by a factor of 5. These factors will have a considerable effect on the weld time available during 3D printing, as well as the amount of interdiffusion χ that occurs.

6.4 Weld time characterization

Only the time-temperature superposition behavior of the polymer is required to calculate the available weld time. The weld time is given by

$$t_{weld} = \int_0^\infty \frac{1}{a\big(T(t)\big)}\,dt \qquad (6.3)$$

where $a(T)$ is given by the WLF equation, as in previous literature.[206]

Since temperature is time-dependent in the material extrusion process, it is essential to measure the temperature evolution to calculate the weld time.

Figure 6.3 shows two thermal profiles for NGEN at the same nozzle temperature (230 °C) and different printing speeds (20 and 80 mm/s). Each temperature peak corresponds to a passage of the nozzle at the region of the plate where the thermocouple is fixed. It can be seen how, as the printing speed increases, the number of peaks in the same time interval increases proportionally. It can also be noted that the temperature recorded at the end of each decay never goes below the one set for the build plate (85 °C). The successive maxima in the profile are found at decreasing temperature, due to the insulating effect of the deposited layers. The acquisition of the thermal profiles proceeds until the complete deposition of three layers for each analyzed condition.

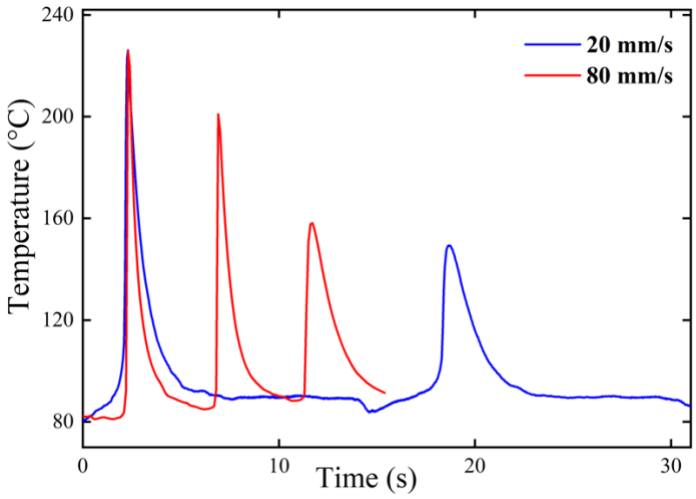

Figure 6.3. Thermal profiles of the first layer of NGEN deposited on the build plate at the nozzle temperature of 230 °C and indicated printing speeds.

Since welding occurs predominantly during the first pass of the nozzle, we assume that subsequent heating/cooling cycles have a negligible effect on welding; thus, we restrict our thermal measurement to the first decay in temperature following the first peak. As required by our molecularly-aware model, we convert the discrete temperature measurements to a continuous function, by fitting the data to the following exponential decay:

$$T(t) = T_{env} + (T_0 - T_{env}) * \exp\left(\frac{-(t - t_0)}{\tau_c}\right) \qquad (6.4)$$

where T_{env} is the environment temperature, T_0 is the average between nozzle temperature and bed temperature, t_0 is the time corresponding to the start of cooling while τ_c is the cooling time scale. Equation 6.4 is then substituted into Equation 6.3 for the weld time, which is solved numerically using Wolfram Mathematica to determine the time interval from the beginning of the temperature decay until the glass transition temperature is reached – or equivalently the available "weld time" during the first cooling cycle. Figure 6.4 shows an example of this weld time calculation in the case of a HT co-polyester sample printed at a nozzle temperature 250 °C and 20 mm/s of printing speed. The calculation was performed for all the printing conditions explored for the two materials.

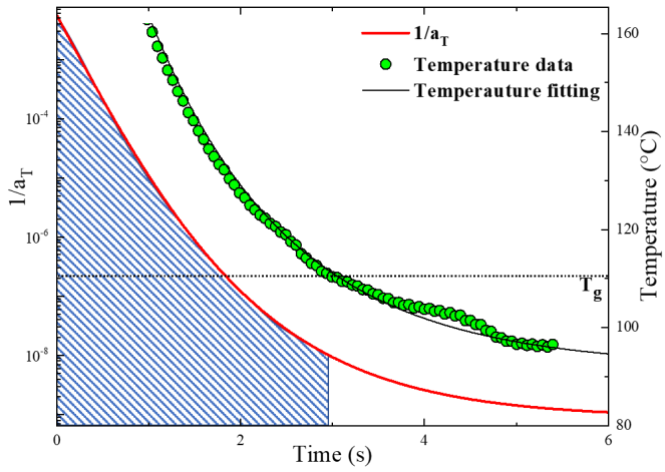

Figure 6.4. Weld time function and temperature as a function of time for the first cooling segment for a HT sample printed at 250 °C and at 20 mm/s. The weld time is calculated as the integral with respect to the time, corresponding to the highlighted area under the $1/a_t$ red curve.

Figure 6.5 shows the weld time values obtained for all the considered printing conditions.

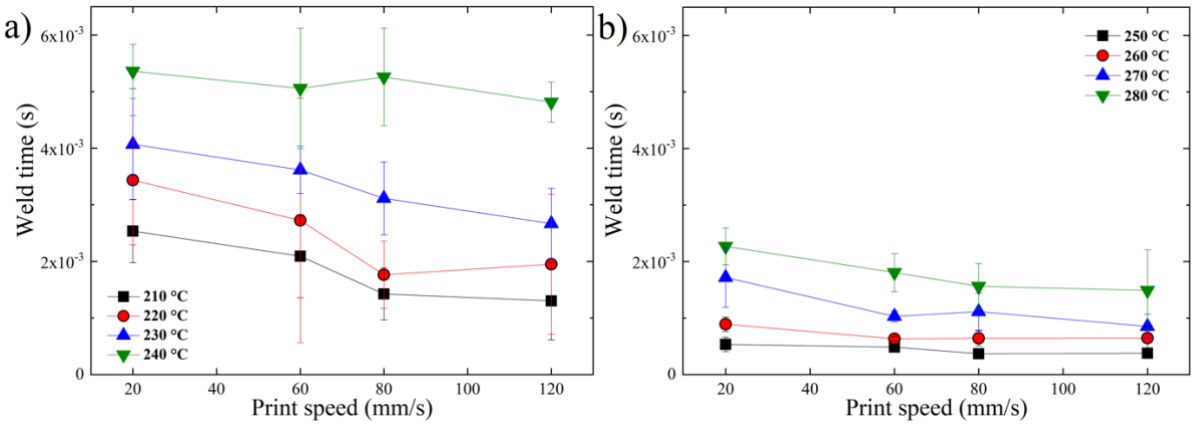

Figure 6.5. Calculated weld time as a function of print speed at different nozzle temperatures for (a) NGEN and (b) HT.

For both materials, the weld time increases using a higher nozzle temperature, in agreement with previous literature results.[139] By printing at higher temperatures, in fact, the polymer remains above the glass transition temperature, where the rheological relaxation times are faster, for a longer time interval, thus increasing the degree of interdiffusion. The increase in speed leads to a slight decrease in the weld time. Moreover, the range of weld times for the respective processing conditions are significantly lower for the HT co-polyester than for NGEN. This reduced weld time, together with a much slower reptation time, suggests more efficient welding for NGEN. Thus, we would expect to observe dramatic differences in the weld strength achieved for each of the materials.

6.5 Weld strength measurements

Figure 6.6a illustrates the failure of a printed specimen. We see that the fracture occurs completely along the weld line in a brittle manner, thus this mechanical test is considered a representative measurement of weld strength. For conditions where the weld strength becomes comparable to the bulk strength, failure along the weld lines is seldomly observed. Furthermore, it is necessary to measure the thickness of the adhesion surface between the adjacent layers, to correctly evaluate the stress experienced by the sample. Figure 6.6b shows an example of a micrograph for a sample of NGEN obtained using a stereoscope. To compare the weld strength to the bulk strength of the material, compression molded samples were also prepared and tested. Compression molding has been carried out at 235 and 250 °C for NGEN and HT, respectively. The high temperature has been kept for 5 min under an applied pressure of ca. 3.5 tons; the applied temperatures are suitable to obtain a good flowability of the amorphous polymer particles. We find that the molding conditions result in homogeneous samples, which do not show any apparent defects or weld lines. A representative example of the stress strain curves obtained for compression molded specimen are shown in Figure 6.7a. The behavior is that typical of thermoplastic polymers, with a linear elastic region, a yield point, strain softening, cold drawing and very low strain hardening. Since the stress at break is typically lower than the stress at yield, we choose the maximum stress to represent the bulk strength of the material, as indicated in Figure 6.7a. Figure 6.7b shows some examples of stress/strain curves for different HT 3D-printed samples compared to the compression molded sample (black line). For 3D printed samples, which fail in a brittle manner, the maximum stress (stress at break) is taken as a measure of weld strength and compared to the maximum stress

(stress at yield) of the compression molded sample, which corresponds to the bulk strength of the material. This example shows how the process conditions can affect the tensile strength and the elongation break, and ultimately how the weld strength is reduced compared to the bulk strength.

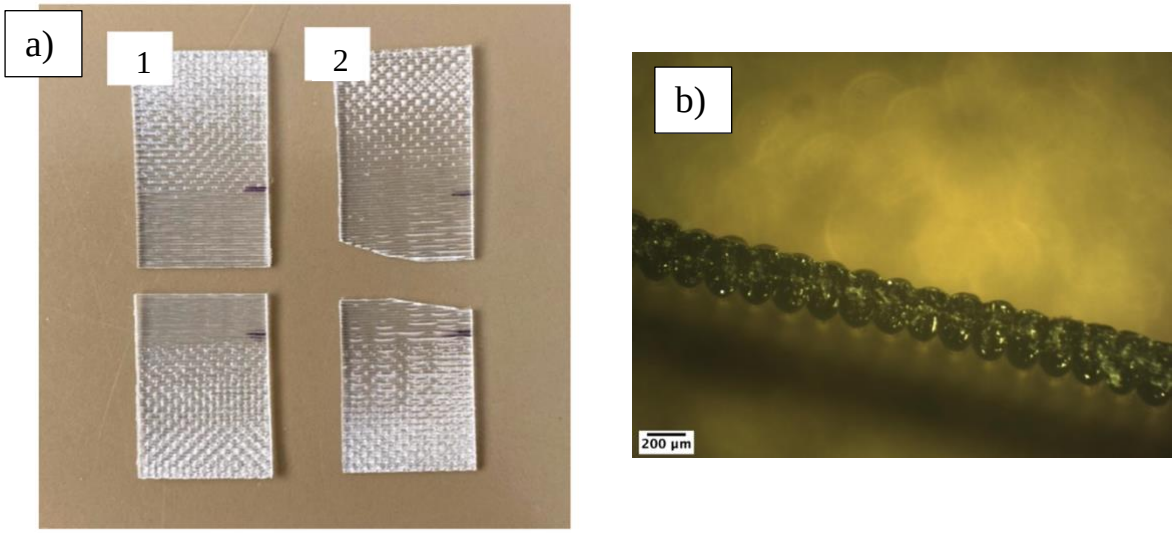

Figure 6.6. NGEN copolyester specimens after failure for samples printed at 210 ◦C and 80 mm/s (a.1) and 240 °C and 20 mm/s (a.2) respectively. (b) An example of micrograph of the deposited layers for a sample printed at 260 ◦C and at a speed of 20 mm/s.

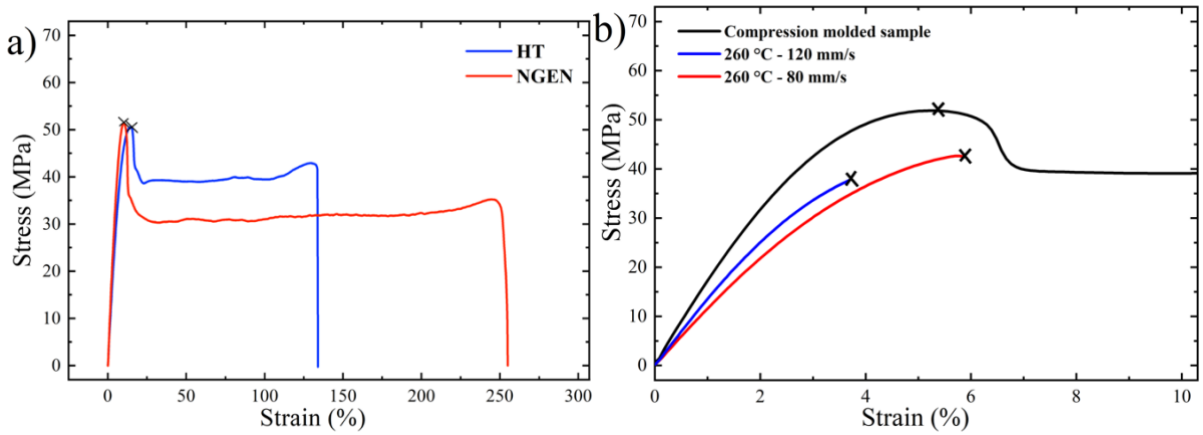

Figure 6.7. (a) Stress-strain curves for NGEN and HT copolyester samples obtained by compression molding. The cross indicates representative value of bulk strength for each material. (b) Examples of stress/strain curves obtained from tensile tests on both compression molded and 3D-printed HT samples, with cross indicating the bulk strength and weld strength, respectively.

Figure 6.8 shows the weld strength values for different nozzle temperatures for NGEN (a) and HT (b), as the printing speed varies. The shaded yellow areas correspond to the bulk strength values measured using dog-bone shaped specimens obtained by compression molding. As it can be seen, for most of the printing conditions the strength perpendicular to the print direction remain lower than the reference values, which are about 50 and 52 MPa for NGEN and HT, respectively.

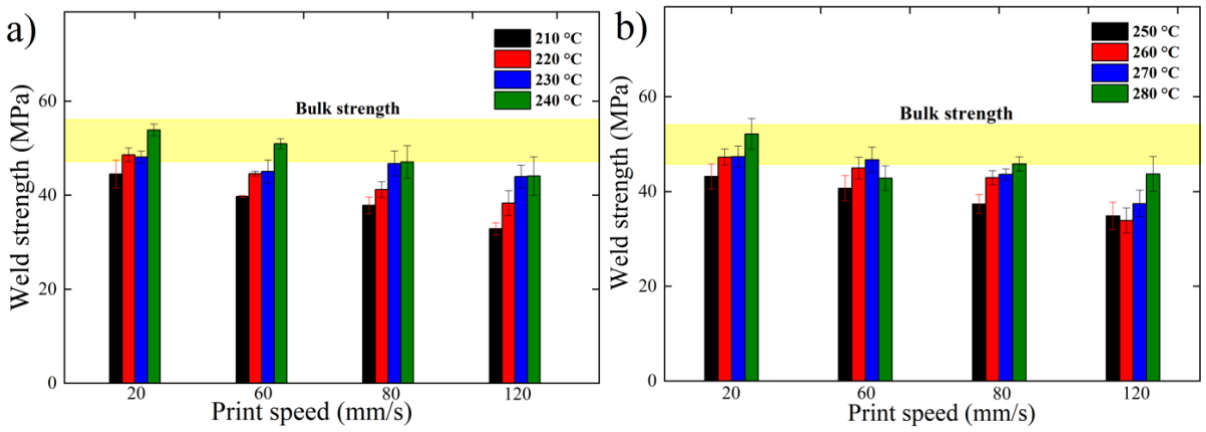

Figure 6.8. Trend of the weld strength as a function of the different printing conditions for NGEN (a) and HT (b). The shaded yellow area correspond to the bulk strength measured on compression molded samples.

For both materials, the weld strength decreases as the printing speed increases, with a less marked decrease at higher nozzle temperatures. Despite the difference in weld time and reptation time between the two materials, the weld strength values are very similar to each other. In this respect, Figure 6.9 shows the weld strength normalized with respect to the value of compression molded specimen as a function of weld time for all the considered printed conditions for the two materials. For both co-polyesters, the bond strength between the layers increases as the weld time increases, with a slightly steeper slope for the HT co-polyester. It can also be noted that, despite the lower weld times for HT, the reduction of weld strength is comparable to that of NGEN, which has weld times almost three times larger.

Although for both materials the behavior of the weld strength as a function of the weld time is clearly linear in the semi-logarithmic plot, there is some scatter in the data particularly for the strongest printing conditions, i.e., at high deposition speed and low extrusion temperature. The reason for this discrepancy could be attributable to the presence of molecular orientation at the interfaces between the layers, generated due to the characteristics of the deposition process.

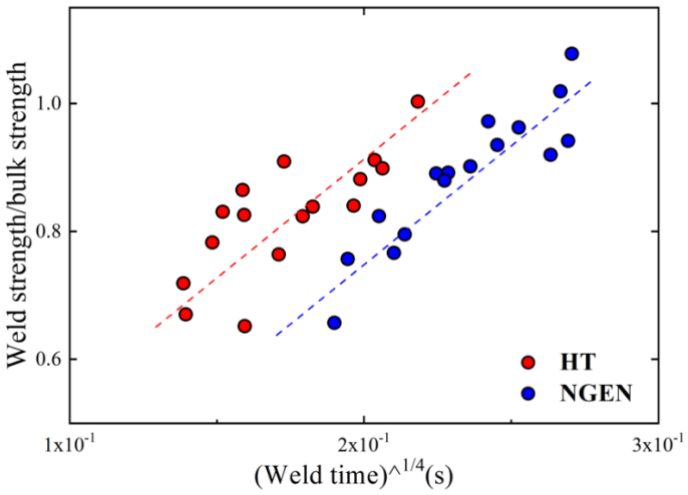

Figure 6.9. Weld strength as a function of the weld time for NGEN and HT for all analyzed printing conditions. Dashed lines serve to guide the eyes.

6.6 Molecularly-aware modelling

Compared to NGEN, we have shown that the HT polymer reptation time is increased (by a factor of 5). Furthermore, the temperature-dependence of the reptation time diverges more rapidly in the vicinity of the glass transition, as determined by the WLF equation, which leads to a decrease in the weld time. Due to these factors, we expect to observe a decrease in weld strength because of reduced interdiffusion and more residual alignment trapped in the vicinity of the weld (see Chapters 4 and 5). However, we have shown that the weld strength of HT is in fact comparable to NGEN (Figure 6.8).

To investigate this counter-intuitive behaviour, we employ the established molecularly-aware modelling approach of McIlroy et al.[3,4,152] We refer the reader to references [3,4] for full details of the model and comment here only on the constitutive model. This model relies on the Rolie-Poly constitutive model[206] for which the polymer behaviour is described using a configuration tensor, A, satisfying the Rolie-Poly equation:

$$\frac{dA}{dt} = K \cdot A + (A \cdot K)^T + \frac{1}{\tau_d(T)}(A - I) + \frac{f}{\tau_R(T)}\left(2 - \frac{1}{\Lambda}\right)\left(A + \frac{\beta}{\Lambda}(A - I)\right) \qquad (6.5)$$

The velocity gradient tensor is denoted K, which captures the printing flow. Importantly, in cylindrical polar coordinates the A_{rs} component of the configuration tensor describes how the polymer is aligned with respect to the flow direction, s, and Λ (defined in Equation 4.11) describes the degree of polymer stretch; $A = I$ indicates a polymer at equilibrium. The polymer reptation time, τ_d, governs interdiffusion and polymer orientation, whereas the polymer Rouse time, τ_R, governs polymer stretch. Both relaxation times depend on the temperature profile. The convective constraint release parameter is set to $\beta = 0.5$ and f denotes a finite-extensibility parameter to be discussed.

This constitutive model is employed to predict how the polymer molecules deform when subjected to steady-state flow through a heated axisymmetric printing nozzle, followed by deposition into an elliptically shaped filament onto a build plate. This flow-induced deformation then provides an initial condition to calculate how the polymers diffuse and relax as the deposited filament cools in the surrounding air. In the model, cooling is dictated by the measured thermal profile, which is employed as an axisymmetric boundary condition to solve the heat equation. Once the glass transition temperature is reached, diffusion and relaxation of the polymer is arrested, and we obtain the molecular properties of the filament at solidification. We infer that the properties at the filament surface correspond to properties within the weld region of an assembled single-filament wall. Here we probe the following weld properties:

- the degree of interdiffusion, in relation to the polymer's radius of gyration,
- the degree of residual alignment,
- the degree of residual stretch.

Notably, these weld properties are dominated by the polymer relaxation time, τ_e^0, the entanglement number, Z, and the cooling time scale, τ_c. Recall that whilst we model NGEN and HT having the same Z, the relaxation and cooling time scales of the two materials are very different.

Owing to a larger weld time and shorter reptation time, NGEN demonstrates a greater degree of interdiffusion than HT across all print conditions, as shown in Figure . Moreover, despite the more severe WLF curve as discussed in Chapter 6.2 there remains sufficient weld time for the HT polymers to diffuse a distance that is greater than or equal to their size. As is a recurring theme across different printing materials, we must probe the polymer configuration in the weld

region rather than the degree of interdiffusion (which suggests full healing), to better understand molecular contributions that may be responsible for reduced weld strength.

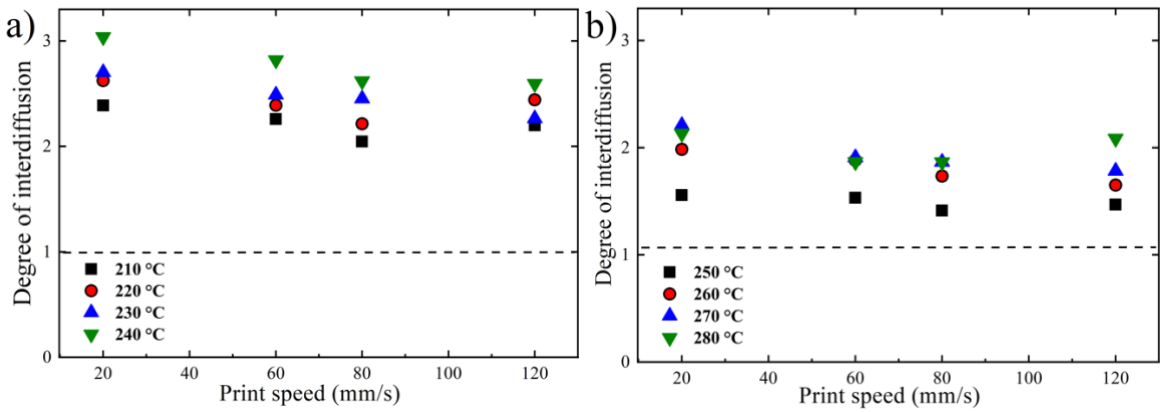

Figure 6.10. Degree of interdiffusion calculated at different temperatures as a function of the print speed for (a) NGEN and (b) HT.

Since we wish to quantitatively compare the molecular stretch and orientation of two co-polymer materials comprised of several monomers, we must account for the effect of finite extension of the polymer chain (previous studies of simpler homopolymers assumed infinite extensibility). Here we incorporate a finite-extensibility factor into our Rolie-poly equation defined by a typical Langevin function[233]

$$f = \frac{(3 - \Lambda^2/\Lambda_{max}^2)(1 - 1/\Lambda_{max}^2)}{(1 - \Lambda^2/\Lambda_{max}^2)(3 - 1/\Lambda_{max}^2)} \qquad (6.6)$$

The finite extensibility limit, Λ_{max}, is defined by Bartolai et al.[234]

$$\Lambda_{max}^2 = \frac{M_e}{C_\infty M_0} \qquad (6.7)$$

for characteristic ratio C_∞ and M_0 the average molecular weight of a repeat polymer unit; $C_\infty = 1$ corresponds to a freely jointed chain. Thus, to proceed we must consider the chemistry of our two co-polyester materials.

Recall that Figure 3.1 illustrates the structure of the monomers present in a repeat unit of NGEN and HT. Table 6.1 indicates the average molecular weight of a repeat unit in each co-polyester (considering for the sake of simplicity an equimolar composition of all comonomers). Since

NGEN contains monomers that all have rotational freedom, we assume that the characteristic ratio is similar to that of the most commonly occurring polyester PET ($C_\infty = 4$).[235] On the other hand, the TMCD monomer present in HT is much stiffer due to a non-planar carbon ring (see Figure 3.1). In fact, the increased heat resistance and toughness demonstrated by HT (compared to NGEN) is attributed to this monomer. Since M_0 is very similar for the two materials, a change in stiffness comes from the characteristic ratio; here, we assume that the characteristic ratio of HT is larger by a factor of two. By Equation 6.7 this gives slightly different finite extensibility limits of $\Lambda_{max} = 3$ for NGEN and $\Lambda_{max} = 2$ for HT.

Table 6.1. Model parameters to predict extensibility of copolyester chains

Material	**NGEN**	**HT**
M_e	8 000 g/mol	8 000 g/mol
Average M_0	233.24 g/mol	274.31 g/mol
C_∞	4	8
Λ_{max}	~3	~2

Figures 6.11 and 6.12 show the predicted degree of residual molecular alignment and stretch in the weld region upon solidification for NGEN and HT, respectively. As observed for other polymer melts used in MatEx, residual alignment increases with increasing print speed and reduced print temperature. This is due to a greater initial flow-induced polymer orientation, which relaxes more slowly due to an increased polymer reptation time resulting from the thermal profile. Note that faster printing speeds yield faster cooling rates. The residual stretch shows similar trends since the two control parameters - print speed and print temperature - have similar effects on the initial stretch and the Rouse relaxation time.

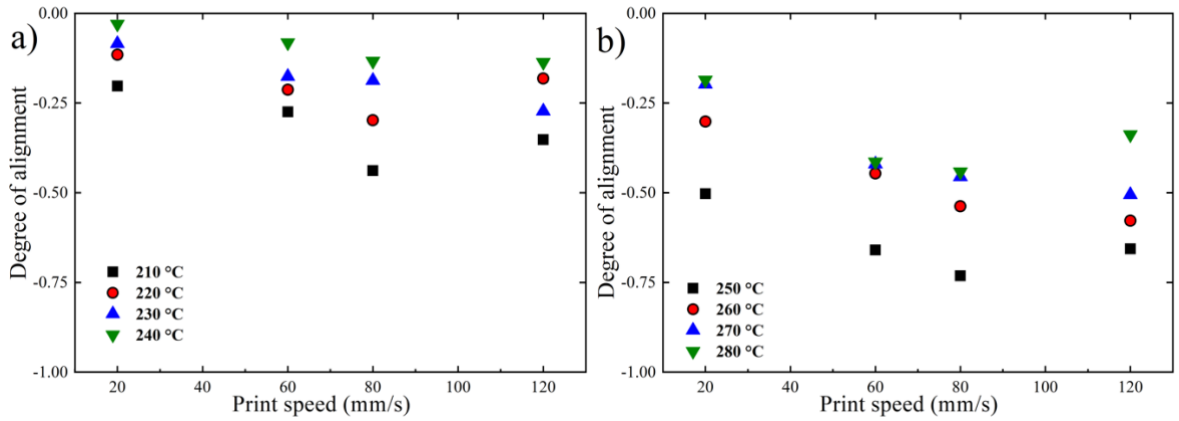

Figure 6.11. Degree of alignment calculated at different temperatures as a function of the print speed for (a) NGEN and (b) HT.

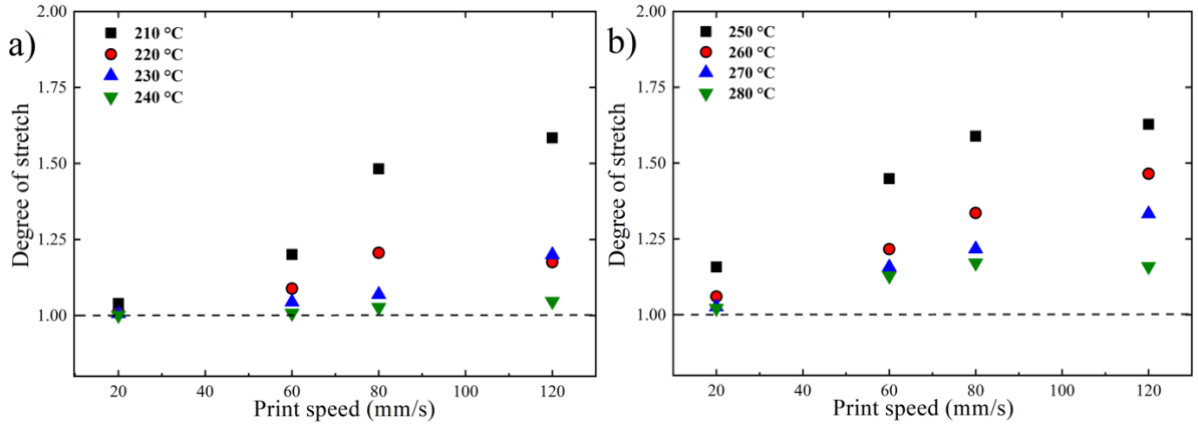

Figure 6.12. Degree of stretch calculated at different temperatures as a function of the print speed for (a) NGEN and (b) HT.

Nonetheless, both materials exhibit quantitatively similar molecular properties in the weld region. Thus, we expect a comparable mechanical response for NGEN and HT as we have seen in our weld strength investigation. Importantly, we have shown that despite having an increased reptation time and reduced weld time, which should exacerbate molecular features known to reduce weld strength, it is the increased stiffness of the HT monomer TCMD that reduces the extensibility of the polymer chains, and therefore limits the ultimate degree of stretch and alignment found in the weld. For model predictions neglecting the effect of chain extensibility, we refer the reader to Figures 6.15 and 6.16 in the Appendix. Here we compare NGEN and HT for f = 1 i.e., assuming that the chains of both materials are infinitely extensible. Importantly, the rheology of the chains differs, with HT demonstrating a longer reptation time. Without the limit of finite extension, this ultimately leads to a greater degree of deformation (stretch and alignment) of the HT polymers compared to the NGEN polymers under similar printing conditions. Introducing a finite extensibility limit to represent stiffness of the chain has little effect on the NGEN polymer dynamics, but significantly restricts the deformation in HT polymers. Hence, the degree of deformation that persists at solidification becomes comparable, as shown in Figures 6.11 and 6.12. Whilst the benefits of the TCMD monomer are known in terms of the bulk properties of the co-polyester, for the first time we confirm that this chemistry does not negatively affect the welding behaviour during MatEx (in comparison to the NGEN feedstock).

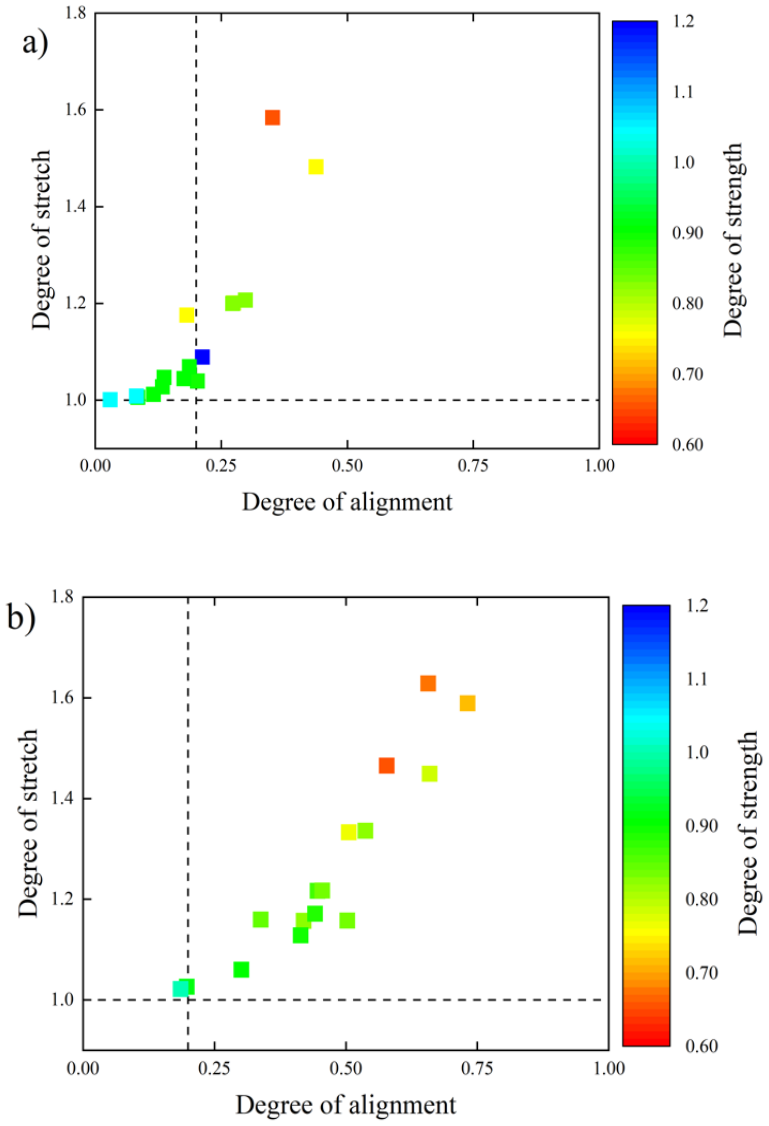

Figure 6.13. Degree of residual alignment and degree of strength as a function of degree of alignment for NGEN (a) and HT (b).

In Figure 6.13 we plot the degree of residual alignment versus the degree of residual stretch. Whilst the relationship between these model parameters is inherent to the Rolie-Poly model, colour-coding the points correspond to the reduction in the experimentally measured weld strength and reveals subtle correlations between the molecular and mechanical properties in the weld. As discussed earlier, the quantitative reduction in weld strength is similar for the two materials across all printing conditions.

However, by applying our molecular perspective, we reveal two qualitative regimes that may be overlooked in the experimental data:

I. Weld strength is moderately affected (G_{weld}/G_{bulk} ~ 90%, green-blue points) due to the persistence of *polymer alignment* in the weld

II. Weld strength is affected more severely (G_{weld}/G_{bulk} ~ 60%, orange-red points) due polymers being both *aligned and stretched* in the weld region.

The polymer configuration for regimes I and II is shown schematically in Figure 6.14:

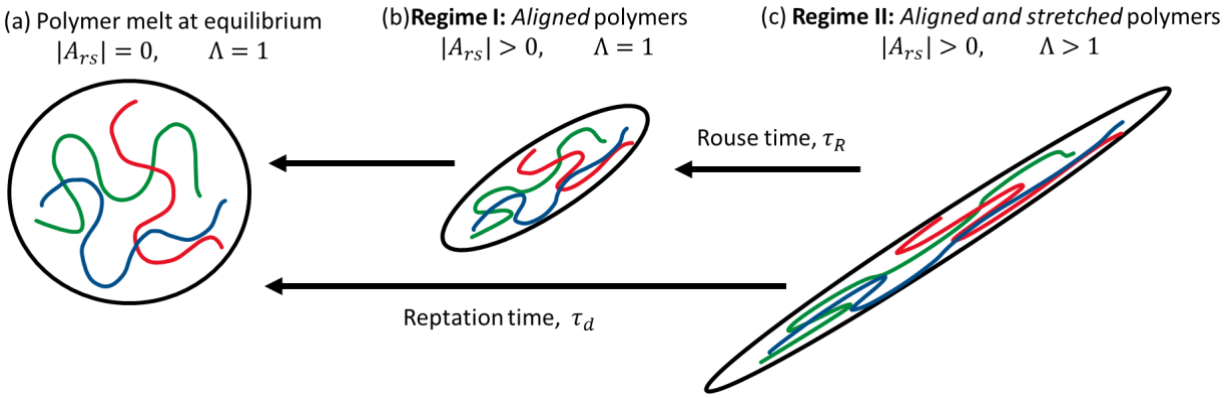

Figure 6.14. Schematization of the polymer configuration for regimes I and II purposed in the model.

Figure 6.13 shows that NGEN spans both regime I and II: at high print temperatures and slow printing speeds, there is sufficient time for polymer stretch to fully relax prior to solidification, while polymer alignment persists (since $\tau_d > \tau_R$). As can be seen in Figure 6.10a, this regime results in a moderate decrease in weld strength, which appears to plateau with increasing print speed. Under more severe conditions – at low print temperatures and fast printing speeds – stretch relaxation is also prohibited by the glass transition. We propose that this second regime leads to a more dramatic reduction in the weld strength (as seen in Figure 6.10b). On the other hand, HT appears to be predominantly affected by regime II. This is due to a combination of increased relaxation time, reduced weld time and stiffer chains.

Thus, using our molecularly-aware modelling approach we have shown that whilst the reduction in weld strength may be quantitatively similar for different materials, there lies subtle and intricate differences in the molecular features within the weld region that are reflected in the weld strength measurements. These observations allude to some of the difficulties in deriving a theoretical model to predict mechanical properties based on the molecular features.

6.7 Conclusions

In this chapter, we investigated the behaviour of two grades of polyester, namely NGEN and HT, with 3D printing capability. Due to a new comonomer which increases the glass transition of the material by ~20 °C, HT demonstrates superior temperature-resistance properties.

Whilst improvement in the bulk properties is known, here we investigate for the first time how this change in chemistry may affect the molecular inter-diffusive welding process inherent to the layer-by-layer MatEx technique. Through rheological characterization and in-situ temperature measurements, we show that HT exhibits longer polymer relaxation times and decreased weld times, compared to NGEN. Although these properties are expected to significantly reduce the weld strength, our mechanical analysis finds that this is not the case; NGEN and HT demonstrate comparable mechanical properties.

To understand this counter-intuitive behaviour, we employ an established molecularly-aware modelling approach to predict the degree of interdiffusion achieved at solidification, as well as any residual anisotropy that may be trapped in the weld region. Due to the nature of these co-polyester materials, for the first time we incorporate finite-extensibility into our modelling approach. We show that all printing conditions permit interdiffusion of the order of the polymer size in both materials, despite the increased reptation time and reduced weld time of HT compared to NGEN. Furthermore, we show that both materials demonstrate similar molecular properties (residual polymer stretch and alignment) within the weld region. We propose that it is the increased stiffness (and therefore reduced extensibility) of the HT polymers that mitigatees residual anisotropy and therefore any effect increased anisotropy may have on weld strength, in agreement with our weld strength properties.

6.8 Appendix

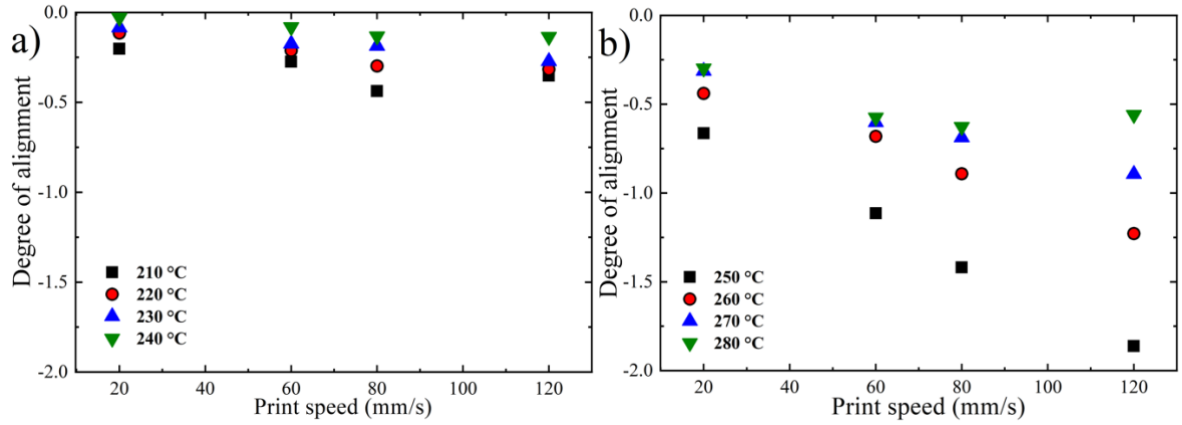

Figure 6.15. Degree of alignment calculated at different temperatures as a function of the print speed for (a) NGEN and (b) HT in the case of infinite extensibility (f=1).

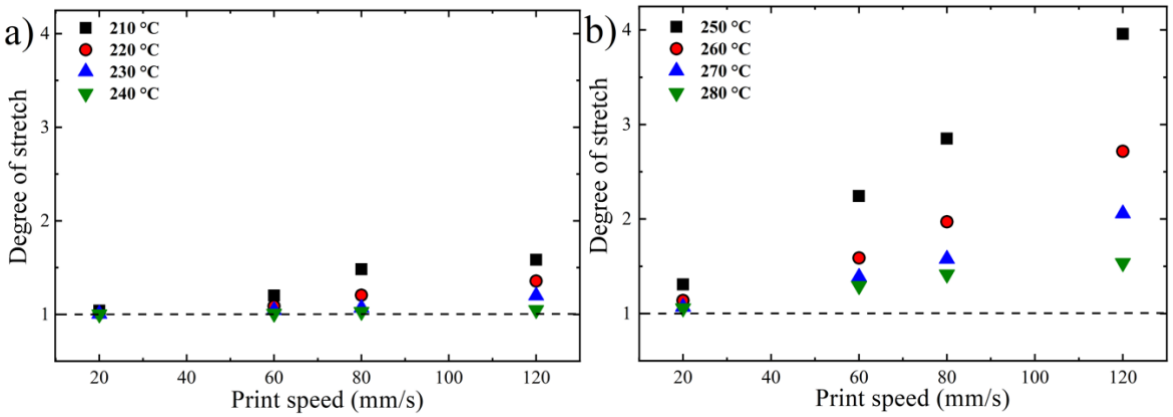

Figure 6.16. Degree of stretch calculated at different temperatures as a function of the print speed for (a) NGEN and (b) HT in the case of infinite extensibility (f =1).

In Figure 6.15 is shown the model predictions for the degree of residual alignment and stretch in the weld region for NGEN and HT in the case of infinite extensibility. This corresponds to $\Lambda_{max} \rightarrow \infty$ and thus taking $f = 1$ in the Rolie-Poly constitutive equation (Equation 6.5). With unlimited extension we find that the molecular properties in the weld region predicted for NGEN and HT are quantitatively different; the longer relaxation times and faster cooling rates in HT lead to greater molecular anisotropy (stretch and alignment) being trapped in the weld region at solidification. In this case, and in line with the results presented in Chapter 4, we would expect HT to exhibit a significantly weaker weld compared to NGEN. This in contrast to the results plotted in Figures 6.8 and 6.9 that account for the stiffness of the chains via the

extensibility parameter; finite Λ_{max}, as calculated from the chemical composition of a repeat unit, leads to quantitatively similar weld properties for both NGEN and HT in agreement with of our weld strength measurements.

7 EFFECT OF CRYSTALLIZATION ON WELD STRENGTH

7.1 Introduction

In this work it was proposed to study the crystallization kinetics of two different polyamides used for FDM 3D printing and to link it to the microstructure and properties obtained during 3D printing. The kinetics is studied both in isothermal and fast cooling conditions, thanks to a home-built device which allows to mimick the quenching experienced during filament deposition. Despite the degree of crystallinity is not a strong function of printing variables, the weld strength of adjacent layers shows remarkable variations. Moreover, a decrease of its value with printing speed is observed, linked to the probable development of molecular anisotropy under the more extreme printing conditions.

7.2 Isothermal Characterization

As can be observed from the standard calorimetric analysis (Figure 7.1a-b), these are two semi-crystalline polymers which differ both in crystallization temperature and degree of crystallinity (melting enthalpy). In particular, Novamid ID1030, being a copolymer of PA-6 and PA-6,6 (see Chapter 3.1) presents a lower crystallization temperature and a lower crystallinity, while the melting point is close to that of Novamid ID1070 (PA-6).

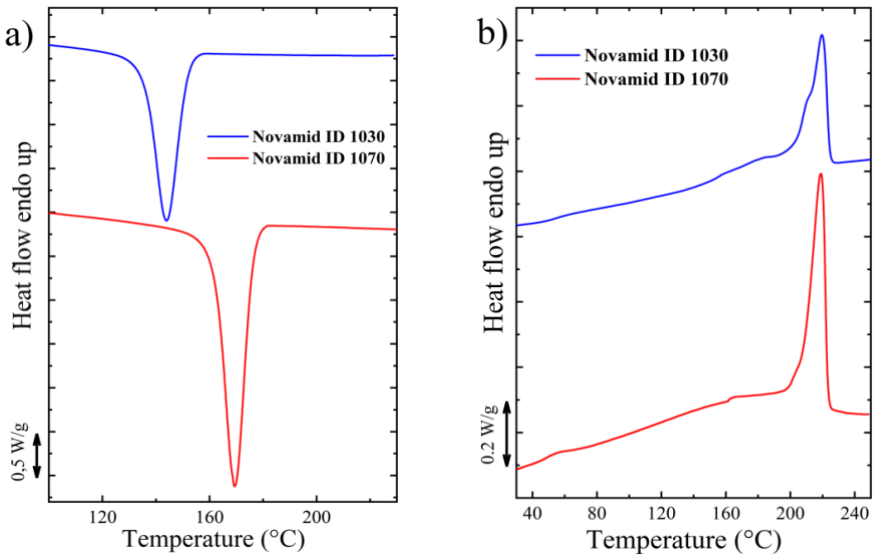

Figure 7.1. (a) Cooling ramp and (b) second heating ramp at 10 °C/min for the two polyamides obtained by DSC calorimetric analysis.

A characterization of the materials' isothermal crystallization behavior has been performed according to the Avrami model.[236] Avrami's equation allows to describe, at constant temperature, the changes in the degree of space filling by the spherulites and is particularly useful in the context of polymeric materials to obtain important information relating to their crystallization kinetics. Once the onset points corresponding to the start of crystallization in a standard heating-cooling cycle were individuated, a series of isotherms at gradually increasing temperatures was performed on the two polyamides, starting from about 15 °C above the temperature of crystallization onset. Some of the isothermal crystallization curves for the two materials are shown in Figure 7.2.

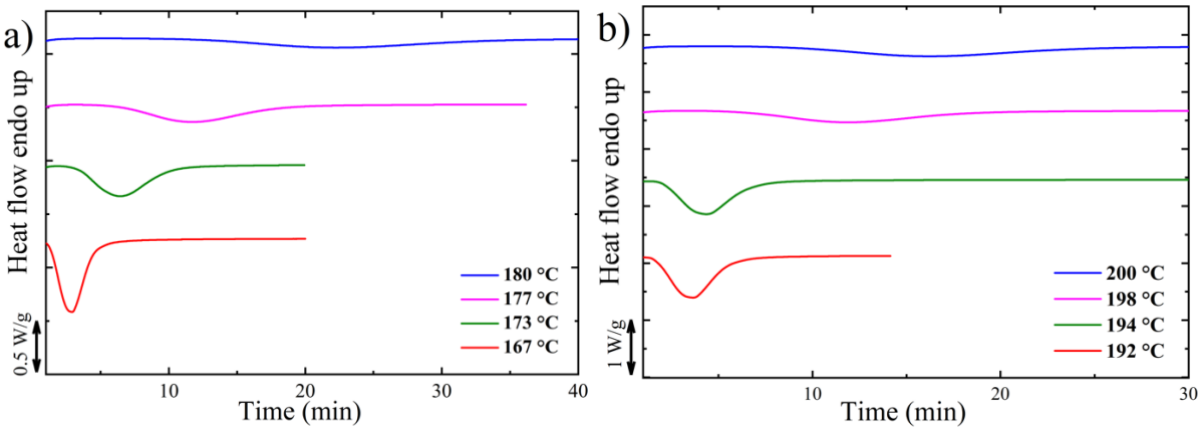

Figure 7.2. Examples of isothermal crystallization curves for (a) Novamid ID 1030 and (b) Novamid ID 1070.

By means of a plug-in for the OriginPro software, it was possible to analyze the isothermal crystallization curves in order to obtain the half-crystallization times ($t_{0.5}$) for the two materials.[236] The obtained values are reported in Figure 7.3a. As expected, in the case of the homopolymer, a shift to higher temperatures is required to achieve the same crystallization rate of the copolymer, indicating a largely different crystallization kinetics for the two polyamides. The difference in the undercooling at the same rate for the two materials are in the order of 20 °C. Thanks to the same plug-in it was also possible to calculate the Avrami index for the two materials, reported in Figure 7.3b. An Avrami exponent of about 3 is obtained, suggesting classical spherulitic crystallization on heterogeneous nuclei.

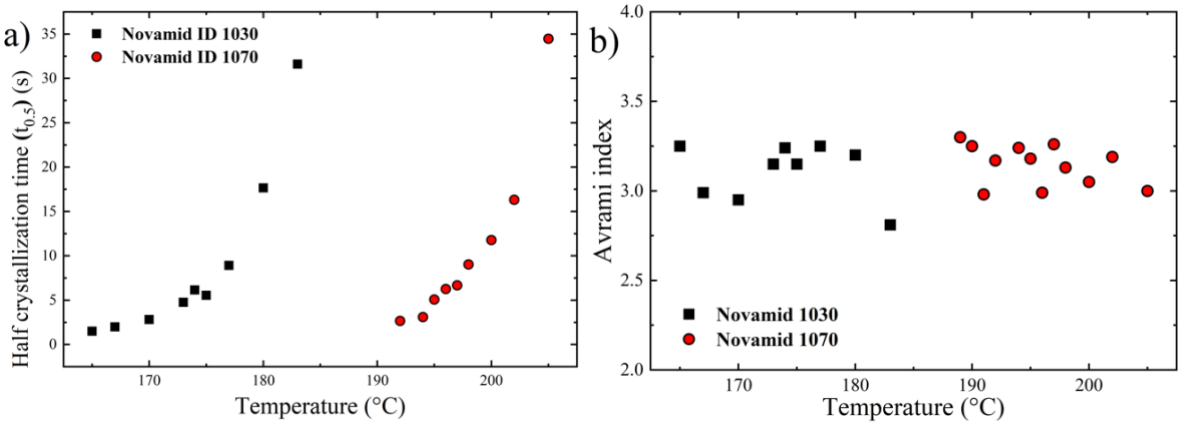

Figure 7.3. (a) Half crystallization time for the two polyamides and (b) Avrami index of the two polyamides as a function of the crystallization temperature.

7.3 Non-Isothermal Characterization

The characterization of the crystallization kinetics in fast cooling conditions was carried out using a custom-built quenching device[189] which applies a controlled air flow, thanks to which it was possible to obtain cooling rates of increasing intensity. Samples for the two materials were prepared in the form of thin films, heated above their respective melting temperatures and subsequently cooled. The thermal history of the samples was measured using a type K thermocouple inserted into the thin film and connected to a National Instrument acquisition unit. Figure 7.4a shows as example the cooling curves for the Novamid ID 1030 for different air flows, while Figure 3b shows the corresponding cooling rates obtained by numerical derivation of the temperature profiles. It can be seen that the temperature decreases exponentially to the target value (room temperature), and that the decrease is somehow perturbed at the lower cooling rate by the heat released by crystallization, which provokes a temperature plateau. Cooling rates are linearly dependent on temperature when no phase transition occurs. As such, the crystallization process can be detected at the lowest cooling rate as a peak in the derivative curve (Figure 7.4b). We note that cooling rates of few to tens °C/s are obtained, exceeding those commonly achievable by DSC, but in the range of those expected for FDM 3D printing.[129] Some of the quenched samples were subsequently subjected to a heating ramp at 10 °C/min at the DSC in order to highlight possible differences of crystallinity with cooling conditions.

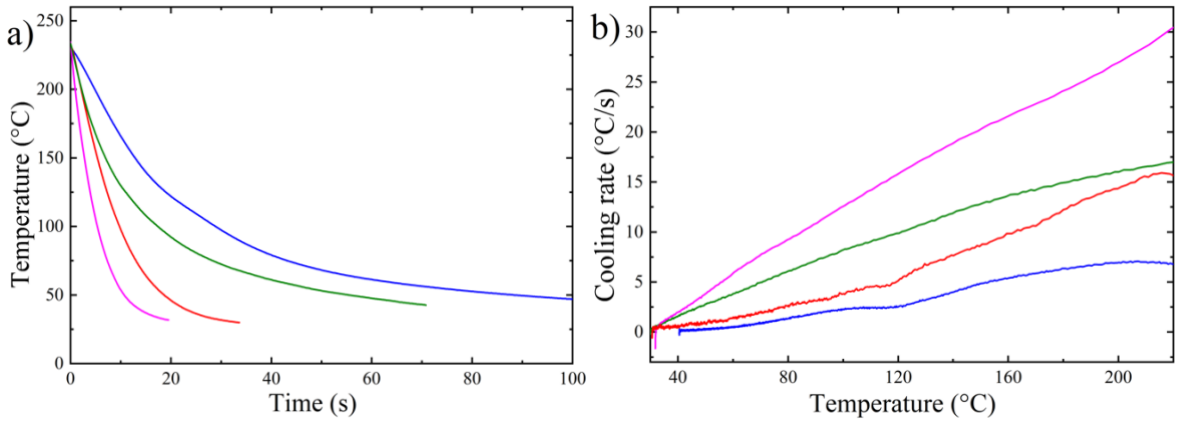

Figure 7.4. (a) Cooling curves obtained for different air flows and (b) corresponding cooling rates for Novamid ID 1030 samples.

For both the polyamides, Figure 7.5 shows that, as the cooling rate increases, the area of the cold crystallization peak increases, correlated to the heat released during the crystallization process in the heating ramp. This means that, with faster cooling, the material will have a gradually lower initial degree of crystallinity before the DSC heating ramp. The enthalpy of crystallization during the fast cooling can thus be derived by subtracting the cold crystallization enthalpy from the melting endotherm. Therefore, the initial degree of crystallinity shows a decrease as a function of the cooling rate for both polyamides as displayed in Figure 7.5. The crystallinity decreases of about one third with an increase of cooling rate from few to hundreds °C/s. In fact, at high cooling rates, the time allowed for the polymer chains during solidification to arrange into ordered structures is shorter, thus preventing the material from reaching the maximum achievable degree of crystallinity. Furthermore, Figure 7.5 shows that, at the same cooling rate, the homopolymer has a lower extent of cold crystallization than the copolymer, thus indicating a lower degree of initial crystallinity of the latter. The crystallization kinetics of polyamide 6,6 in non-isothermal conditions had already been studied by Rhoades et al., who found a similar trend to the present case.[237]

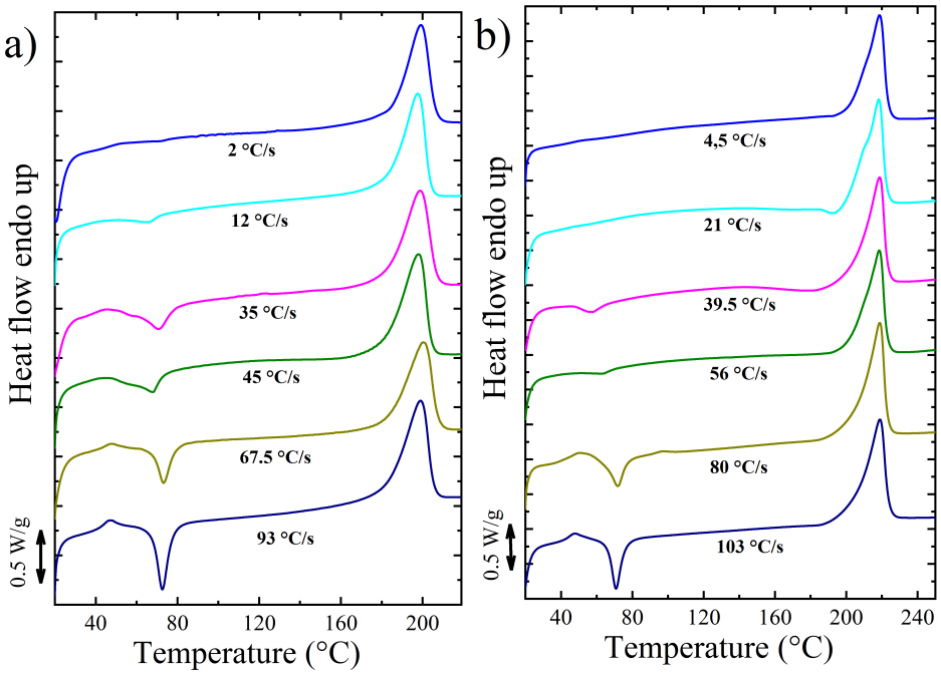

Figure 7.5. (a) DSC heating ramps obtained for samples subjected to the indicated different cooling rates for Novamid 1030 (b) and Novamid 1070. Cooling rates are estimated at 180 °C.

The large difference in crystallizability of the two materials, as evidenced by isothermal and non-isothermal measurements, might result in different welding performance during printing. In principle, the polyamide copolymer crystallizes at lower temperature during cooling which give rise to longer welding times and potentially more efficient weld formation. However, the different nozzle temperatures for the two polymers complicate the above reasoning. On the other hand, the different crystallinity between homo- and copolymer can influence the ultimate achievable tensile strength, even if a similar bond between the layers is achieved during cooling the deposited filaments.

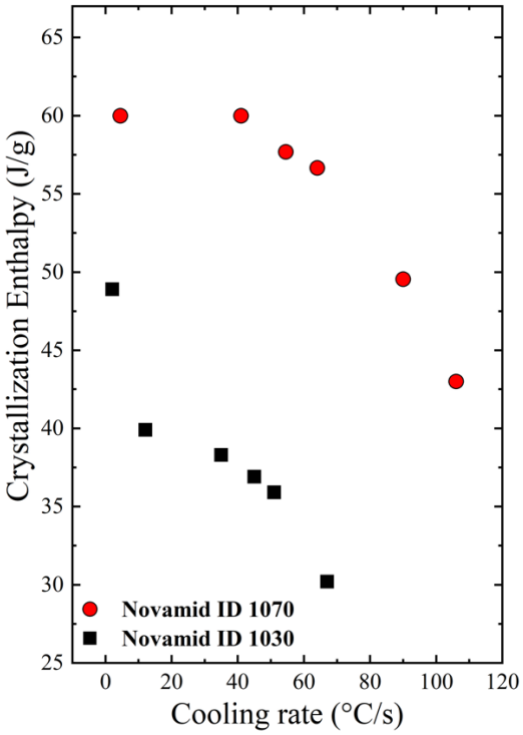

Figure 7.6. Crystallization enthalpy for samples of the two polyamides as the cooling rate estimated at 180°C varies.

7.4 In-situ Temperature measurements

Having characterized the crystallization behavior of the materials under isothermal and non-isothermal processing conditions, the work focused on determining the thermal history of the material during the deposition process. Several previous works have already proposed set-ups able to measure the thermal profile of the material during the deposition process, for example by IR thermography or small thermocouples.[121,132] The printed geometry is the same as previously described (see Chapter 3.2) and which was also used for the weld strength measurements described further on. Using a micro-thermocouple placed on the printing plate in correspondence with the deposition area, it was possible to measure the thermal profile of the first layer following its deposition and that of the subsequent layers above it. Figure 7.7 shows the thermal profile for Novamid ID 1030 at different printing speed and at different nozzle temperatures respectively. Note that the maximum temperature measured by the thermocouple does not correspond to that set in the nozzle, probably due to the very short contact time between the two. Each temperature peak corresponds to a passage of the nozzle over the area of the plate where the thermocouple has been placed. The printing process was allowed to proceed until the deposition of successive upper layers led to temperature peaks of appreciable intensity. For both polyamides the thermal profile was measured at three printing

speeds (20, 60, and 120 mm/s) and for three different nozzle temperatures for the two materials (220, 230, and 240 °C for the Novamid ID 1030 and 255, 265, and 270 °C for the Novamid ID 1070). Figure 7.7 shows some examples of thermal history for Novamid ID 1030 respectively at constant deposition temperature (a) and constant deposition rate (b). It can be seen how different nozzle temperatures lead to an evident variation of the maximum amplitude, while different printing speeds lead to variation of the modulation period of the temperature/time curves. It can also be observed that the minimum temperature reached after subsequent depositions increases, reasonably due to the increasing number of underlying hot layers deposited which therefore slow down the dissipation of heat during cooling. Moreover, it is worth to note that the average temperature in the long time keeps definitely higher than the glass transition. As such, crystallization is expected to proceed until saturation, given the recorded temperature history of the deposited filament.

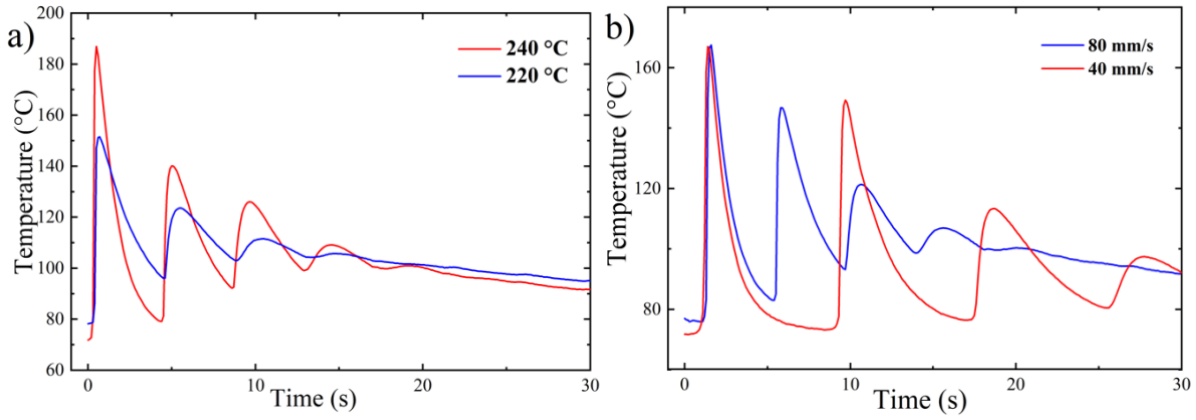

Figure 7.7. Thermal profiles of the first layer of Novamid ID 1030 deposited on the plate for different printing conditions at the same deposition speed (80 mm/s) (a) and the same nozzle temperature (230 °C) (b).

To characterize the thermal history corresponding to the different printing conditions the peak relative to the first passage of the nozzle on the thermocouple was considered, representing the deposition of the first layer. By analyzing the cooling curves in the different cases and obtaining the respective cooling rates, it is possible to estimate a parameter (beta), which represents the reciprocal of the time constant for the exponential cooling of the single filament.[154] The beta parameter (β) was calculated for all the analyzed printing conditions and the results in the case of Novamid ID 1070 are shown in Figure 7.8a. The trend of parameter ß found for the various process conditions highlights the fact that the deposition speed does not meaningfully influence it. In fact, the average β value remains constant as the printing speed increases but changes, shifting to higher values, with increasing the nozzle temperature. The samples for which

thermal history was measured were subsequently subjected to a heating ramp at 10 °C/min in the DSC. Figure 7.8b shows the heat flow related to the heating ramps for the Novamid ID 1070 samples printed at 20, 60, and 120 mm/s at the nozzle temperature of 230 °C. The heat flow curves indicate, for all printing conditions, the achievement of the maximum degree of crystallinity during cooling, as judged by the absence of cold crystallization. In fact, by comparing the values of β for the printed sample with those obtained for quenched samples, it is possible to derive that a β of around 1.2 s^{-1} correspond to a cooling rate, calculated at 180 °C, of about 100 °C/s (Figure 7.9). Such high cooling rates, as previously seen, should have led to the appearance of cold crystallization peaks during subsequent heating. However, this does not happen because, as shown by the thermal history of the layer during printing, the polymers remain above the glass transition temperature (about 60 °C) for most of the deposition process, thus giving the possibility to the material to fully crystallize. Therefore, in the range of cooling rates corresponding to the printing conditions, the enthalpy of crystallization corresponds to the maximum achievable by the material. The achievement of the maximum degree of crystallinity in all the cases may also be due to the effect induced by the flow to which the materials are subjected during the deposition process, which can accelerate the crystallization kinetics. Being able to cool in relatively mild conditions during the printing process, the materials do not exhibit the characteristic peak of cold crystallization when subjected to a subsequent heating ramp. A noteworthy exception is that of the sample printed at 20 mm/s which shows a distinct exothermic signal before melting, possibly indicating a reorganization phenomenon of the crystals. For that sample the width of the melting endotherm is also broader than the rest of the conditions, suggesting that a different microstructure might be present. Similar cold-ordering event are observed for samples of polyamide-6 crystallized at large undercooling into a mesomorphic structure.[238]

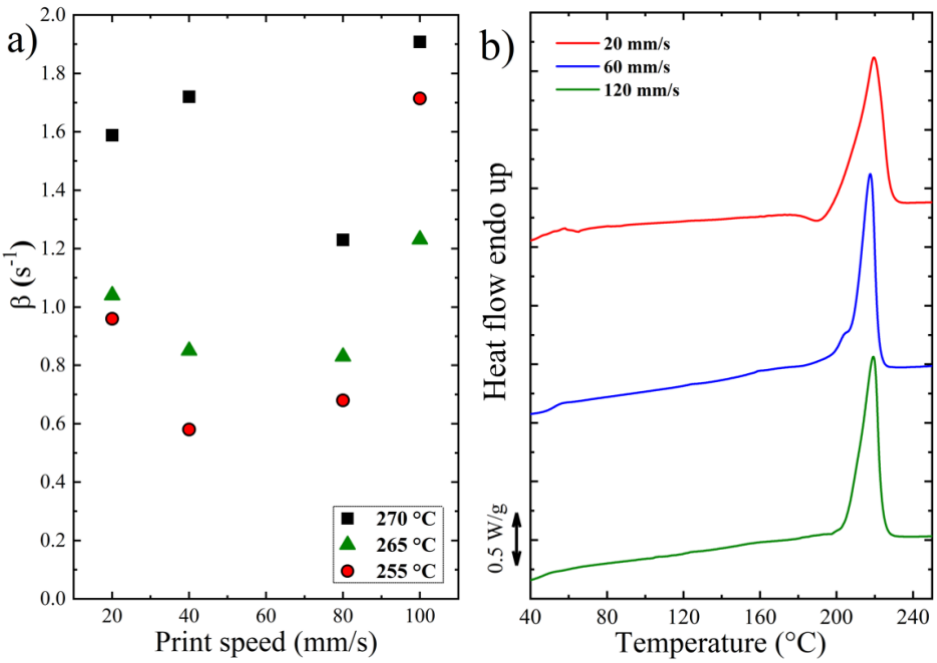

Figure 7.8. (a) Average values of parameter β calculated for the different printing conditions and (b) DSC ramps in heating at 10 °C/min for samples of Novamid ID 1070 printed at 255 °C.

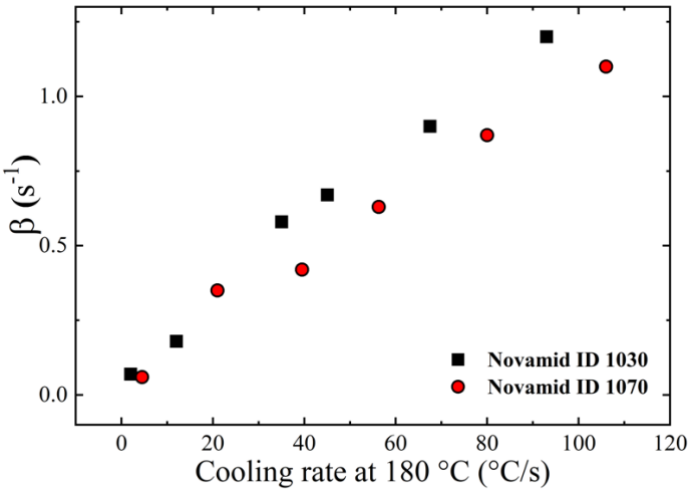

Figure 7.9. Parameter β estimated for the two polyamides as a function of the cooling rate calculated at 180 °C.

7.5 Weld Strength Measurements

Next, results on the adhesion strength between adjacent layers and how this vary with processing conditions are presented. As already demonstrated, the processing parameters can be a fundamental factor in determining a better adhesion between adjacent layers,[239] sometimes allowing the use of the products even in extreme temperature conditions.[240] Table 7.1

summarizes the ranges of variation of the printing conditions, for which the mechanical properties were analyzed.

Table 7.1. Adopted processing parameters.

Parameter	Novamid ID 1030	Novamid ID 1070
Nozzle temperature	220–240 °C	255–270 °C
Print speed	20–120 mm/S	20–120 mm/s
Build plate temperature	80 °C	80 °C
Chamber temperature	50 °C	50 °C

All samples were printed maintaining the buildplate and printer chamber temperatures at 80 °C and 50 °C, respectively. After printing the cubes and cutting out the faces from which the specimens for mechanical tests were obtained, in order to correctly assess the stress, it was necessary to measure the contact surface between adjacent layers using a stereoscope. An example photomicrograph of the weld width measurement is shown in Figure 7.10a. Tensile tests were carried out by setting a clamp separation speed of 6 mm/min. Some examples of the stress–strain curves obtained for Novamid ID 1030 are shown in Figure 7.10b. In the proposed examples, it is generally noted that the tensile strength and deformation at break are lower the more extreme the printing conditions of the materials are, i.e., when one is far from the typical processing temperature of the material and at a deposition rate too high or low. These stress–strain curves show how the printing conditions strongly influence the final mechanical properties, in particular the stress at break, and how this value is different when the load is applied perpendicular or parallel to the printing direction (Figure 7.10b). For both materials, the trend can be traced back to a brittle breakage, therefore preceding the yielding phase, apart from the case indicated as “parallel to the printing direction”, in which yielding and therefore plastic deformation occurs. The large difference between loading in the parallel or transverse direction indicate a meaningful anisotropy of the printed object.

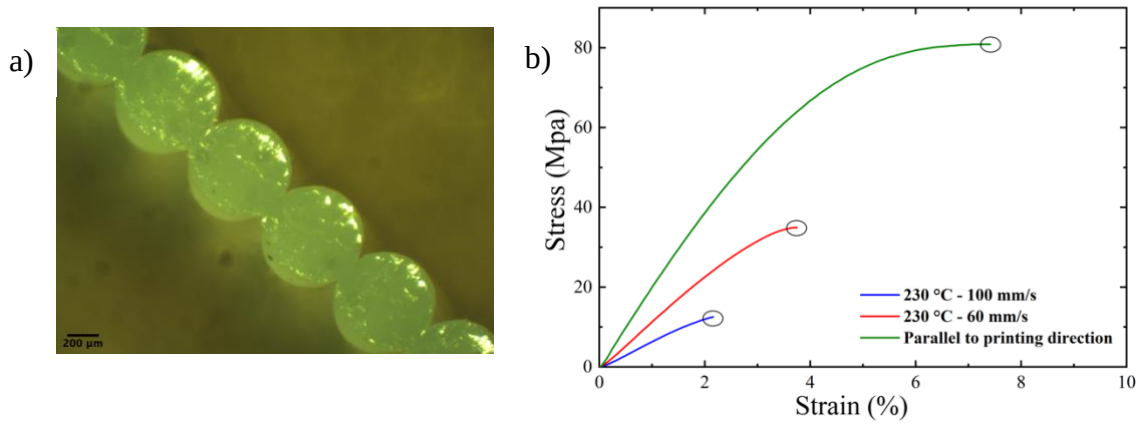

Figure 7.10. a) An example of micrograph of the deposited layers for a sample printed at 230 °C and at a speed of 60 mm/s; b) examples of stress–strain curves obtained from tensile tests on Novamid ID 1030 samples.

Figure 7.11show the weld strength values for different nozzle temperatures for Novamid ID 1030 (a) and Novamid ID 1070 (b), as the printing speed varies. The horizontal lines in the graphs correspond to the average yield stress values obtained for the two materials in the case of measurements parallel to the printing direction. All measured values, remain lower than those of bulk stress at break, respectively found at 79 and 89 MPa. It should be noted that, in the case of the Novamid ID 1030, there are no data points related to some printing parameters, because of the impossibility in printing the specimen under those conditions. In the case of the copolymer the change in weld strength recalls the behavior already found in amorphous polymers, i.e., the weld strength decreases monotonically with increasing printing speed. In particular, for high printing speeds the drop in weld strength can be associated with the molecular orientation, due to the high flow experienced by the macromolecules (Figure 7.11a).[241] If subjected to high shear stresses it is in fact possible to orient the polymer chains in a preferential direction of space. The result of this mechanism is the generation of an anisotropic molecular network, resulting in a decreased density of entanglements in a direction perpendicular to the printing one. In fact, a decreasing trend of weld strength with increasing printing speed had already been found in Chapter 4 and 5, where an amorphous material was used and the presence of molecular orientation at the interfaces between the layers was demonstrated by birefringence and polarized infrared microspectroscopy measurements. A similar trend for random polyamide copolymers was also found by Vaes et al.[242] measuring the tear energy, and also for other semi-crystalline polymers such as PP[243,244] and PA[106,172,245].

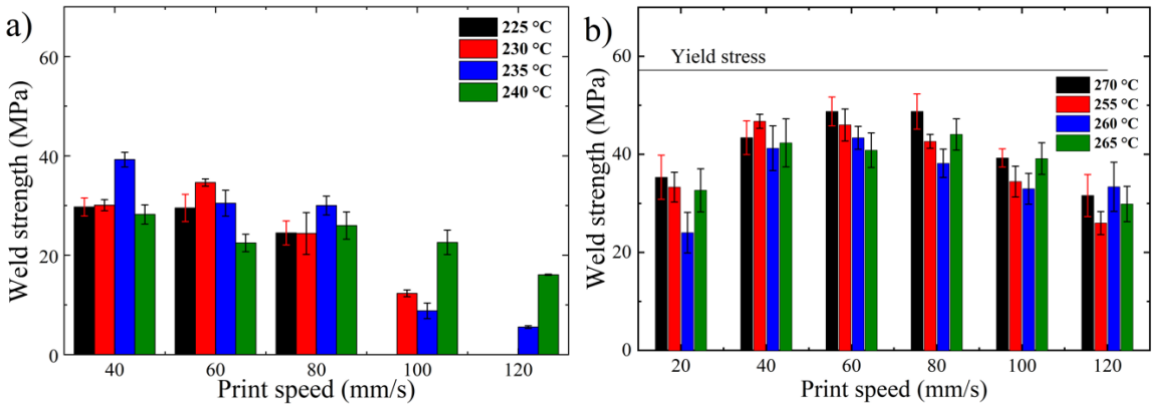

Figure 7.11. Trend of the weld strength as a function of the different printing conditions for Novamid ID 1030 (a) and Novamid ID 1070 (b). The horizontal line in figure (b) corresponds to the average yield stress values obtained for the two materials in the case of measurements parallel to the printing direction.

The situation is different in the case of the homopolymer, where the data trend displays a maximum, with the optimum located at intermediate printing speeds with respect to the analyzed range. It is interesting to note that an optimum value of tensile strength as a function of printing parameters is also achieved in multiple-layer structures, due to a balance between deposition of the filament and bond formation.[246] The poor mechanical properties at the interface for low deposition rates could be due to the peculiarity of the deposition process. We recall in fact that the final DSC heating scan of the Novamid 1070 sample printed at 20 mm/s presents reorganization and broad melting phenomena, indicative of less stable crystals, possibly pertaining to the mesophase.[237,247] We thus propose that the original crystals for the sample printed at 20 mm/s are in mesophase and possess lower mechanical strength. For what concerns the effect of temperature, previous work on amorphous PLA showed that there was a shift to greater values of weld strength as the temperature of the nozzle increases.[156] Instead, for the two polymers considered in this study this process variable does not seem to play a fundamental role for crystallization and final mechanical properties of the printed specimen. This suggest that the welding quality is not limited by the diffusion for this system, being the nozzle temperature always sufficiently high to allow formation of entanglement formation at the interface, unless orientation start to be a dominant factor. In general, the homopolymer Novamid ID 1070 is more resistant to traction than the copolymer Novamid ID 1030.

7.6 Appendix

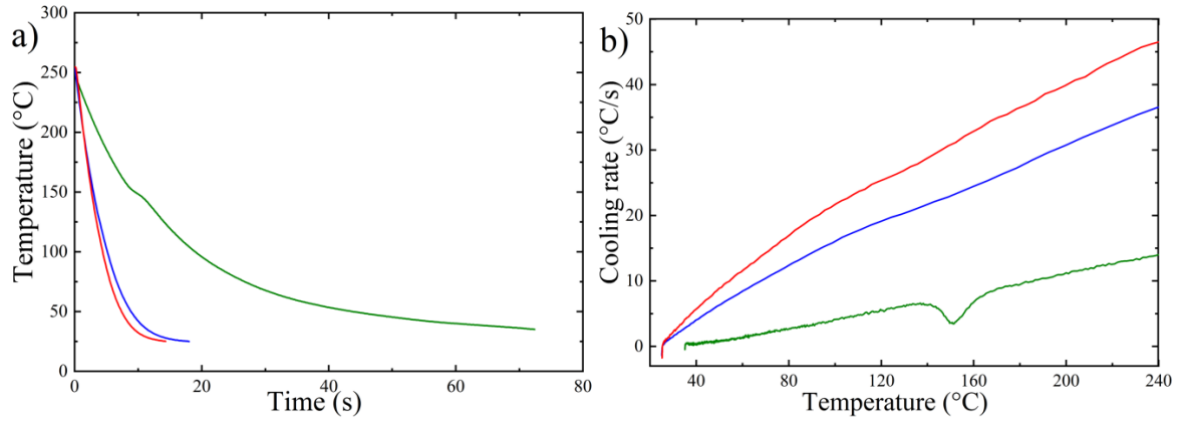

Figure 7.12. (a) Cooling curves obtained at different air flows and (b) corresponding cooling rates for Novamid ID 1070 samples.

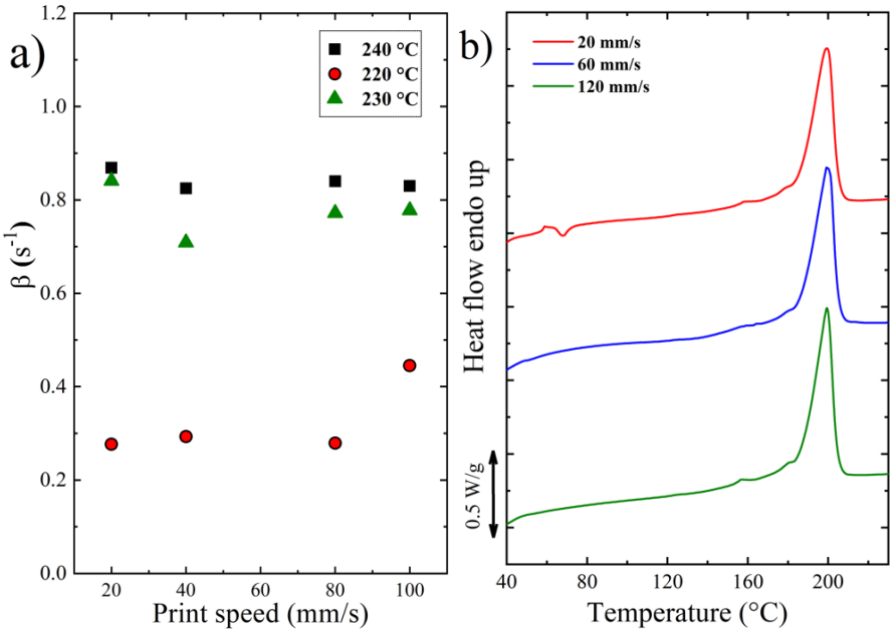

Figure 7.13. (a) Average values of parameter β calculated for the different printing conditions for Novamid ID 1030 samples. (b) DSC ramps in heating at 10 °C/min for samples of Novamid ID 1030 printed at 230 °C.

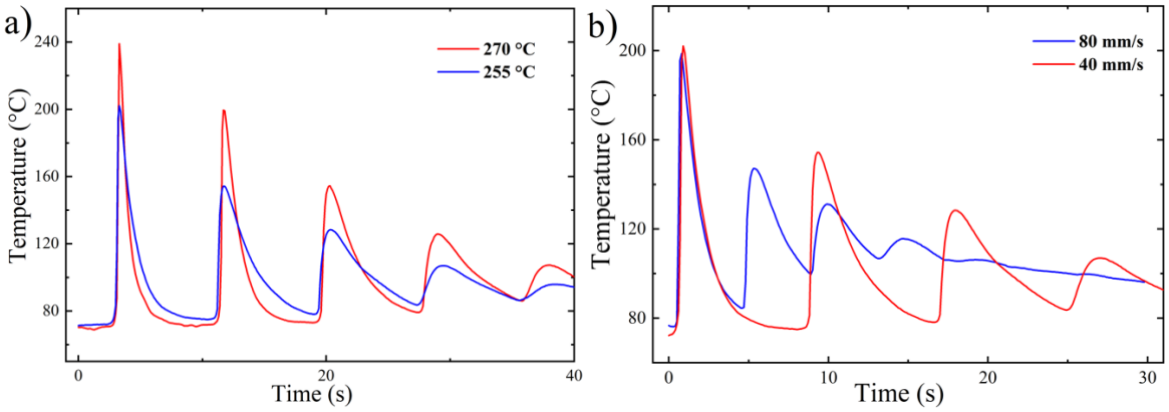

Figure 7.14. Thermal profiles of the first layer of Novamid ID 1070 deposited on the plate for different printing conditions at the same deposition speed (40 mm/s) (a) and the same nozzle temperature (255 °C) (b) respectively.

7.7 Conclusions

In this chapter, an approach was proposed to study the influence of crystallization during printing on the final properties, by selecting two polyamides with largely different crystallizability. In particular it was clearly assessed that the polyamide-6 homopolymer crystallizes at higher temperatures or in shorter times than the polyamide 6/6,6 copolymer, as expected from the molecular structure. The application of fast cooling protocols by means of a home-built device revealed a decrease in crystallinity as the cooling rate applied increases for both materials. By analyzing the printed parts via DSC, it is finally verified that during the printing process, for both materials, the maximum possible degree of crystallinity is reached. However, low printing speed for the homopolymer probably lead to the development of the mesomorphic modification. A direct measurement of the temperature profile of the filament during the printing process was attempted, and it was concluded that the first filament, after the fourth layer, is no longer affected by the heat generated by the deposition of the subsequent layers, as its temperature remains almost constant as the printing process continues. This temperature is higher than the glass transition temperature of the polymer, which is why, at the end of printing, the polymer was able to reach the maximum degree of developable crystallinity. In the tensile strength or weld strength tests for the homopolymer, a “bell-shaped” trend was obtained, indicating that the best tensile properties are obtained in samples printed at intermediate printing speeds. The maximum loads are in any case lower than the yield strength, so no plastic deformation of the material occurs at the interface between the two layers. In the copolymer, on the other hand, the best tensile strength was found at low printing

speeds with an important decrease at higher speeds. This fact can be explained by assuming that at high speeds a meaningful degree of molecular orientation is obtained in the transverse direction with respect to the loading. This study represents a first approach in developing deeper knowledge regarding the behavior of semicrystalline polymeric materials in the 3D printing process.

8 LIGHT SCATTERING APPROACH TO THE IN-SITU MEASUREMENT OF POLYMER CRYSTALLIZATION DURING 3D PRINTING

8.1 Introduction

This chapter focuses on the implementation of a simple optical setup to follow the crystallization process in-situ during pritings. The new setup exploits light scattering generated during filament deposition and cooling. To this purpose, the beam scattered by a growing 3D printed wall geometry is collected on a semi-transparent screen during the deposition for both amorphous polylactide and a semicrystalline polyamide copolymer. The clear differences between the scattered light patterns and their temporal evolution confirm the suitability of the proposed set-up for the in-situ measurement of crystallization during the FDM process. It must be remembered that this set-up does not allow to obtain structural information, but only on turbidity, unlike, for example, synchrotron techniques in which, thanks to a smaller beam diameter, it is also possible to probe a single layer.

8.2 Thermal characterization

Figure 8.1 reports the differential scanning calorimetry (DSC) analysis for the two materials, subjected to cooling and heating runs at 10 °C/min. While polyamide crystallizes during cooling at 10 °C/min, as evidenced by the exothermic peak around 180 °C and the subsequent melting centered at about 220 °C, PLA 4043D does not show clear traces of crystallization in the cooling step. The subsequent heating shows a very evident glass transition around 60 °C and a minimal melting endotherm due to the development of a limited crystallinity on heating (notice the very broad exothermic crystallization peak). The degree of crystallinity calculated for PLA 4043D is around 0.5 % ($\Delta H_{cold\text{-}cryst}$=0.46 J/g), which confirms our hypothesis of considering it as an amorphous material.

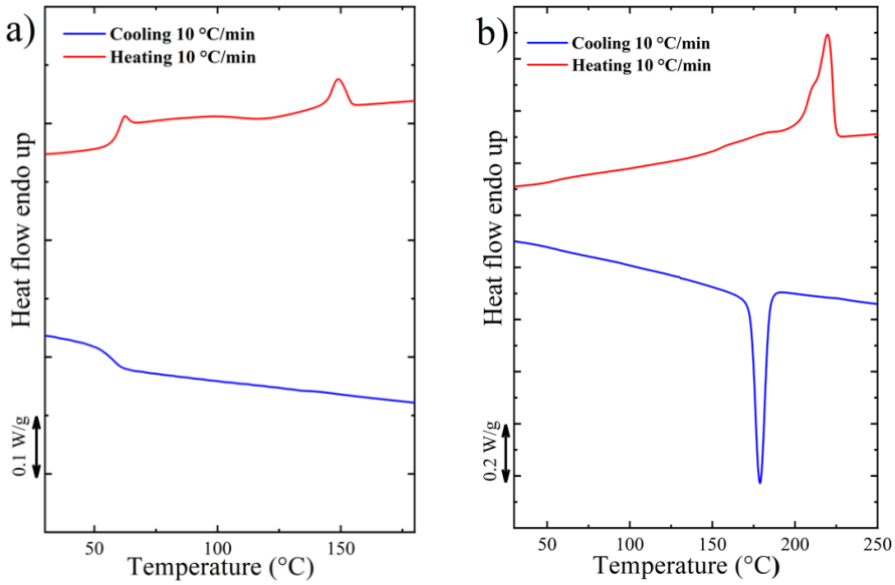

Figure 8.1. DSC cooling (blue) and heating (red) ramps at 10 °C/min for (a) PLA 4043D and (b) Novamid ID 1030.

8.3 Light scattering measurements

Light-scattering measurements consist of acquiring the scattered intensity generated by a collimated light beam hitting the samples.[248] Figure 8.2 shows the different scattering patterns measured for specific printing conditions for the amorphous PLA 4043D and the semicrystalline Novamid ID 1030. The amorphous PLA object scatters the light mainly along the vertical direction (Figure 8.2a). Conversely, the semicrystalline Novamid ID 1030 scatters isotropically (Figure 8.2b). This observation is of considerable importance as it suggests that the isotropic scattering arises from the presence of crystallites in the polyamide printed part. Crystallites are, in fact, very effective scattering centers that cause isotropic light diffusion. Conversely, vertical scattering is presumably due to the horizontal interfaces between the different layers for the amorphous material.

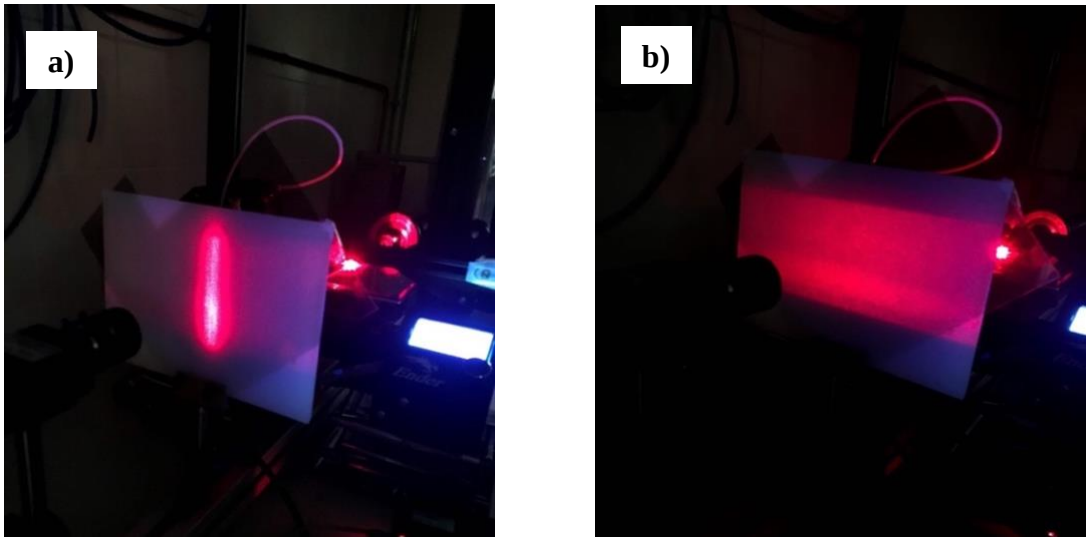

Figure 8.2. Digital images collected for (a) PLA 4043D and (b) Novamid ID 1030 once the printed object has reached the total coverage of the laser beam.

We also monitored the dynamic evolution of the scattering pattern during printing the two polymers in different printing conditions. The acquisition started in correspondence with the deposition of the first layer and lasted until the intensity pattern of the scattered light reached a steady condition. Figure 8.3a-b shows some frames extracted at 5, 15, 25, and 35 s for the two polymers. Note that in both cases, the direct beam spot (transmitted intensity) at the center of the image decreases in intensity along the process while the scattered intensity increases.

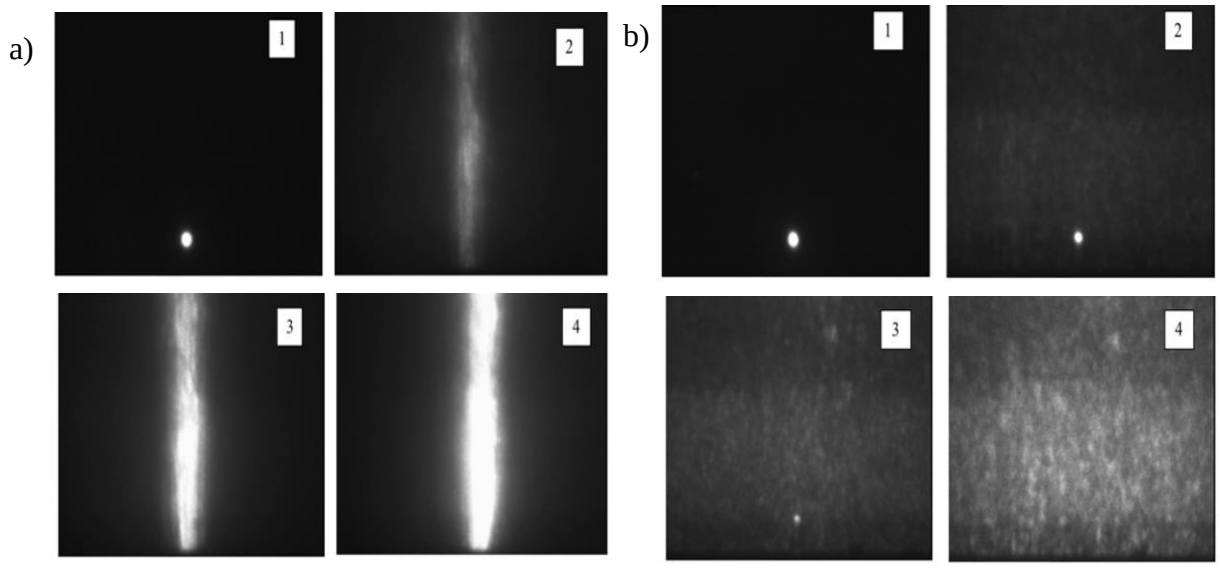

Figure 8.3. Frames extracted at different times during printing of (a) the PLA 4043D and (b) the Novamid ID 1030 printed at a speed of 7 mm/s. The first image (1) shows the beam before interacting with the printing object, the last (4) is instead collected when the light beam is entirely covered by the object.

Image analysis was carried out on rectangular areas to monitor the scattered light dynamics in different spatial regions. In particular, three areas of interest have been selected for each frame. Figure 8.4 shows an example of the integration area selected with imageJ in the case of Novamid ID 1030 printed at 7 mm/s.

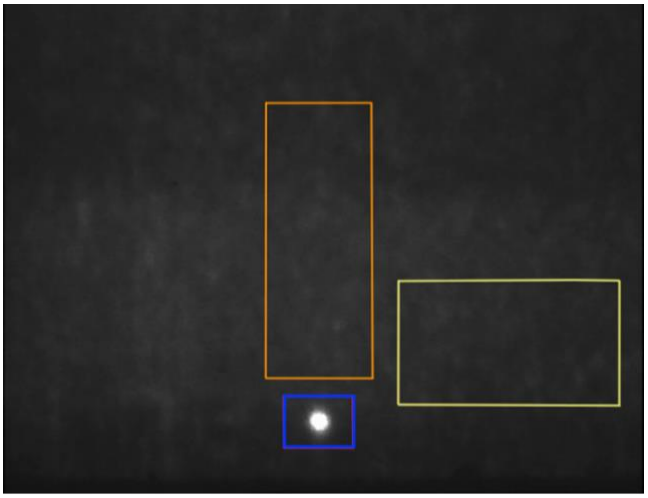

Figure 8.4. Integration areas selected with imageJ to monitor the evolution of scattered light in the case of the Novamid ID 1030 printed at 7 mm/s.

One vertically aligned area along with the scattering pattern of the amorphous polymer, was selected to monitor the anisotropic scattering arising from the macroscopic morphological features of the print. The horizontal area centered in the region where only the crystalline material scatters was chosen to monitor scattering intensity from crystallites. Finally, a small, squared area placed in correspondence of the direct beam allowed us to monitor the transmitted intensity. The integrated intensity reported in Figure 8.6a for specimens printed at a speed of 7 mm/s shows that amorphous PLA scatters only in the direction perpendicular to the deposition one. Indeed, the integrated scattered intensity for PLA increases with the printing time only along the vertical axis, while the intensity value on the horizontal one is steady at about zero for the entire process. Conversely, for the semicrystalline material, the light reaches both the horizontal and the vertical regions with the same intensity (Figure 8.6b). The experiments were repeated using two different printing speeds: 10.7 and 4.5 mm/s. In all analyzed cases, the scattered intensity increased in the horizontal and vertical areas while the intensity detected in the area containing the direct laser beam decreased. Figure 8.6 also shows that all the intensity profiles were characterized by periodic minima when the nozzle crosses the laser beam. These minima allowed us to estimate the time for the deposition of a single filament.

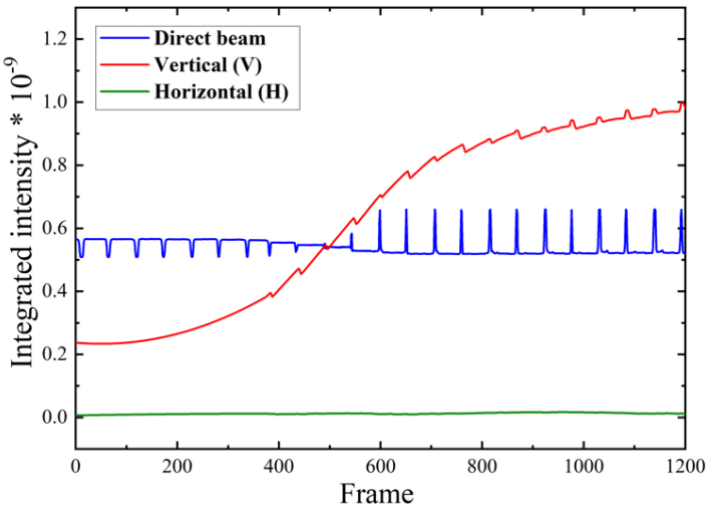

Figure 8.5. Integrated intensities in the three rectangular areas for a sample of PLA 4043D printed at a speed of 10.7 mm/s and a nozzle temperature of 200 °C.

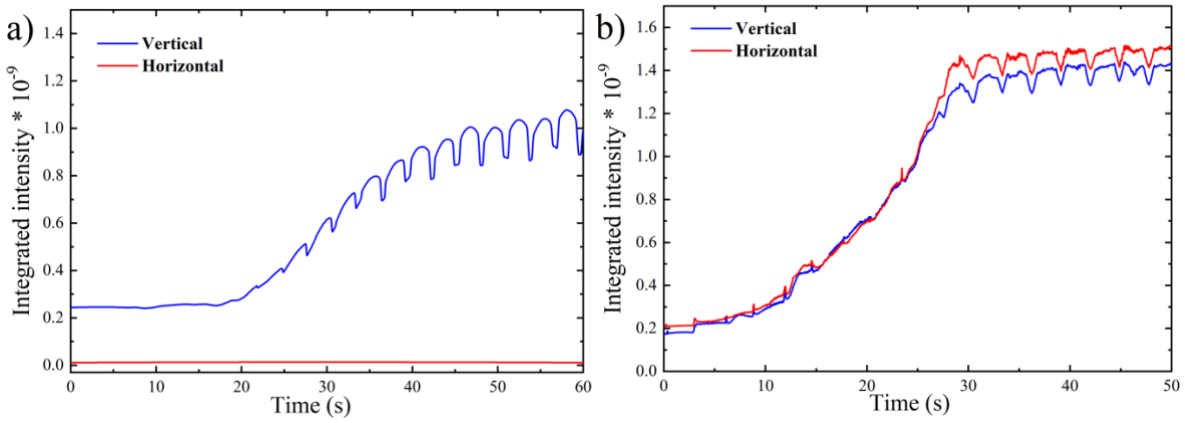

Figure 8.6. The trend of scattered light intensity in the vertical and horizontal areas selected for (a) a sample of PLA 4043D and (b) a sample of Novamid ID 1030 printed at a speed of 75% (7 mm/s).

The zero time of the process was determined using Wolfram Mathematica software (Wolfram Research, Champaign, IL, USA) by comparing the integrated light intensity data to the intensity evaluated in the area containing the transmitted intensity, which starts to decrease when the first filament covers the laser beam. As visible in Figure 8.5, where it is shown as an example the integrated intensities in the three rectangular areas for a sample of PLA 4043D printed at 10.7 mm/s and a nozzle temperature of 200 °C, and Figure 8.6, the integrated light increases from a minimum to a maximum for the scattered light and decreases from a maximum

to a minimum for the transmitted light. Then, all the integrated intensities were normalized as follows:

$$I_{norm} = \frac{I(t) - I_{min}}{I_{max} - I_{min}} \qquad (8.1)$$

where I(t) represents the intensity value at generic time t, I_{min} is the initial value of the integrated intensity at time zero, while I_{max} is the highest scattered intensity value reached at the end of the print. Figure 8.7 compares the normalized scattered intensity evaluated for two printing speeds (4.5 and 10.7 mm/s a) for PLA 4043D in the vertical region (Figure 8.7a) and the Novamid ID 1030 in the horizontal region (Figure 8.7b). Both scattered intensities follow a sigmoidal trend. For the amorphous polymer, the increase in scattered intensity along the vertical direction follows a similar trend but does not seem to reach the asymptotic value. The dynamics measured for polymers printed at the same speed are different, suggesting that the light scattering has a different origin for the two polymers. If the light scattered by the amorphous and transparent PLA can presumably be associated with the coverage of the beam by the printing part, in the case of polyamide, this hypothesis is not likely. Indeed, the kinetics are different, although the objects are printed at the same speed.

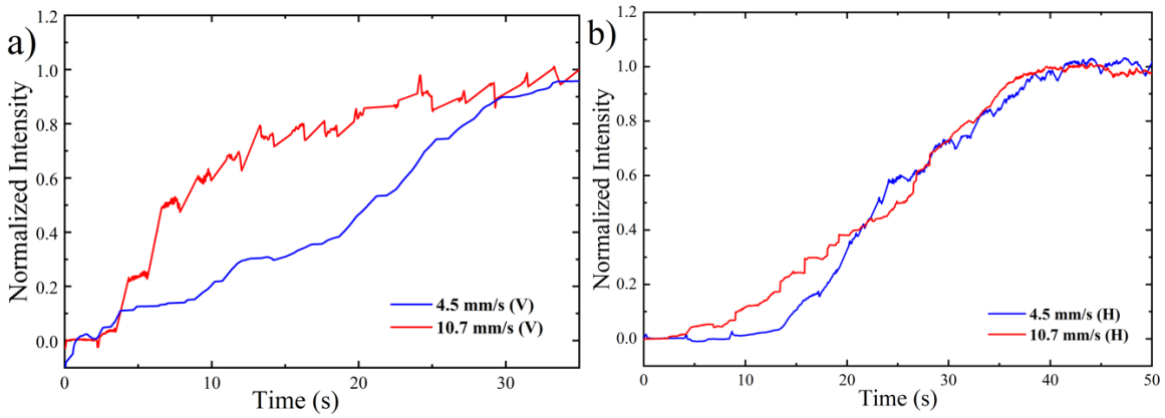

Figure 8.7. Normalized scattered light intensities for (a) PLA 4043D in the vertical area and (b) Novamid ID 1030 in the horizontal area during printing at speeds of 4.5 and 10.7 mm/s.

From the normalized scattered intensity of Figures 8.7a and 8.7b, we extracted two characteristic process times, $t_{0.1}$ and $t_{0.5}$, representing the times required to reach 10% and 50% of the maximum intensity in both directions. The characteristic times are reported in Table 8.1 for the various explored conditions.

Table 8.1. Characteristic times for light scattering evaluated for the two materials.

	Print speed (mm/s)	**$t_{0.1}$ (V) (s)**	**$t_{0.1}$ (H) (s)**	**$t_{0.5}$ (V) (s)**	**$t_{0.5}$ (H) (s)**
PLA 4043D	10.7	3.75	-	12.05	-
	7	5.75	-	15	-
	4.5	8.35	-	23	-
Novamid ID 1030	10.7	9.15	10.65	21.85	20.05
	7	8.95	8.65	18.85	19.35
	4.5	8.85	14.75	24.25	23.05

As expected, the characteristic times decrease upon increasing the printing speed for both materials. Such a decrease is visible in Figure 8.8, which reports $t_{0.5}$ as a function of deposition rate. While the values of $t_{0.5}$ are similar for low printing speeds, they diverge at higher speed values, where the amorphous polymer exhibits faster light scattering kinetics than the semicrystalline one. The data suggest that the semicrystalline polymer $t_{0.5}$ is affected by the crystallization process and follows a non-linear dependence on the printing speed.

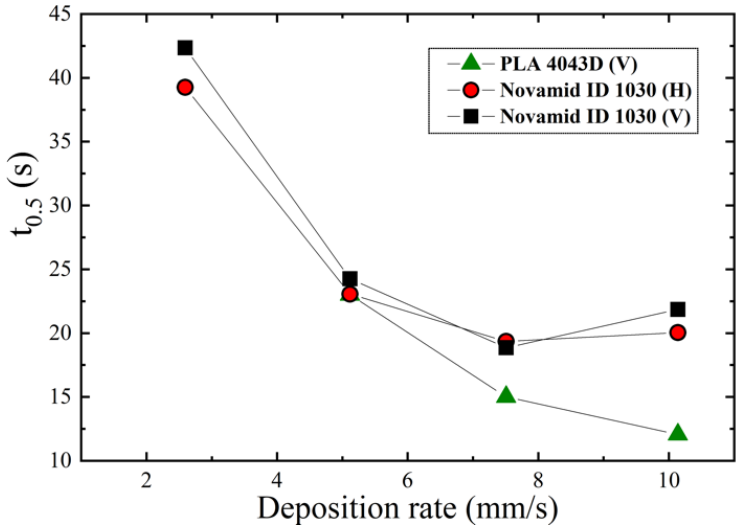

Figure 8.8. Time to reach 50% of the maximum intensity of the scattered light for Novamid ID 1030 and PLA 4043D at different printing speeds.

To properly consider the variation in the deposition kinetics of the layer, we took as a reference the number of deposited layers in the time interval necessary to reach 10% and 50% of the final scattered intensity. This behavior also provides further experimental evidence that a different phenomenon than the simple coverage of the light beam due to the growing number of layers during the early stage of the print is observed in the semicrystalline polymer. If the light

scattering was caused simply by the coverage, the chosen percentage of scattered light intensity would always be achieved after the deposition of a given number of layers, regardless of the printing speed. The average number of layers deposited at $t_{0.5}$ for the various deposition speeds were calculated as the ratio between the $t_{0.5}$ and the time of deposition of a single layer (Δt).

The results are reported in Figure 8.9a-b. Concerning PLA 4043D, the number of layers printed at $t_{0,1}$ and $t_{0.5}$ is practically constant for different deposition speeds and approaches 1.5 and 5 layers, respectively. This result confirms that the kinetics of the scattered light generation in the vertical direction for the amorphous polymer describes the printing process purely, and is related to horizontal interface formation between the various layers. For Novamid ID 1030 instead, the number of layers printed at $t_{0.1}$ and $t_{0.5}$ increases with the deposition speed, meaning that the kinetics of scattered light generation in the semicrystalline polymer increases more than linearly with the deposition speed. This effect is then ascribed to phenomena independent from the pure beam coverage. It is then reasonable to state that the scattering is affected by the development of the semicrystalline structures.

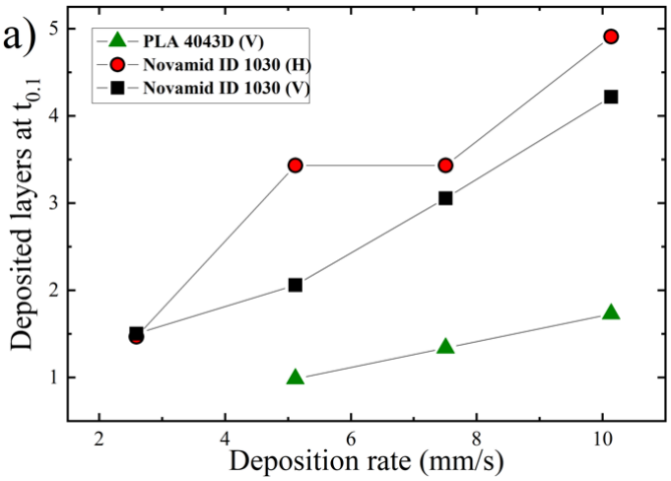

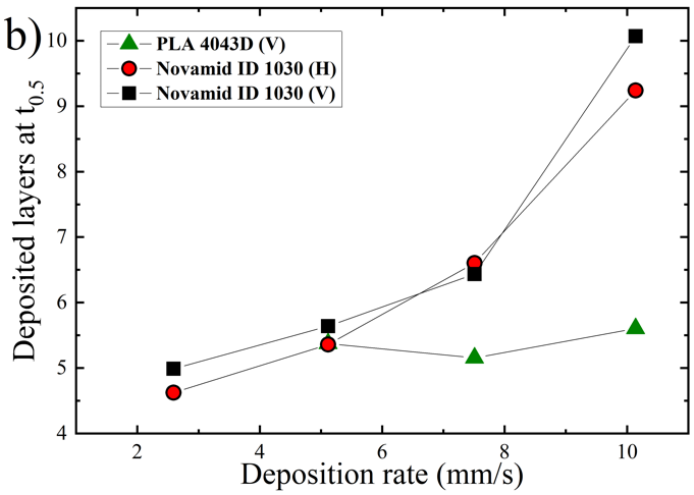

Figure 8.9. The number of deposited layers for PLA 4043D and Novamid ID 1030 as a function of the deposition rate at (a) t0.1 and (b) t0.5. Lines joining the data serve to guide the eyes.

The concept just illustrated is also evident by reporting the rate for the achievement of 10% and 50% of the maximum intensity ($1/t_{0.1}$ or $1/t_{0.5}$) and the reciprocal of the deposition time of a single layer ($1/\Delta t$) as a function of the deposition rate (figure 8.10a-b). In the case of PLA 4043D, there is a substantially linear relationship between the two parameters mentioned above and the deposition rate. Conversely, for the semicrystalline polymer, the light scattering rates reach a plateau value at high printing speeds. Considering $1/t_{0.1}$ and $1/t_{0.5}$ as the rate at which 10% and 50% of the final crystallinity is achieved, these are comparable to the deposition rate for low values of printing speed, while they increase less than the deposition rate with the increase of the explored print speed range. In other words, crystallization kinetics is comparable to the printing speed at low rates but slower than it at higher rates.

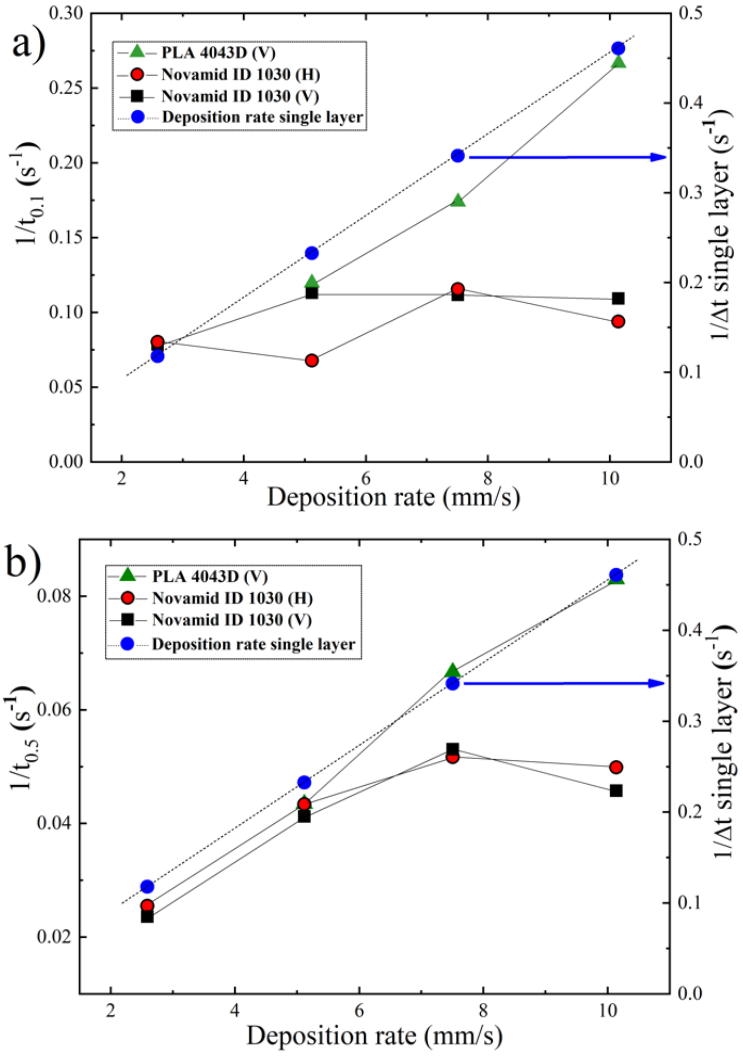

Figure 8.10. Speed for reaching a) 10% of the maximum intensity ($1/t_{0.1}$) and b) 50% of the maximum intensity ($1/t_{0.5}$) and speed of completion of a single layer ($1/\Delta t$) as a function of the deposition rate (mm/s).

Summarizing, it is clear that the printing process dominates the light scattering phenomenon in the case of PLA 4043D. Indeed, the rate of light scattering generation follows the rate of layer deposition closely. On the other hand, the deposition process is less influential in the kinetics of scattered light generation for Novamid ID 1030. In this second case, the light is scattered due to the crystallization process, which does not seem strongly influenced by the increase in printing speed. Thus, this result indicates that, for this material and the specific conditions adopted, the role of flow-induced crystallization is not particularly important. These results confirm that simple light scattering measurements can be employed to evaluate crystallization processes in FDM 3D printing.

Another valid approach to monitor the evolution of crystallinity in FDM printed parts is the combination of IR thermography and Fast Scanning Chip Calorimetry measurements. By

comparing the semi-crystallization times in the figure X and those calculated for layer 10 by Vaes et al., on a similar material, comparable values are obtained, confirming the effectiveness of both techniques for this type of experiment.[249]

8.4 Conclusions

In this chapter, it is proposed a new simple method to investigate the crystallization of a polyamide copolymer during 3D printing as the speed of the process is varied. The technique relies on light scattering measurement and allows us to compare the behavior of crystalline and amorphous polymers. We observed a clear difference in the spatial distribution of the laser light scattered from the two materials. The amorphous material gave rise to a scattering pattern with vertical streaks, generated by the horizontal interfaces formed during the object build-up. Conversely, the semicrystalline polymer resulted in isotropic scattering. Furthermore, while the evolution of intensity scattered follows the deposition kinetics of the successive polymer layers for the amorphous polymer, this is not valid for the semicrystalline polymer, where the light scattering is mainly affected by the formation of crystallites. We demonstrated that the difference between the scattered light patterns and their temporal evolutions during printing allows confirming this simple setup's suitability for observing the development of crystallization in-situ during the printing process. Improvements in the setup developed in this work will enable us to obtain important information on the crystallization of materials in this new polymer processing method. Moreover, this technique could be a useful tool for on-line monitoring and process control, especially in the scouting of new printing materials

9 CONCLUSIONS & OUTLOOK

One of the problems of the manufacts obtained with FDM is the poor adhesion between adjacent layers, which can lead to a significant drop in mechanical properties. The application of high shear stresses and the non-isothermal nature of the process can lead, in fact, to the orientation of the macromolecules at the interface, hindering the formation of entanglements and thus reducing the weld strength.
The purpose of this Ph.D. thesis was to study for different materials, as the printing conditions vary, how the intrinsic features of the polymers can influence the final mechanical properties of the products, with particular reference to those obtained for a test geometry. The behavior of both amorphous materials, including some copolymers based on PLA or co-polyesters, and other semi-crystalline polymers such as polyamides, have been studied.

In the case of a commercial PLA, we found that the drop in mechanical properties with stronger printing conditions (i.e. high print speed and low nozzle temperature) is due to the increase of residual molecular alignment at the interface region between adjacent layers.
Moreover, with the support of a molecularly-aware model, we discovered that the real reason of poor mechanical properties for some printing conditions is linked to a lower entanglements density at the interfaces.
Molecular weight also appears to strongly influence the mechanical properties of printed parts. In fact, by comparing six commercial PLA having different molecular masses and D-lactide comonomer content, we found a decrease in mechanical strength with Z, whereas the effect of the D-lactide content is negligible. Subsequently, the combination of infrared microspectroscopy measurements with continuum modelling (in collaboration with Lincoln University) showed that a significant degree of molecular alignment is frozen into the sample for high-molar-mass materials whereas low-molar-mass samples exhibits isotropy.
These results state how achieving molecular isotropy in the weld is clearly an interplay between temperature and molecular weight, thus indicating how the latter should be a key parameter in filament deposition 3D printing.
Subsequently, by carrying out tensile tests of specimens printed using two commercial co-polyesters characterized by a different chain structure, we found similar mechanical properties, despite the in-situ temperature measurements of the same materials during printing showing clearly different weld times. However, with the support of the above-mentioned molecular model we showed that both materials demonstrate similar molecular properties (residual

polymer stretch and alignment) within the weld region. However, the modeling suggests that it is the increased stiffness of the high T_g polymer that mitigates residual anisotropy and therefore any effect increased anisotropy may have on weld strength.

In general, Chapters 3,4 and 5 therefore revealed the presence of molecular orientation at the weld interlayer if very high deposition rates and low extrusion temperatures are used, thus making this thesis relevant in case such conditions are met in industrial 3d printing.

Crystallization also plays an important role in the final properties of molded parts. By studying the tensile strength of a commercial polyamide-6 as a function of process conditions, a bell-shaped trend was obtained, with the poor mechanical properties obtained at low printing speeds justified by the presence of mesophase.

Finally, we presented a new setup based on light scattering for in-situ observation of polymer crystallization during printing. To this purpose, the beam scattered by a growing 3D printed wall geometry was collected on a semi-transparent screen during the deposition for both amorphous polylactide and a semicrystalline polyamide copolymer. While the amorphous polymer scattered light anisotropically and generated a vertical scattering pattern, the semicrystalline polyamide produced isotropic scattering, demonstrating this simple setup's suitability for observing the development of crystallization in-situ during the printing process.

Future work may be focused on a more in-depth study of semi-crystalline polymers employed in FDM technology. In fact, while the behavior of amorphous materials seems to have been clarified by now, the effect of crystallization on the final properties of printed products has not yet been definitively understood. The improvement of the set-up for light scattering measurements could be a good attempt to investigate more precisely the morphology of 3D printed crystals and, consequently, correlate their characteristics to the weld strength of the samples.

References

(1) Turner, B.; Strong, R.; Gold, S. A Review of Melt Extrusion Additive Manufacturing Processes: I. Process Design and Modeling. *Rapid Prototyp. J.* **2014**, *20*. https://doi.org/10.1108/RPJ-01-2013-0012.

(2) Ahn, S.; Montero, M.; Odell, D.; Roundy, S.; Wright, P. K. Anisotropic Material Properties of Fused Deposition Modeling ABS. *Rapid Prototyp. J.* **2002**, *8* (4), 248–257. https://doi.org/10.1108/13552540210441166.

(3) McIlroy, C.; Olmsted, P. D. Disentanglement Effects on Welding Behaviour of Polymer Melts during the Fused-Filament-Fabrication Method for Additive Manufacturing. *Polymer* **2017**, *123*, 376–391. https://doi.org/10.1016/j.polymer.2017.06.051.

(4) McIlroy, C.; Olmsted, P. Deformation of an Amorphous Polymer during the Fused-Filament-Fabrication Method for Additive Manufacturing. *J. Rheol.* **2016**, *61*. https://doi.org/10.1122/1.4976839.

(5) Ianniruberto, G.; Marrucci, G. Convective Constraint Release (CCR) Revisited. *J. Rheol.* **2013**, *58*. https://doi.org/10.1122/1.4843957.

(6) Wang, X.; Jiang, M.; Zhou, Z.; Gou, J.; Hui, D. 3D Printing of Polymer Matrix Composites: A Review and Prospective. *Compos. Part B Eng.* **2017**, *110*, 442–458. https://doi.org/10.1016/j.compositesb.2016.11.034.

(7) Daminabo, S. C.; Goel, S.; Grammatikos, S. A.; Nezhad, H. Y.; Thakur, V. K. Fused Deposition Modeling-Based Additive Manufacturing (3D Printing): Techniques for Polymer Material Systems. *Mater. Today Chem.* **2020**, *16*, 100248. https://doi.org/10.1016/j.mtchem.2020.100248.

(8) Wu, H.; Fahy, W. P.; Kim, S.; Kim, H.; Zhao, N.; Pilato, L.; Kafi, A.; Bateman, S.; Koo, J. H. Recent Developments in Polymers/Polymer Nanocomposites for Additive Manufacturing. *Prog. Mater. Sci.* **2020**, *111*, 100638. https://doi.org/10.1016/j.pmatsci.2020.100638.

(9) ISO/ASTM 52900:2015, Additive Manufacturing - General Principles - Termi-Nology. International Organization for Standardization, Geneva, Switzerland. **2015**.

(10) Ligon, S. C.; Liska, R.; Stampfl, J.; Gurr, M.; Mülhaupt, R. Polymers for 3D Printing and Customized Additive Manufacturing. *Chem. Rev.* **2017**, *117* (15), 10212–10290. https://doi.org/10.1021/acs.chemrev.7b00074.

(11) Gao, W.; Zhang, Y.; Ramanujan, D.; Ramani, K.; Chen, Y.; Williams, C. B.; Wang, C. C. L.; Shin, Y. C.; Zhang, S.; Zavattieri, P. D. The Status, Challenges, and Future of Additive Manufacturing in Engineering. *Comput.-Aided Des.* **2015**, *69*, 65–89. https://doi.org/10.1016/j.cad.2015.04.001.

(12) Ivanova, O.; Williams, C.; Campbell, T. Additive Manufacturing (AM) and Nanotechnology: Promises and Challenges. *Rapid Prototyp. J.* **2013**, *19*, 353. https://doi.org/10.1108/RPJ-12-2011-0127].

(13) González-Henríquez, C. M.; Sarabia-Vallejos, M. A.; Rodriguez-Hernandez, J. Polymers for Additive Manufacturing and 4D-Printing: Materials, Methodologies, and Biomedical Applications. *Prog. Polym. Sci.* **2019**, *94*, 57–116. https://doi.org/10.1016/j.progpolymsci.2019.03.001.

(14) Jacobs, P. F. Stereolithography and Other Rp&m Technologies: From Rapid Prototyping to Rapid Tooling; **1995**.

(15) Jacobs, P. F.; Reid, D. T. *Rapid Prototyping & Manufacturing: Fundamentals of Stereolithography*; Society of Manufacturing Engineers: Dearborn, MI, **1992**.

(16) Noorani, R. *Rapid Prototyping. Principles and Application*; Wiley: Hoboken, NJ, 2006.

(17) Pham, D. T.; Gault, R. S. A Comparison of Rapid Prototyping Technologies. *Int. J.*

Mach. Tool Manuf. **1998**, *38*, 1257–1287.
(18) Wendel, B.; Rietzel, D.; Kühnlein, F.; Feulner, R.; Hülder, G.; Schmachtenberg, E. Additive Processing of Polymers. *Macromol. Mater. Eng.* **2008**, *293* (10), 799–809. https://doi.org/10.1002/mame.200800121.
(19) Wohlers, T.; Caffrey, T. Additive Manufacturing and 3D Printing State of the Industry. *Wohlers Associates: Fort Collins, CO* **2013**.
(20) *Additive Manufacturing Market Size, Share & Trends Analysis Report By Component, By Printer Type, By Technology, By Software, By Application, By Vertical, By Material, By Region, And Segment Forecasts, 2022 - 2030*.
(21) Wohlers Report 2015:3D Printing and Additive Manufacturing State of the Industry Wohlers Associates: Fort Collins, CO. **2015**.
(22) Meakin, J.; Shepherd, D.; Hukins, D. Fused Deposition Models from CT Scans. *Br. J. Radiol. - BRIT J RADIOL* **2004**, *77*, 504–507.
(23) Al-Ahmad, A.; Wiedmann-Al-Ahmad, M.; Carvalho, C.; Hellwig, E. *Bacterial and Candida Albicans Adhesion on Rapid Prototyping-Produced Scaffolds Manufactured as Bone Replacement Materials*; **2011**.
(24) Laschke, M.; Rücker, M.; Jensen, G.; Carvalho, C.; Mülhaupt, R.; Gellrich, N.-C.; Menger, M. Improvement of Vascularization of PLGA Scaffolds by Inosculation of In Situ-Preformed Functional Blood Vessels With the Host Microvasculature. *Ann. Surg.* **2009**, *248*, 939–948. https://doi.org/10.1097/SLA.0b013e31818fa52f.
(25) Rücker, M.; Laschke, M. W.; Junker, D.; Carvalho, C.; Schramm, A.; Mülhaupt, R.; Gellrich, N.-C.; Menger, M. D. Angiogenic and Inflammatory Response to Biodegradable Scaffolds in Dorsal Skinfold Chambers of Mice. *Biomaterials* **2006**, *27* (29), 5027–5038. https://doi.org/10.1016/j.biomaterials.2006.05.033.
(26) Rücker, M.; Laschke, M.; Junker, D.; Carvalho, C.; Tavassol, F.; Mülhaupt, R.; Gellrich, N.-C.; Menger, M. Vascularization and Biocompatibility of Scaffolds Consisting of Different Calcium Phosphate Compounds. *J. Biomed. Mater. Res. A* **2008**, *86*, 1002–1011. https://doi.org/10.1002/jbm.a.31722.
(27) Gibson, I.; Kvan, T.; Ming, L. Rapid Prototyping for Architectural Models. *Rapid Prototyp. J.* **2002**, *8*, 91–95. https://doi.org/10.1108/13552540210420961.
(28) Wannarumon, S.; Bohez, E. Rapid Prototyping and Tooling Technology in Jewelry CAD. *Comput.-Aided Des. Appl.* **2004**, *1*. https://doi.org/10.1080/16864360.2004.10738300.
(29) Hofmann, M. 3D Printing Gets a Boost and Opportunities with Polymer Materials. *ACS Macro Lett.* **2014**, *3* (4), 382–386. https://doi.org/10.1021/mz4006556.
(30) Tumbleston, J. R.; Shirvanyants, D.; Ermoshkin, N.; Janusziewicz, R.; Johnson, A. R.; Kelly, D.; Chen, K.; Pinschmidt, R.; Rolland, J. P.; Ermoshkin, A.; Samulski, E. T.; DeSimone, J. M. Continuous Liquid Interface Production of 3D Objects. *Science* **2015**, *347* (6228), 1349–1352. https://doi.org/10.1126/science.aaa2397.
(31) Decker, C. Light-Induced Crosslinking Polymerization. *Polym. Int.* **2002**, *51* (11), 1141–1150. https://doi.org/10.1002/pi.821.
(32) Kruth, J.-P.; Levy, G.; Klocke, F.; Childs, T. H. C. Consolidation Phenomena in Laser and Powder-Bed Based Layered Manufacturing. *CIRP Ann.* **2007**, *56* (2), 730–759. https://doi.org/10.1016/j.cirp.2007.10.004.
(33) Agarwala, M. K.; Jamalabad, V. R.; Langrana, N. A.; Safari, A.; Whalen, P. J.; Danforth, S. C. Structural Quality of Parts Processed by Fused Deposition. *Rapid Prototyp. J.* **1996**, *2* (4), 4–19. https://doi.org/10.1108/13552549610732034.
(34) Lee, C. S.; Kim, S. G.; Kim, H. J.; Ahn, S. H. Measurement of Anisotropic Compressive Strength of Rapid Prototyping Parts. *3rd Int. Conf. Adv. Form. Manuf. Technol.* **2007**, *187–188*, 627–630. https://doi.org/10.1016/j.jmatprotec.2006.11.095.
(35) Chacón, J. M.; Caminero, M. A.; García-Plaza, E.; Núñez, P. J. Additive Manufacturing

of PLA Structures Using Fused Deposition Modelling: Effect of Process Parameters on Mechanical Properties and Their Optimal Selection. *Mater. Des.* **2017**, *124*, 143–157. https://doi.org/10.1016/j.matdes.2017.03.065.
(36) Monzon, M.; Ortega, Z.; Hernández, A.; Paz Hernández, R.; Ortega, F. Anisotropy of Photopolymer Parts Made by Digital Light Processing. *Materials* **2017**, *10*, 64. https://doi.org/10.3390/ma10010064.
(37) Kumar, S.; Kruth, J.-P. Composites by Rapid Prototyping Technology. *Mater. Des.* **2010**, *31* (2), 850–856. https://doi.org/10.1016/j.matdes.2009.07.045.
(38) Josef Prusa's Mk2 Set to Enter the Multi-Color 3D Printer Race with a Clever Twist. Http://Www.3ders.Org/Articles/20160929 (Ac- Cessed Dec 29, 2016).
(39) Vaezi, M.; Chianrabutra, S.; Mellor, B.; Yang, S. Multiple Material Additive Manufacturing – Part 1: A Review. *Virtual Phys. Prototyp.* **2013**, *8* (1), 19–50. https://doi.org/10.1080/17452759.2013.778175.
(40) Choi, J.-W.; Kim, H.-C.; Wicker, R. Multi-Material Stereolithography. *J. Mater. Process. Technol.* **2011**, *211* (3), 318–328. https://doi.org/10.1016/j.jmatprotec.2010.10.003.
(41) Inamdar, A.; Magana, M.; Medina, F.; Grajeda, Y.; Wicker, R. Development of an Automated Multiple Material Stereolithography Machine. *Proc. 17th Annu. Solid Free. Fabr. Symp. Austin TX* **2006**, 624–635.
(42) Lappo, K.; Jackson, B.; Wood, K.; Bourell, D.; Beaman, J. Discrete Multiple Material Selective Laser Sintering (M̂2SLS): Experimental Study of Part Processing. *SFF Symp. Proc.* **2003**, *14*, 109–119.
(43) Xie, D.; Zhang, H.; Shu, X.; Xiao, J.; Cao, S. Multi-Materials Drop-on-Demand Inkjet Technology Based on Pneumatic Diaphragm Actuator. *Sci. China Technol. Sci.* **2010**, *53*, 1605–1611. https://doi.org/10.1007/s11431-010-3149-7.
(44) Ratheesh, G.; Venugopal, J.; Chinnappan, A.; Ezhilarasu, H.; Sadiq, A.; Ramakrishna, S. 3D Fabrication of Polymeric Scaffolds for Regenerative Therapy. *ACS Biomater. Sci. Eng.* **2016**, *3*. https://doi.org/10.1021/acsbiomaterials.6b00370.
(45) Shafiee, A.; Atala, A. Tissue Engineering: Toward a New Era of Medicine. *Annu. Rev. Med.* **2016**, *68*, 22.1-22.12. https://doi.org/10.1146/annurev-med-102715-092331.
(46) Magin, C.; Alge, D.; Anseth, K. Bio-Inspired 3D Microenvironments: A New Dimension in Tissue Engineering. *Biomed. Mater.* **2016**, *11*, 022001. https://doi.org/10.1088/1748-6041/11/2/022001.
(47) Do, A.-V.; Khorsand, B.; Geary, S.; Salem, A. 3D Printing of Scaffolds for Tissue Regeneration Applications. *Adv. Healthc. Mater.* **2015**, *4*. https://doi.org/10.1002/adhm.201500168.
(48) Melchels, F.; Domingos, M.; Klein, T.; Malda, J.; Bartolo, P.; Hutmacher, D. Additive Manufacturing of Tissues and Organs. *Prog. Polym. Sci.* **2012**, *37*, 1079–1104. https://doi.org/10.1016/j.progpolymsci.2011.11.007.
(49) Husár, B.; Hatzenbichler, M.; Mironov, V.; Liska, R.; Stampfl, J.; Ovsianikov, A. 6 - Photopolymerization-Based Additive Manufacturing for the Development of 3D Porous Scaffolds. In *Biomaterials for Bone Regeneration*; Dubruel, P., Van Vlierberghe, S., Eds.; Woodhead Publishing, **2014**; pp 149–201. https://doi.org/10.1533/9780857098104.2.149.
(50) Husár, B.; Liska, R. Vinyl Carbonates, Vinyl Carbamates, and Related Monomers: Synthesis, Polymerization, and Application. *Chem. Soc. Rev.* **2012**, *41* (6), 2395–2405. https://doi.org/10.1039/C1CS15232G.
(51) GIORDANO, R. A.; Wu, B. M.; Borland, S. W.; Cima, L. G.; Sachs, E. M.; Cima, M. J. Mechanical Properties of Dense Polylactic Acid Structures Fabricated by Three Dimensional Printing. *J. Biomater. Sci. Polym. Ed.* **1997**, *8* (1), 63–75. https://doi.org/10.1163/156856297X00588.
(52) Heeg, A. 3D-Bioplotting with Vital Cells, Albert- Ludwigs University, **2010**.

(53) Carvalho, C.; Landers, R.; Muelhaupt, R. Soft and Hard Implant Fabrication Using 3D-Bioplotting. *SFF Symp. Proc.* **2004**, 732−741.
(54) ASTM International - Standards Worldwide; Http://Www.Astm. Org/ (Accessed Mar 25, **2014**).
(55) ASTM F2792-12a. Standard Terminology for Additive Manufactur- Ing Technologies; ASTM International: West Conshohocken, PA, **2012**.
(56) Tofail, S. A. M.; Koumoulos, E. P.; Bandyopadhyay, A.; Bose, S.; O'Donoghue, L.; Charitidis, C. Additive Manufacturing: Scientific and Technological Challenges, Market Uptake and Opportunities. *Mater. Today* **2018**, *21* (1), 22–37. https://doi.org/10.1016/j.mattod.2017.07.001.
(57) Tyagi, S.; Yadav, A.; Deshmukh, S. Review on Mechanical Characterization of 3D Printed Parts Created Using Material Jetting Process. *CMAE'21* **2022**, *51*, 1012–1016. https://doi.org/10.1016/j.matpr.2021.07.073.
(58) Su, Z.; Zhao, K.; Ye, Z.; Cao, W.; Wang, X.; Liu, K.; Wang, Y.; Yang, L.; Dai, B.; Zhu, J. Overcoming the Penetration–Saturation Trade-off in Binder Jet Additive Manufacturing via Rapid in Situ Curing. *Addit. Manuf.* **2022**, 103157. https://doi.org/10.1016/j.addma.2022.103157.
(59) Tsai, Y.-C.; Leitz, K.-H.; Fardel, R.; Schmidt, M.; Arnold, C. B. Generating Nanostructures with Multiphoton Absorption Polymerization Using Optical Trap Assisted Nanopatterning. *Laser Assist. Net Shape Eng. 7 LANE 2012* **2012**, *39*, 669–673. https://doi.org/10.1016/j.phpro.2012.10.087.
(60) Huang, M.; Wu, Y.; Ou, J.; Huang, Y.; Wang, J.; Wu, S. 3D-Printing of Polymer-derived SiCN Ceramic Matrix Composites by Digital Light Processing. *J. Eur. Ceram. Soc.* **2022**, *42* (13), 5476–5483. https://doi.org/10.1016/j.jeurceramsoc.2022.06.056.
(61) Kim, T. Y.; Park, S.-H.; Park, K. Development of Functionally Graded Metamaterial Using Selective Polymerization via Digital Light Processing Additive Manufacturing. *Addit. Manuf.* **2021**, *47*, 102254. https://doi.org/10.1016/j.addma.2021.102254.
(62) Essmeister, J.; Altun, A. A.; Staudacher, M.; Lube, T.; Schwentenwein, M.; Konegger, T. Stereolithography-Based Additive Manufacturing of Polymer-Derived SiOC/SiC Ceramic Composites. *J. Eur. Ceram. Soc.* **2022**, *42* (13), 5343–5354. https://doi.org/10.1016/j.jeurceramsoc.2022.06.021.
(63) Liu, T.; Guessasma, S.; Zhu, J.; Zhang, W.; Nouri, H.; Belhabib, S. Microstructural Defects Induced by Stereolithography and Related Compressive Behaviour of Polymers. *J. Mater. Process. Technol.* **2018**, *251*, 37–46. https://doi.org/10.1016/j.jmatprotec.2017.08.014.
(64) Calignano, F.; Giuffrida, F.; Galati, M. Effect of the Build Orientation on the Mechanical Performance of Polymeric Parts Produced by Multi Jet Fusion and Selective Laser Sintering. *J. Manuf. Process.* **2021**, *65*, 271–282. https://doi.org/10.1016/j.jmapro.2021.03.018.
(65) Li, Z.; Sui, S.; Ma, X.; Tan, H.; Zhong, C.; Bi, G.; Clare, A. T.; Gasser, A.; Chen, J. High Deposition Rate Powder- and Wire-Based Laser Directed Energy Deposition of Metallic Materials: A Review. *Int. J. Mach. Tools Manuf.* **2022**, *181*, 103942. https://doi.org/10.1016/j.ijmachtools.2022.103942.
(66) Oropeza, D.; Firdosy, S.; Hofmann, D. C. Development of In-Plane SS316 to M300 Maraging Steel Gradients via Directed Energy Deposition. *Addit. Manuf. Lett.* **2022**, *3*, 100078. https://doi.org/10.1016/j.addlet.2022.100078.
(67) Crump, S.S. Apparatus and Method for Creating Three-Dimensional Objects. U.S. Patent No. 5,121,329A, **1992**.
(68) Singh, R.; Garg, H. Fused Deposition Modeling – A State of Art Review and Future Applications. In *Reference Module in Materials Science and Materials Engineering*; **2016**. https://doi.org/10.1016/B978-0-12-803581-8.04037-6.

(69) Turner, B. N.; Gold, S. A. A Review of Melt Extrusion Additive Manufacturing Processes: II. Materials, Dimensional Accuracy, and Surface Roughness. *Rapid Prototyp. J.* **2015**, *21* (3), 250–261. https://doi.org/10.1108/RPJ-02-2013-0017.
(70) Vaes, D.; Van Puyvelde, P. Semi-Crystalline Feedstock for Filament-Based 3D Printing of Polymers. *Prog. Polym. Sci.* **2021**, *118*, 101411. https://doi.org/10.1016/j.progpolymsci.2021.101411.
(71) Ngo, T. D.; Kashani, A.; Imbalzano, G.; Nguyen, K. T. Q.; Hui, D. Additive Manufacturing (3D Printing): A Review of Materials, Methods, Applications and Challenges. *Compos. Part B Eng.* **2018**, *143*, 172–196. https://doi.org/10.1016/j.compositesb.2018.02.012.
(72) Peterson, A. M. Review of Acrylonitrile Butadiene Styrene in Fused Filament Fabrication: A Plastics Engineering-Focused Perspective. *Addit. Manuf.* **2019**, *27*, 363–371. https://doi.org/10.1016/j.addma.2019.03.030.
(73) Wohlers TT, Campbell I, Diegel O, Huff R, Kowen J. Wohlers Report **2020**. Wohlers Associates, Inc; 2020.
(74) Rubinstein, M.; Colby, R. H. *Polymer Physics*; Oxford University Press: New York, **2003**.
(75) Gofman, I. V.; Yudin, V. E.; Orell, O.; Vuorinen, J.; Grigoriev, A. Ya.; Svetlichnyi, V. M. Influence of the Degree of Crystallinity on the Mechanical and Tribological Properties of High-Performance Thermoplastics Over a Wide Range of Temperatures: From Room Temperature up to 250°C. *J. Macromol. Sci. Part B* **2013**, *52* (12), 1848–1860. https://doi.org/10.1080/00222348.2013.808932.
(76) Mark, J. E. *Physical Properties of Polymers Handbook*; Springer: New York, **2007**.
(77) Piorkowska, E.; Rutledge, G. C. *Handbook of Polymer Crystallization*; John Wiley & Sons, Inc: Hoboken.
(78) Kutz, M. *Applied Plastics Engineering Handbook. Norwich*; William Andrew: Norwich, **2017**.
(79) Esposito Corcione, C.; Gervaso, F.; Scalera, F.; Padmanabhan, S. K.; Madaghiele, M.; Montagna, F.; Sannino, A.; Licciulli, A.; Maffezzoli, A. Highly Loaded Hydroxyapatite Microsphere/ PLA Porous Scaffolds Obtained by Fused Deposition Modelling. *Thermophys. Asp. Funct. Ceram. Surf.* **2019**, *45* (2, Part B), 2803–2810. https://doi.org/10.1016/j.ceramint.2018.07.297.
(80) Lee, J.; Lee, H.; Cheon, K.-H.; Park, C.; Jang, T.-S.; Kim, H.-E.; Jung, H.-D. Fabrication of Poly(Lactic Acid)/Ti Composite Scaffolds with Enhanced Mechanical Properties and Biocompatibility via Fused Filament Fabrication (FFF)–Based 3D Printing. *Addit. Manuf.* **2019**, *30*, 100883. https://doi.org/10.1016/j.addma.2019.100883.
(81) Ravi, P.; Shiakolas, P. S.; Welch, T. R. Poly-l-Lactic Acid: Pellets to Fiber to Fused Filament Fabricated Scaffolds, and Scaffold Weight Loss Study. *Addit. Manuf.* **2017**, *16*, 167–176. https://doi.org/10.1016/j.addma.2017.06.002.
(82) Senatov, F. S.; Niaza, K. V.; Zadorozhnyy, M. Yu.; Maksimkin, A. V.; Kaloshkin, S. D.; Estrin, Y. Z. Mechanical Properties and Shape Memory Effect of 3D-Printed PLA-Based Porous Scaffolds. *J. Mech. Behav. Biomed. Mater.* **2016**, *57*, 139–148. https://doi.org/10.1016/j.jmbbm.2015.11.036.
(83) Hutmacher, D.; Schantz, T.; Zein, I.; Ng, K.; Teoh, H.; Tan, K.-C. Mechanical Properties and Cell Cultural Response of Polycaprolactone Scaffolds Designed and Fabricated via Fused Deposition Modelling. *J. Biomed. Mater. Res.* **2001**, *55*, 203–216. https://doi.org/10.1002/1097-4636(200105)55:2<203::AID-JBM1007>3.0.CO;2-7.
(84) Patrício, T.; Domingos, M.; Gloria, A.; Bártolo, P. Characterisation of PCL and PCL/PLA Scaffolds for Tissue Engineering. *First CIRP Conf. BioManufacturing* **2013**, *5*, 110–114. https://doi.org/10.1016/j.procir.2013.01.022.
(85) Seyednejad, H.; Gawlitta, D.; Dhert, W. J. A.; van Nostrum, C. F.; Vermonden, T.;

Hennink, W. E. Preparation and Characterization of a Three-Dimensional Printed Scaffold Based on a Functionalized Polyester for Bone Tissue Engineering Applications. *Acta Biomater.* **2011**, *7* (5), 1999–2006. https://doi.org/10.1016/j.actbio.2011.01.018.
(86) Aho, J.; Bøtker, J. P.; Genina, N.; Edinger, M.; Arnfast, L.; Rantanen, J. Roadmap to 3D-Printed Oral Pharmaceutical Dosage Forms: Feedstock Filament Properties and Characterization for Fused Deposition Modeling. *J. Pharm. Sci.* **2019**, *108* (1), 26–35. https://doi.org/10.1016/j.xphs.2018.11.012.
(87) Holländer, J.; Genina, N.; Jukarainen, H.; Khajeheian, M.; Rosling, A.; Mäkilä, E.; Sandler, N. Three-Dimensional Printed PCL-Based Implantable Prototypes of Medical Devices for Controlled Drug Delivery. *J. Pharm. Sci.* **2016**, *105*. https://doi.org/10.1016/j.xphs.2015.12.012.
(88) Li, D.; Guo, G.; Fan, R.; Liang, J.; Deng, X.; Luo, F.; Qian, Z. PLA/F68/Dexamethasone Implants Prepared by Hot-Melt Extrusion for Controlled Release of Anti-Inflammatory Drug to Implantable Medical Devices: I. Preparation, Characterization and Hydrolytic Degradation Study. *Int. J. Pharm.* **2013**, *441* (1), 365–372. https://doi.org/10.1016/j.ijpharm.2012.11.019.
(89) Başgül, C.; Yu, T.; Macdonald, D.; Siskey, R.; Marcolongo, M.; Kurtz, S. Structure-Property Relationships for 3D Printed PEEK Intervertebral Lumbar Cages Produced Using Fused Filament Fabrication. *J. Mater. Res.* **2018**, *33*, 1–12. https://doi.org/10.1557/jmr.2018.178.
(90) Haleem, A.; Javaid, M. Polyether Ether Ketone (PEEK) and Its Manufacturing of Customised 3D Printed Dentistry Parts Using Additive Manufacturing. *Clin. Epidemiol. Glob. Health* **2019**, *7* (4), 654–660. https://doi.org/10.1016/j.cegh.2019.03.001.
(91) Berretta, S.; Evans, K.; Ghita, O. Additive Manufacture of PEEK Cranial Implants: Manufacturing Considerations versus Accuracy and Mechanical Performance. *Mater. Des.* **2018**, *139*, 141–152. https://doi.org/10.1016/j.matdes.2017.10.078.
(92) Katschnig, M.; Arbeiter, F.; Haar, B.; van Campe, G.; Holzer, C. Cranial Polypropylene Implants by Fused Filament Fabrication. *Adv. Eng. Mater.* **2017**, *19* (4), 1600676. https://doi.org/10.1002/adem.201600676.
(93) Daniel, F.; Patoary, N.; Moore, A.; Weiss, L.; Radadia, A. Temperature-Dependent Electrical Resistance of Conductive Polylactic Acid Filament for Fused Deposition Modeling. *Int. J. Adv. Manuf. Technol.* **2018**, *99*. https://doi.org/10.1007/s00170-018-2490-z.
(94) Leigh, S. J.; Bradley, R. J.; Purssell, C. P.; Billson, D. R.; Hutchins, D. A. A Simple, Low-Cost Conductive Composite Material for 3D Printing of Electronic Sensors. *PLOS ONE* **2012**, *7* (11), e49365. https://doi.org/10.1371/journal.pone.0049365.
(95) Kim, H.; Johnson, J.; Chavez, L. A.; Garcia Rosales, C. A.; Tseng, T.-L. B.; Lin, Y. Enhanced Dielectric Properties of Three Phase Dielectric MWCNTs/BaTiO3/PVDF Nanocomposites for Energy Storage Using Fused Deposition Modeling 3D Printing. *Ceram. Int.* **2018**, *44* (8), 9037–9044. https://doi.org/10.1016/j.ceramint.2018.02.107.
(96) Tichy, T.; Sefl, O.; Veselý, P.; Capal, T. *Application Possibilities of Fused Filament Fabrication Technology for High-Voltage and Medium-Voltage Insulation Systems*; **2019**; p 6. https://doi.org/10.1109/ISSE.2019.8810300.
(97) Klippstein, H.; Sanchez, A.; Hassanin, H.; Zweiri, Y.; Seneviratne, L. Fused Deposition Modeling for Unmanned Aerial Vehicles (UAVs): A Review. *Adv. Eng. Mater.* **2017**, *20*, 1700552. https://doi.org/10.1002/adem.201700552.
(98) Fink, J. K. *High Performance Polymers*; William Andrew: Norwich, 2008.
(99) Fallon, J. J.; McKnight, S. H.; Bortner, M. J. Highly Loaded Fiber Filled Polymers for Material Extrusion: A Review of Current Understanding. *Addit. Manuf.* **2019**, *30*, 100810. https://doi.org/10.1016/j.addma.2019.100810.
(100) Gao, X.; Zhang, D.; Qi, S.; Wen, X.; Su, Y. Mechanical Properties of 3D Parts

Fabricated by Fused Deposition Modeling: Effect of Various Fillers in Polylactide. *J. Appl. Polym. Sci.* **2019**, *136*, 47824. https://doi.org/10.1002/app.47824.
(101) Das, A.; Chatham, C. A.; Fallon, J. J.; Zawaski, C. E.; Gilmer, E. L.; Williams, C. B.; Bortner, M. J. Current Understanding and Challenges in High Temperature Additive Manufacturing of Engineering Thermoplastic Polymers. *Addit. Manuf.* **2020**, *34*, 101218. https://doi.org/10.1016/j.addma.2020.101218.
(102) Goh, G. D.; Yap, Y. L.; Tan, H. K. J.; Sing, S. L.; Goh, G. L.; Yeong, W. Y. Process–Structure–Properties in Polymer Additive Manufacturing via Material Extrusion: A Review. *Crit. Rev. Solid State Mater. Sci.* **2020**, *45* (2), 113–133. https://doi.org/10.1080/10408436.2018.1549977.
(103) Dizon, J. R. C.; Espera, A. H.; Chen, Q.; Advincula, R. C. Mechanical Characterization of 3D-Printed Polymers. *Addit. Manuf.* **2018**, *20*, 44–67. https://doi.org/10.1016/j.addma.2017.12.002.
(104) Wu, W.-G., PengAU-Li, GuiweiAU-Zhao, DiAU-Zhang, HaiboAU-Zhao, JiTI-Influence of Layer Thickness and Raster Angle on the Mechanical Properties of 3D-Printed PEEK and a Comparative Mechanical Study between PEEK and ABS. Influence of Layer Thickness and Raster Angle on the Mechanical Properties of 3d-Printed Peek and a Comparative Mechanical Study between PEEK and ABS. *Materials* **2015**, *8* (9), 5834–5846. https://doi.org/10.3390/ma8095271.
(105) Messimer, S. L. A.-R. P., TaisAU-Patterson, Albert E. AU-Lubna, MalihaAU-Drozda, Fabiano O. TI-Full-Density Fused Deposition Modeling Dimensional Error as a Function of Raster Angle and Build Orientation: Large Dataset for Eleven Materials. Full-Density Fused Deposition Modeling Dimensional Error as a Function of Raster Angle and Build Orientation: Large Dataset for Eleven Materials. *J. Manuf. Mater. Process.* **2019**, *3* (1). https://doi.org/10.3390/jmmp3010006.
(106) Li, H.; Zhang, S.; Yi, Z.; Li, J.; Sun, A.; Guo, J.; Xu, G. Bonding Quality and Fracture Analysis of Polyamide 12 Parts Fabricated by Fused Deposition Modeling. *Rapid Prototyp. J.* **2017**, *23* (6), 973–982. https://doi.org/10.1108/RPJ-03-2016-0033.
(107) Rezayat, H.; Zhou, W.; Siriruk, A.; Penumadu, D.; Babu, S. S. Structure–Mechanical Property Relationship in Fused Deposition Modelling. *Mater. Sci. Technol.* **2015**, *31* (8), 895–903. https://doi.org/10.1179/1743284715Y.0000000010.
(108) Kiendl, J.; Gao, C. Controlling Toughness and Strength of FDM 3D-Printed PLA Components through the Raster Layup. *Compos. Part B Eng.* **2020**, *180*, 107562. https://doi.org/10.1016/j.compositesb.2019.107562.
(109) Costa, A. E.; Ferreira da Silva, A.; Sousa Carneiro, O. A Study on Extruded Filament Bonding in Fused Filament Fabrication. *Rapid Prototyp. J.* **2019**, *25* (3), 555–565. https://doi.org/10.1108/RPJ-03-2018-0062.
(110) Torrado, A. R.; Shemelya, C. M.; English, J. D.; Lin, Y.; Wicker, R. B.; Roberson, D. A. Characterizing the Effect of Additives to ABS on the Mechanical Property Anisotropy of Specimens Fabricated by Material Extrusion 3D Printing. *Addit. Manuf.* **2015**, *6*, 16–29. https://doi.org/10.1016/j.addma.2015.02.001.
(111) Patadiya, N. H.; Dave, H. K.; Rajpurohit, S. R. Effect of Build Orientation on Mechanical Strength of FDM Printed PLA. In *Advances in Additive Manufacturing and Joining*; Shunmugam, M. S., Kanthababu, M., Eds.; Springer Singapore: Singapore, **2020**; pp 301–307.
(112) Uddin, M. S.; Sidek, M. F. R.; Faizal, M. A.; Ghomashchi, R.; Pramanik, A. Evaluating Mechanical Properties and Failure Mechanisms of Fused Deposition Modeling Acrylonitrile Butadiene Styrene Parts. *J. Manuf. Sci. Eng.* **2017**, *139* (8). https://doi.org/10.1115/1.4036713.
(113) Türk, D.-A.; Brenni, F.; Zogg, M.; Meboldt, M. Mechanical Characterization of 3D Printed Polymers for Fiber Reinforced Polymers Processing. *Mater. Des.* **2017**, *118*, 256–265.

https://doi.org/10.1016/j.matdes.2017.01.050.
(114) Maurel, A.; Courty, M.; Fleutot, B.; Tortajada, H.; Prashantha, K.; Armand, M.; Grugeon, S.; Panier, S.; Dupont, L. Highly Loaded Graphite–Polylactic Acid Composite-Based Filaments for Lithium-Ion Battery Three-Dimensional Printing. *Chem. Mater.* **2018**, *30* (21), 7484–7493. https://doi.org/10.1021/acs.chemmater.8b02062.
(115) Parandoush, P.; Lin, D. A Review on Additive Manufacturing of Polymer-Fiber Composites. *Compos. Struct.* **2017**, *182*, 36–53. https://doi.org/10.1016/j.compstruct.2017.08.088.
(116) Blok, L. G.; Longana, M. L.; Yu, H.; Woods, B. K. S. An Investigation into 3D Printing of Fibre Reinforced Thermoplastic Composites. *Addit. Manuf.* **2018**, *22*, 176–186. https://doi.org/10.1016/j.addma.2018.04.039.
(117) Brenken, B.; Barocio, E.; Favaloro, A.; Kunc, V.; Pipes, R. B. Fused Filament Fabrication of Fiber-Reinforced Polymers: A Review. *Addit. Manuf.* **2018**, *21*, 1–16. https://doi.org/10.1016/j.addma.2018.01.002.
(118) Love, L. J.; Kunc, V.; Rios, O.; Duty, C. E.; Elliott, A. M.; Post, B. K.; Smith, R. J.; Blue, C. A. The Importance of Carbon Fiber to Polymer Additive Manufacturing. *J. Mater. Res.* **2014**, *29* (17), 1893–1898. https://doi.org/10.1557/jmr.2014.212.
(119) Weng, Z.; Wang, J.; Senthil, T.; Wu, L. Mechanical and Thermal Properties of ABS/Montmorillonite Nanocomposites for Fused Deposition Modeling 3D Printing. *Mater. Des.* **2016**, *102*, 276–283. https://doi.org/10.1016/j.matdes.2016.04.045.
(120) Dawoud, M.; Taha, I.; Ebeid, S. J. Mechanical Behaviour of ABS: An Experimental Study Using FDM and Injection Moulding Techniques. *J. Manuf. Process.* **2016**, *21*, 39–45. https://doi.org/10.1016/j.jmapro.2015.11.002.
(121) Sun, Q.; Rizvi, G. M.; Bellehumeur, C. T.; Gu, P. Effect of Processing Conditions on the Bonding Quality of FDM Polymer Filaments. *Rapid Prototyp. J.* **2008**, *14* (2), 72–80. https://doi.org/10.1108/13552540810862028.
(122) Coogan, T. J.; Kazmer, D. O. Healing Simulation for Bond Strength Prediction of FDM. *Rapid Prototyp. J.* **2017**, *23* (3), 551–561. https://doi.org/10.1108/RPJ-03-2016-0051.
(123) Bellehumeur, C.; Li, L.; Sun, Q.; Gu, P. Modeling of Bond Formation Between Polymer Filaments in the Fused Deposition Modeling Process. *J. Manuf. Process.* **2004**, *6* (2), 170–178. https://doi.org/10.1016/S1526-6125(04)70071-7.
(124) Barocio, E.; Brenken, B.; Favaloro, A.; Bogdanor, M.; Pipes, R. B. Extrusion Deposition Additive Manufacturing with Fiber-Reinforced Thermoplastic Polymers. In *Structure and Properties of Additive Manufactured Polymer Components*; Friedrich, K., Walter, R., Soutis, C., Advani, S. G., Fiedler, Ing. Habil. B., Eds.; Woodhead Publishing, **2020**; pp 191–219. https://doi.org/10.1016/B978-0-12-819535-2.00007-7.
(125) Gao, X.; Qi, S.; Kuang, X.; Su, Y.; Li, J.; Wang, D. Fused Filament Fabrication of Polymer Materials: A Review of Interlayer Bond. *Addit. Manuf.* **2021**, *37*, 101658. https://doi.org/10.1016/j.addma.2020.101658.
(126) Yin, J.; Lu, C.; Fu, J.; Huang, Y.; Zheng, Y. Interfacial Bonding during Multi-Material Fused Deposition Modeling (FDM) Process Due to Inter-Molecular Diffusion. *Mater. Des.* **2018**, *150*, 104–112. https://doi.org/10.1016/j.matdes.2018.04.029.
(127) Yang, F.; Pitchumani, R. Healing of Thermoplastic Polymers at an Interface under Nonisothermal Conditions. *Macromolecules* **2002**, *35* (8), 3213–3224. https://doi.org/10.1021/ma010858o.
(128) Kousiatza, C.; Karalekas, D. In-Situ Monitoring of Strain and Temperature Distributions during Fused Deposition Modeling Process. *Mater. Des.* **2016**, *97*, 400–406. https://doi.org/10.1016/j.matdes.2016.02.099.
(129) Seppala, J. E.; Migler, K. D. Infrared Thermography of Welding Zones Produced by Polymer Extrusion Additive Manufacturing. *Addit. Manuf.* **2016**, *12*, 71–76.

https://doi.org/10.1016/j.addma.2016.06.007.
(130) Shmueli, Y.; Jiang, J.; Zhou, Y.; Xue, Y.; Chang, C.-C.; Yuan, G.; Satija, S. K.; Lee, S.; Nam, C.-Y.; Kim, T.; Marom, G.; Gersappe, D.; Rafailovich, M. H. Simultaneous in Situ X-Ray Scattering and Infrared Imaging of Polymer Extrusion in Additive Manufacturing. *ACS Appl. Polym. Mater.* **2019**, *1* (6), 1559–1567. https://doi.org/10.1021/acsapm.9b00328.
(131) Mackay, M. E. The Importance of Rheological Behavior in the Additive Manufacturing Technique Material Extrusion. *J. Rheol.* **2018**, *62* (6), 1549–1561. https://doi.org/10.1122/1.5037687.
(132) Northcutt, L. A.; Orski, S. V.; Migler, K. B.; Kotula, A. P. Effect of Processing Conditions on Crystallization Kinetics during Materials Extrusion Additive Manufacturing. *Polymer* **2018**, *154*, 182–187. https://doi.org/10.1016/j.polymer.2018.09.018.
(133) Serdeczny, M. P.; Comminal, R.; Pedersen, D. B.; Spangenberg, J. Numerical Simulations of the Mesostructure Formation in Material Extrusion Additive Manufacturing. *Addit. Manuf.* **2019**, *28*, 419–429. https://doi.org/10.1016/j.addma.2019.05.024.
(134) Garzon-Hernandez, S.; Garcia-Gonzalez, D.; Jérusalem, A.; Arias, A. Design of FDM 3D Printed Polymers: An Experimental-Modelling Methodology for the Prediction of Mechanical Properties. *Mater. Des.* **2020**, *188*, 108414. https://doi.org/10.1016/j.matdes.2019.108414.
(135) Coogan, T. J.; Kazmer, D. O. Modeling of Interlayer Contact and Contact Pressure during Fused Filament Fabrication. *J. Rheol.* **2019**, *63* (4), 655–672. https://doi.org/10.1122/1.5093033.
(136) Coasey, K.; Hart, K. R.; Wetzel, E.; Edwards, D.; Mackay, M. E. Nonisothermal Welding in Fused Filament Fabrication. *Addit. Manuf.* **2020**, *33*, 101140. https://doi.org/10.1016/j.addma.2020.101140.
(137) Pokluda, O.; Bellehumeur, C. T.; Vlachopoulos, J. Modification of Frenkel's Model for Sintering. *AIChE J.* **1997**, *43* (12), 3253–3256. https://doi.org/10.1002/aic.690431213.
(138) Kamyabi, M.; Sotudeh-Gharebagh, R.; Zarghami, R.; Saleh, K. Principles of Viscous Sintering in Amorphous Powders: A Critical Review. *Chem. Eng. Res. Des.* **2017**, *125*, 328–347. https://doi.org/10.1016/j.cherd.2017.06.009.
(139) Seppala, J. E.; Hoon Han, S.; Hillgartner, K. E.; Davis, C. S.; Migler, K. B. Weld Formation during Material Extrusion Additive Manufacturing. *Soft Matter* **2017**, *13* (38), 6761–6769. https://doi.org/10.1039/C7SM00950J.
(140) Bhalodi, D.; Zalavadiya, K.; Gurrala, P. K. Influence of Temperature on Polymer Parts Manufactured by Fused Deposition Modeling Process. *J. Braz. Soc. Mech. Sci. Eng.* **2019**, *41* (3), 113. https://doi.org/10.1007/s40430-019-1616-z.
(141) Polychronopoulos, N. D.; Vlachopoulos, J. The Role of Heating and Cooling in Viscous Sintering of Pairs of Spheres and Pairs of Cylinders. *Rapid Prototyp. J.* **2020**, *26* (4), 719–726. https://doi.org/10.1108/RPJ-06-2019-0162.
(142) Gurrala, P. K.; Regalla, S. P. Part Strength Evolution with Bonding between Filaments in Fused Deposition Modelling. *Virtual Phys. Prototyp.* **2014**, *9* (3), 141–149. https://doi.org/10.1080/17452759.2014.913400.
(143) Bellehumeur, C. T.; Bisaria, M. K.; Vlachopoulos, J. An Experimental Study and Model Assessment of Polymer Sintering. *Polym. Eng. Sci.* **1996**, *36* (17), 2198–2207. https://doi.org/10.1002/pen.10617.
(144) Liu, S.-J. Sintering Rheology of Semi-Crystalline Polymers. **1998**, *13* (1), 88–90. https://doi.org/10.3139/217.980088.
(145) Shahriar, B. B.; France, C.; Valerie, N.; Arthur, C.; Christian, G. Toward Improvement of the Properties of Parts Manufactured by FFF (Fused Filament Fabrication) through Understanding the Influence of Temperature and Rheological Behaviour on the Coalescence Phenomenon. *AIP Conf. Proc.* **2017**, *1896* (1), 040008. https://doi.org/10.1063/1.5008034.

(146) Srinivas, V.; van Hooy-Corstjens, C. S. J.; Harings, J. A. W. Correlating Molecular and Crystallization Dynamics to Macroscopic Fusion and Thermodynamic Stability in Fused Deposition Modeling; a Model Study on Polylactides. *Polymer* **2018**, *142*, 348–355. https://doi.org/10.1016/j.polymer.2018.03.063.
(147) Wool, R. P.; O'Connor, K. M. A Theory Crack Healing in Polymers. *J. Appl. Phys.* **1981**, *52* (10), 5953–5963. https://doi.org/10.1063/1.328526.
(148) Coogan, T. J.; Kazmer, D. O. Prediction of Interlayer Strength in Material Extrusion Additive Manufacturing. *Addit. Manuf.* **2020**, *35*, 101368. https://doi.org/10.1016/j.addma.2020.101368.
(149) Sha, Y.; Hui, C. Y.; Ruina, A.; Kramer, E. J. Continuum and Discrete Modeling of Craze Failure at a Crack Tip in a Glassy Polymer. *Macromolecules* **1995**, *28* (7), 2450–2459. https://doi.org/10.1021/ma00111a044.
(150) Xue, Y.-Q.; Tervoort, T. A.; Lemstra, P. J. Welding Behavior of Semicrystalline Polymers. 1. The Effect of Nonequilibrium Chain Conformations on Autoadhesion of UHMWPE. *Macromolecules* **1998**, *31* (9), 3075–3080. https://doi.org/10.1021/ma970544u.
(151) Xue, Y.-Q.; Tervoort, T. A.; Rastogi, S.; Lemstra, J. Welding Behavior of Semicrystalline Polymers. 2. Effect of Cocrystallization on Autoadhesion. *Macromolecules* **2000**, *33* (19), 7084–7087. https://doi.org/10.1021/ma000754y.
(152) McIlroy, C.; Graham, R. S. Modelling Flow-Enhanced Crystallisation during Fused Filament Fabrication of Semi-Crystalline Polymer Melts. *Addit. Manuf.* **2018**, *24*, 323–340. https://doi.org/10.1016/j.addma.2018.10.018.
(153) Nogales, A.; Gutiérrez-Fernández, E.; García-Gutiérrez, M.-C.; Ezquerra, T. A.; Rebollar, E.; Šics, I.; Malfois, M.; Gaidukovs, S.; Gēcis, E.; Celms, K.; Bakradze, G. Structure Development in Polymers during Fused Filament Fabrication (FFF): An in Situ Small- and Wide-Angle X-Ray Scattering Study Using Synchrotron Radiation. *Macromolecules* **2019**, *52* (24), 9715–9723. https://doi.org/10.1021/acs.macromol.9b01620.
(154) McIlroy, C.; Seppala, J. E.; Kotula, A. P. Combining Modeling and Measurements To Predict Crystal Morphology in Material Extrusion. In *Polymer-Based Additive Manufacturing: Recent Developments*; ACS Symposium Series; American Chemical Society, 2019; Vol. 1315, pp 85–113. https://doi.org/10.1021/bk-2019-1315.ch006.
(155) Abbott, A. C.; Tandon, G. P.; Bradford, R. L.; Koerner, H.; Baur, J. W. Process-Structure-Property Effects on ABS Bond Strength in Fused Filament Fabrication. *Addit. Manuf.* **2018**, *19*, 29–38. https://doi.org/10.1016/j.addma.2017.11.002.
(156) Levenhagen, N. P.; Dadmun, M. D. Bimodal Molecular Weight Samples Improve the Isotropy of 3D Printed Polymeric Samples. *Polymer* **2017**, *122*, 232–241. https://doi.org/10.1016/j.polymer.2017.06.057.
(157) Levenhagen, N. P.; Dadmun, M. D. Interlayer Diffusion of Surface Segregating Additives to Improve the Isotropy of Fused Deposition Modeling Products. *SI Adv. Polym. 3DPrintingAdditive Manuf.* **2018**, *152*, 35–41. https://doi.org/10.1016/j.polymer.2018.01.031.
(158) Wang, L.; Gramlich, W. M.; Gardner, D. J. Improving the Impact Strength of Poly(Lactic Acid) (PLA) in Fused Layer Modeling (FLM). *Polymer* **2017**, *114*, 242–248. https://doi.org/10.1016/j.polymer.2017.03.011.
(159) Cole, D. P.; Riddick, J. C.; Iftekhar Jaim, H. M.; Strawhecker, K. E.; Zander, N. E. Interfacial Mechanical Behavior of 3D Printed ABS. *J. Appl. Polym. Sci.* **2016**, *133* (30). https://doi.org/10.1002/app.43671.
(160) Ravi, A. K.; Deshpande, A.; Hsu, K. H. An In-Process Laser Localized Pre-Deposition Heating Approach to Inter-Layer Bond Strengthening in Extrusion Based Polymer Additive Manufacturing. *J. Manuf. Process.* **2016**, *24*, 179–185. https://doi.org/10.1016/j.jmapro.2016.08.007.
(161) Spoerk, M.; Savandaiah, C.; Arbeiter, F.; Traxler, G.; Cardon, L.; Holzer, C.; Sapkota,

J. Anisotropic Properties of Oriented Short Carbon Fibre Filled Polypropylene Parts Fabricated by Extrusion-Based Additive Manufacturing. *Compos. Part Appl. Sci. Manuf.* **2018**, *113*, 95–104. https://doi.org/10.1016/j.compositesa.2018.06.018.
(162) Striemann, P.-H., DanielAU-Niedermeier, MichaelAU-Walther, FrankTI-Optimization and Quality Evaluation of the Interlayer Bonding Performance of Additively Manufactured Polymer Structures. Optimization and Quality Evaluation of the Interlayer Bonding Performance of Additively Manufactured Polymer Structures. *Polymers* **2020**, *12* (5). https://doi.org/10.3390/polym12051166.
(163) Khudiakova, A.; Arbeiter, F.; Spoerk, M.; Wolfahrt, M.; Godec, D.; Pinter, G. Inter-Layer Bonding Characterisation between Materials with Different Degrees of Stiffness Processed by Fused Filament Fabrication. *Addit. Manuf.* **2019**, *28*, 184–193. https://doi.org/10.1016/j.addma.2019.05.006.
(164) Aliheidari, N.; Christ, J.; Tripuraneni, R.; Nadimpalli, S.; Ameli, A. Interlayer Adhesion and Fracture Resistance of Polymers Printed through Melt Extrusion Additive Manufacturing Process. *Mater. Des.* **2018**, *156*, 351–361. https://doi.org/10.1016/j.matdes.2018.07.001.
(165) Young, D. J.; Otten, C.; Czabaj, M. W. Effect of Processing Parameters on Interlayer Fracture Toughness of Fused Filament Fabrication Thermoplastic Materials. In *Mechanics of Additive and Advanced Manufacturing, Volume 8*; Kramer, S., Jordan, J. L., Jin, H., Carroll, J., Beese, A. M., Eds.; Springer International Publishing: Cham, **2019**; pp 77–79.
(166) Kishore, V.; Ajinjeru, C.; Nycz, A.; Post, B.; Lindahl, J.; Kunc, V.; Duty, C. Infrared Preheating to Improve Interlayer Strength of Big Area Additive Manufacturing (BAAM) Components. *Addit. Manuf.* **2017**, *14*, 7–12. https://doi.org/10.1016/j.addma.2016.11.008.
(167) Davis, C. S.; Hillgartner, K. E.; Han, S. H.; Seppala, J. E. Mechanical Strength of Welding Zones Produced by Polymer Extrusion Additive Manufacturing. *Addit. Manuf.* **2017**, *16*, 162–166. https://doi.org/10.1016/j.addma.2017.06.006.
(168) Tofangchi, A.-H., PuAU-Izquierdo, JulioAU-Iyengar, AdithyaAU-Hsu, KengTI-Effect of Ultrasonic Vibration on Interlayer Adhesion in Fused Filament Fabrication 3D Printed ABS. Effect of Ultrasonic Vibration on Interlayer Adhesion in Fused Filament Fabrication 3D Printed ABS. *Polymers* **2019**, *11* (2). https://doi.org/10.3390/polym11020315.
(169) Comminal, R.; Serdeczny, M. P.; Pedersen, D. B.; Spangenberg, J. Numerical Modeling of the Strand Deposition Flow in Extrusion-Based Additive Manufacturing. *Addit. Manuf.* **2018**, *20*, 68–76. https://doi.org/10.1016/j.addma.2017.12.013.
(170) Gao, X.; Qi, S.; Zhang, D.; Su, Y.; Wang, D. The Role of Poly (Ethylene Glycol) on Crystallization, Interlayer Bond and Mechanical Performance of Polylactide Parts Fabricated by Fused Filament Fabrication. *Addit. Manuf.* **2020**, *35*, 101414. https://doi.org/10.1016/j.addma.2020.101414.
(171) Bhandari, S.; Lopez-Anido, R. A.; Gardner, D. J. Enhancing the Interlayer Tensile Strength of 3D Printed Short Carbon Fiber Reinforced PETG and PLA Composites via Annealing. *Addit. Manuf.* **2019**, *30*, 100922. https://doi.org/10.1016/j.addma.2019.100922.
(172) Gao, X.; Zhang, D.; Wen, X.; Qi, S.; Su, Y.; Dong, X. Fused Deposition Modeling with Polyamide 1012. *Rapid Prototyp. J.* **2019**, *25* (7), 1145–1154. https://doi.org/10.1108/RPJ-09-2018-0258.
(173) Hertle, S.; Drexler, M.; Drummer, D. Additive Manufacturing of Poly(Propylene) by Means of Melt Extrusion. *Macromol. Mater. Eng.* **2016**, *301* (12), 1482–1493. https://doi.org/10.1002/mame.201600259.
(174) Spoerk, M.; Holzer, C.; Gonzalez-Gutierrez, J. Material Extrusion-Based Additive Manufacturing of Polypropylene: A Review on How to Improve Dimensional Inaccuracy and Warpage. *J. Appl. Polym. Sci.* **2020**, *137* (12), 48545. https://doi.org/10.1002/app.48545.
(175) Spoerk, M.; Arbeiter, F.; Raguž, I.; Weingrill, G.; Fischinger, T.; Traxler, G.;

Schuschnigg, S.; Cardon, L.; Holzer, C. Polypropylene Filled With Glass Spheres in Extrusion-Based Additive Manufacturing: Effect of Filler Size and Printing Chamber Temperature. *Macromol. Mater. Eng.* **2018**, *303* (7), 1800179. https://doi.org/10.1002/mame.201800179.
(176) Sood, A. K.; Ohdar, R. K.; Mahapatra, S. S. Parametric Appraisal of Mechanical Property of Fused Deposition Modelling Processed Parts. *Mater. Des.* **2010**, *31* (1), 287–295. https://doi.org/10.1016/j.matdes.2009.06.016.
(177) Valerga Puerta, A. P.; Fernandez-Vidal, S. R.; Batista, M.; Girot, F. Fused Deposition Modelling Interfacial and Interlayer Bonding in PLA Post-Processed Parts. *Rapid Prototyp. J.* **2020**, *26* (3), 585–592. https://doi.org/10.1108/RPJ-06-2019-0176.
(178) Compton, B. G.; Post, B. K.; Duty, C. E.; Love, L.; Kunc, V. Thermal Analysis of Additive Manufacturing of Large-Scale Thermoplastic Polymer Composites. *Addit. Manuf.* **2017**, *17*, 77–86. https://doi.org/10.1016/j.addma.2017.07.006.
(179) D'Amico, A. A.; Debaie, A.; Peterson, A. M. Effect of Layer Thickness on Irreversible Thermal Expansion and Interlayer Strength in Fused Deposition Modeling. *Rapid Prototyp. J.* **2017**, *23* (5), 943–953. https://doi.org/10.1108/RPJ-05-2016-0077.
(180) Deshpande, A.; Ravi, A.; Kusel, S.; Churchwell, R.; Hsu, K. Interlayer Thermal History Modification for Interface Strength in Fused Filament Fabricated Parts. *Prog. Addit. Manuf.* **2019**, *4* (1), 63–70. https://doi.org/10.1007/s40964-018-0063-1.
(181) Du, J.; Wei, Z.; Wang, X.; Wang, J.; Chen, Z. An Improved Fused Deposition Modeling Process for Forming Large-Size Thin-Walled Parts. *J. Mater. Process. Technol.* **2016**, *234*, 332–341. https://doi.org/10.1016/j.jmatprotec.2016.04.005.
(182) Papon, E. A.; Haque, A.; Spear, S. K. Effects of Functionalization and Annealing in Enhancing the Interfacial Bonding and Mechanical Properties of 3D Printed Fiber-Reinforced Composites. *Mater. Today Commun.* **2020**, *25*, 101365. https://doi.org/10.1016/j.mtcomm.2020.101365.
(183) Dong, J.; Mei, C.; Han, J.; Lee, S.; Wu, Q. 3D Printed Poly(Lactic Acid) Composites with Grafted Cellulose Nanofibers: Effect of Nanofiber and Post-Fabrication Annealing Treatment on Composite Flexural Properties. *Addit. Manuf.* **2019**, *28*, 621–628. https://doi.org/10.1016/j.addma.2019.06.004.
(184) Wach, R. A.; Wolszczak, P.; Adamus-Wlodarczyk, A. Enhancement of Mechanical Properties of FDM-PLA Parts via Thermal Annealing. *Macromol. Mater. Eng.* **2018**, *303* (9), 1800169. https://doi.org/10.1002/mame.201800169.
(185) Fitzharris, E. R.; Watt, I.; Rosen, D. W.; Shofner, M. L. Interlayer Bonding Improvement of Material Extrusion Parts with Polyphenylene Sulfide Using the Taguchi Method. *Addit. Manuf.* **2018**, *24*, 287–297. https://doi.org/10.1016/j.addma.2018.10.003.
(186) Sweeney, C. B.; Lackey, B. A.; Pospisil, M. J.; Achee, T. C.; Hicks, V. K.; Moran, A. G.; Teipel, B. R.; Saed, M. A.; Green, M. J. Welding of 3D-Printed Carbon Nanotube–Polymer Composites by Locally Induced Microwave Heating. *Sci. Adv. 3* (6), e1700262. https://doi.org/10.1126/sciadv.1700262.
(187) Davidson, J. R.; Appuhamillage, G. A.; Thompson, C. M.; Voit, W.; Smaldone, R. A. Design Paradigm Utilizing Reversible Diels–Alder Reactions to Enhance the Mechanical Properties of 3D Printed Materials. *ACS Appl. Mater. Interfaces* **2016**, *8* (26), 16961–16966. https://doi.org/10.1021/acsami.6b05118.
(188) Shaffer, S.; Yang, K.; Vargas, J.; Di Prima, M. A.; Voit, W. On Reducing Anisotropy in 3D Printed Polymers via Ionizing Radiation. *Shape Mem. Shape Morphing Polym.* **2014**, *55* (23), 5969–5979. https://doi.org/10.1016/j.polymer.2014.07.054.
(189) Portale, G.; Cavallo, D.; Alfonso, G. C.; Hermida Merino, D.; van Drongelen, M.; Balzano, L.; Peters, G.; Goossens, J. G. P.; Bras, W. Polymer Crystallization Studies under Processing-Relevant Conditions at the SAXS/WAXS DUBBLE Beamline at the ESRF. *J. Appl. Crystallogr.* **2013**, *46*. https://doi.org/10.1107/S0021889813027076.

(190) van Drongelen, M.; Cavallo, D.; Balzano, L.; Portale, G.; Vittorias, I.; Bras, W.; Alfonso, G. C.; Peters, G. W. M. Structure Development of Low-Density Polyethylenes During Film Blowing: A Real-Time Wide-Angle X-Ray Diffraction Study. *Macromol. Mater. Eng.* **2014**, *299* (12), 1494–1512. https://doi.org/10.1002/mame.201400161.
(191) Zhao, H.; Zhang, Q.; Xia, Z.; Yang, E.; Zhang, M.; Wang, Y.; Ji, Y.; Chen, W.; Wang, D.; Meng, L.; Li, L. Elucidation of the Relationships of Structure-Process-Property for Different Ethylene/α-Olefin Copolymers during Film Blowing: An in-Situ Synchrotron Radiation X-Ray Scattering Study. *Polym. Test.* **2020**, *85*, 106439. https://doi.org/10.1016/j.polymertesting.2020.106439.
(192) Heeley, E. L.; Gough, T.; Hughes, D. J.; Bras, W.; Rieger, J.; Ryan, A. J. Effect of Processing Parameters on the Morphology Development during Extrusion of Polyethylene Tape: An in-Line Small-Angle X-Ray Scattering (SAXS) Study. *Polymer* **2013**, *54* (24), 6580–6588. https://doi.org/10.1016/j.polymer.2013.10.004.
(193) Schultz, J. M.; Hsiao, B. S.; Samon, J. M. Structural Development during the Early Stages of Polymer Melt Spinning by In-Situ Synchrotron X-Ray Techniques. *Polymer* **2000**, *41* (25), 8887–8895. https://doi.org/10.1016/S0032-3861(00)00232-9.
(194) Lamberti, G.; De Santis, F.; Brucato, V.; Titomanlio, G. Modeling the Interactions between Light and Crystallizing Polymer during Fast Cooling. *Appl. Phys. A* **2004**, *78* (6), 895–901. https://doi.org/10.1007/s00339-003-2086-8.
(195) F. De Santis; M. Ferrara; H. . -C. Neitzert. Optical in Situ Characterization of Isotactic Polypropylene Crystallization Using an LED Array in Avalanche-Photoreceiver Mode. *IEEE Trans. Instrum. Meas.* **2006**, *55* (1), 123–127. https://doi.org/10.1109/TIM.2005.861501.
(196) Shimizu, J.; Kikutani, T. Dynamics and Evolution of Structure in Fiber Extrusion. *J. Appl. Polym. Sci.* **2002**, *83* (3), 539–558. https://doi.org/10.1002/app.2257.
(197) Fernandez-Ballester, L.; Gough, T.; Meneau, F.; Bras, W.; Ania, F.; Balta-Calleja, F. J.; Kornfield, J. A. Simultaneous Birefringence, Small- and Wide-Angle X-Ray Scattering to Detect Precursors and Characterize Morphology Development during Flow-Induced Crystallization of Polymers. *J. Synchrotron Radiat.* **2008**, *15* (2), 185–190. https://doi.org/10.1107/S0909049508002598.
(198) Xie, S.; Sun, Z.; Liu, T.; Zhang, J.; Li, T.; Ouyang, X.; Qiu, X.; Luo, S.; Fan, W.; Lin, H. Beyond Biodegradation: Chemical Upcycling of Poly(Lactic Acid) Plastic Waste to Methyl Lactate Catalyzed by Quaternary Ammonium Fluoride. *J. Catal.* **2021**, *402*, 61–71. https://doi.org/10.1016/j.jcat.2021.08.032.
(199) Gazzotti, S.; Adolfsson, K. H.; Hakkarainen, M.; Farina, H.; Silvani, A.; Ortenzi, M. A. DOX Mediated Synthesis of PLA-Co-PS Graft Copolymers with Matrix-Driven Self-Assembly in PLA-Based Blends. *Eur. Polym. J.* **2022**, *170*, 111157. https://doi.org/10.1016/j.eurpolymj.2022.111157.
(200) DSM Develops New 3D Printing Materials. *Reinf. Plast.* **2019**, *63*, 15.
(201) Duis, P. Major Improvements in Materials and FEA Software Bring Reality of High-Volume 3D Printing of Functional Parts Much Closer. *Reinf. Plast.* **2020**, *64* (2), 80–83. https://doi.org/10.1016/j.repl.2019.04.067.
(202) Cheng, G. Z.; San Jose Estepar, R.; Folch, E.; Onieva, J.; Gangadharan, S.; Majid, A. Three-Dimensional Printing and 3D Slicer: Powerful Tools in Understanding and Treating Structural Lung Disease. *Chest* **2016**, *149* (5), 1136–1142. https://doi.org/10.1016/j.chest.2016.03.001.
(203) Looijmans, S. F. S. P.; Carmeli, E.; Puskar, L.; Ellis, G.; Cavallo, D.; Anderson, P. D.; van Breemen, L. C. A. Polarization Modulated Infrared Spectroscopy: A Pragmatic Tool for Polymer Science and Engineering. *Polym. Cryst.* **2020**, *3* (6), e10138. https://doi.org/10.1002/pcr2.10138.
(204) Schmidt, M.; Schade, U.; Grunze, M. Microspectroscopic Observation of Vibrational

Linear Dichroism Using Polarization-Modulated Infrared Synchrotron Radiation. *Int. Workshop Infrared Microsc. Spectrosc. Accel.-Based Sources* **2006**, *49* (1), 69–73. https://doi.org/10.1016/j.infrared.2006.01.005.
(205) Seppala, J. E.; Kotula, A. P.; Snyder, C. R. *Polymer-Based Additive Manufacturing: Recent Developments*; ACS Symposium Series; American Chemical Society: Washington DC, **2019**.
(206) Likhtman, A. E.; Graham, R. S. Simple Constitutive Equation for Linear Polymer Melts Derived from Molecular Theory: Rolie–Poly Equation. *J. Non-Newton. Fluid Mech.* **2003**, *114* (1), 1–12. https://doi.org/10.1016/S0377-0257(03)00114-9.
(207) Doi, M.; Edwards, S. F.; Edwards, S. F. *The Theory of Polymer Dynamics*; oxford university press, **1988**; Vol. 73.
(208) Baig, C.; Mavrantzas, V. G.; Kröger, M. Flow Effects on Melt Structure and Entanglement Network of Linear Polymers: Results from a Nonequilibrium Molecular Dynamics Simulation Study of a Polyethylene Melt in Steady Shear. *Macromolecules* **2010**, *43* (16), 6886–6902. https://doi.org/10.1021/ma100826u.
(209) *Web Address:, Https.//Www.Makeitfrom.Com/Material-Properties/Polylactic-Acid-PLA- Polylactide, **2019**.*
(210) Das, A.; Gilmer, E. L.; Biria, S.; Bortner, M. J. Importance of Polymer Rheology on Material Extrusion Additive Manufacturing: Correlating Process Physics to Print Properties. *ACS Appl. Polym. Mater.* **2021**, *3* (3), 1218–1249. https://doi.org/10.1021/acsapm.0c01228.
(211) Likhtman, A. E.; McLeish, T. C. B. Quantitative Theory for Linear Dynamics of Linear Entangled Polymers. *Macromolecules* **2002**, *35* (16), 6332–6343. https://doi.org/10.1021/ma0200219.
(212) *RepTate documentation. Available online: https://reptate.readthedocs.io/*. https://reptate.readthedocs.io/.
(213) Dorgan, J. R.; Williams, J. S.; Lewis, D. N. Melt Rheology of Poly(Lactic Acid): Entanglement and Chain Architecture Effects. *J. Rheol.* **1999**, *43* (5), 1141–1155. https://doi.org/10.1122/1.551041.
(214) Lamberti, G.; Titomanlio, G.; Brucato, V. Measurement and Modelling of the Film Casting Process 1. Width Distribution along Draw Direction. *Chem. Eng. Sci.* **2001**, *56* (20), 5749–5761. https://doi.org/10.1016/S0009-2509(01)00286-X.
(215) Mulligan, J.; Cakmak, M. Nonlinear Mechanooptical Behavior of Uniaxially Stretched Poly(Lactic Acid): Dynamic Phase Behavior. *Macromolecules* **2005**, *38* (6), 2333–2344. https://doi.org/10.1021/ma048794f.
(216) Ou, X. *Structural Mechanisms as Revealed by Real Time Mechano Optical Behavior of Polylactic Acid Films in Uni and Biaxial Deformation and Heat Setting Processes*; The University of Akron, **2004**.
(217) Torres, J.; Cotelo, J.; Karl, J.; Gordon, A. P. Mechanical Property Optimization of FDM PLA in Shear with Multiple Objectives. *JOM* **2015**, *67* (5), 1183–1193. https://doi.org/10.1007/s11837-015-1367-y.
(218) Ge, T.; Pierce, F.; Perahia, D.; Grest, G. S.; Robbins, M. O. Molecular Dynamics Simulations of Polymer Welding: Strength from Interfacial Entanglements. *Phys. Rev. Lett.* **2013**, *110* (9), 098301. https://doi.org/10.1103/PhysRevLett.110.098301.
(219) Kausch, H.-H. Polymers/Properties and Applications. Vol.2. Polymer Fracture. *Polym. Appl.* **1987**, *2*.
(220) Kramer, E. J.; Green, P.; Palmstrøm, C. J. Interdiffusion and Marker Movements in Concentrated Polymer-Polymer Diffusion Couples. *Polymer* **1984**, *25* (4), 473–480. https://doi.org/10.1016/0032-3861(84)90205-2.
(221) Brown, H. R. A Molecular Interpretation of the Toughness of Glassy Polymers. *Macromolecules* **1991**, *24* (10), 2752–2756. https://doi.org/10.1021/ma00010a018.

(222) Nofar, M.; Salehiyan, R.; Sinha Ray, S. Rheology of Poly (Lactic Acid)-Based Systems. *Polym. Rev.* **2019**, *59* (3), 465–509. https://doi.org/10.1080/15583724.2019.1572185.
(223) Dorgan, J. R.; Janzen, J.; Clayton, M. P.; Hait, S. B.; Knauss, D. M. Melt Rheology of Variable L-Content Poly(Lactic Acid). *J. Rheol.* **2005**, *49* (3), 607–619. https://doi.org/10.1122/1.1896957.
(224) Cooper-White, J. J.; Mackay, M. E. Rheological Properties of Poly(Lactides). Effect of Molecular Weight and Temperature on the Viscoelasticity of Poly(l-Lactic Acid). *J. Polym. Sci. Part B Polym. Phys.* **1999**, *37* (15), 1803–1814. https://doi.org/10.1002/(SICI)1099-0488(19990801)37:15<1803::AID-POLB5>3.0.CO;2-M.
(225) Martin, J. R.; Johnson, J. F.; Cooper, A. R. Mechanical Properties of Polymers: The Influence of Molecular Weight and Molecular Weight Distribution. *J. Macromol. Sci. Part C* **1972**, *8* (1), 57–199. https://doi.org/10.1080/15321797208068169.
(226) Bersted, B. H.; Anderson, T. G. Influence of Molecular Weight and Molecular Weight Distribution on the Tensile Properties of Amorphous Polymers. *J. Appl. Polym. Sci.* **1990**, *39* (3), 499–514. https://doi.org/10.1002/app.1990.070390302.
(227) Kister, G.; Cassanas, G.; Vert, M.; Pauvert, B.; Térol, A. Vibrational Analysis of Poly(L-Lactic Acid). *J. Raman Spectrosc.* **1995**, *26* (4), 307–311. https://doi.org/10.1002/jrs.1250260409.
(228) Srinivas, V.; van Hooy-Corstjens, C. S. J.; Rastogi, S.; Harings, J. A. W. Promotion of Molecular Diffusion and/or Crystallization in Fused Deposition Modeled Poly(Lactide) Welds. *Polymer* **2020**, *202*, 122637. https://doi.org/10.1016/j.polymer.2020.122637.
(229) Hart, K. R.; Dunn, R. M.; Wetzel, E. D. Increased Fracture Toughness of Additively Manufactured Semi-Crystalline Thermoplastics via Thermal Annealing. *Polymer* **2020**, *211*, 123091. https://doi.org/10.1016/j.polymer.2020.123091.
(230) Kruse, M.; Rolón-Garrido, V. H.; Wagner, M. H. Rheological Characterization of Degradation and Polycondensation of Poly(Ethylene Terephthalate) Melt in Air and in Nitrogen. *AIP Conf. Proc.* **2013**, *1526* (1), 216–229. https://doi.org/10.1063/1.4802616.
(231) Liu, J.; Ye, L.; Zhao, X. Preparation of Long-Chain Branched Poly(Ethylene Terephthalate): Molecular Entanglement Structure and Toughening Mechanism. *Polym. Eng. Sci.* **2019**, *59* (6), 1190–1198. https://doi.org/10.1002/pen.25099.
(232) McKee, M. G.; Wilkes, G. L.; Colby, Ralph. H.; Long, T. E. Correlations of Solution Rheology with Electrospun Fiber Formation of Linear and Branched Polyesters. *Macromolecules* **2004**, *37* (5), 1760–1767. https://doi.org/10.1021/ma035689h.
(233) Kabanemi, K. K.; Hétu, J.-F. Nonequilibrium Stretching Dynamics of Dilute and Entangled Linear Polymers in Extensional Flow. *J. Non-Newton. Fluid Mech.* **2009**, *160* (2), 113–121. https://doi.org/10.1016/j.jnnfm.2009.03.006.
(234) Bartolai, J.; Simpson, T. W.; Xie, R. Predicting Strength of Additively Manufactured Thermoplastic Polymer Parts Produced Using Material Extrusion. *Rapid Prototyp. J.* **2018**, *24* (2), 321–332. https://doi.org/10.1108/RPJ-02-2017-0026.
(235) Https://Polymerdatabase.Com/Polymer%20physics/C%20Table2%20.Html.
(236) Lorenzo, A. T.; Arnal, M. L.; Albuerne, J.; Müller, A. J. DSC Isothermal Polymer Crystallization Kinetics Measurements and the Use of the Avrami Equation to Fit the Data: Guidelines to Avoid Common Problems. *Polym. Test.* **2007**, *26* (2), 222–231. https://doi.org/10.1016/j.polymertesting.2006.10.005.
(237) Rhoades, A. M.; Williams, J. L.; Androsch, R. Crystallization Kinetics of Polyamide 66 at Processing-Relevant Cooling Conditions and High Supercooling. *Chip Calorim.* **2015**, *603*, 103–109. https://doi.org/10.1016/j.tca.2014.10.020.
(238) Cavallo, D.; Gardella, L.; Alfonso, G. C.; Portale, G.; Balzano, L.; Androsch, R. Effect of Cooling Rate on the Crystal/Mesophase Polymorphism of Polyamide 6. *Colloid Polym. Sci.* **2011**, *289* (9), 1073–1079. https://doi.org/10.1007/s00396-011-2428-6.

(239) Zhang, X.; Wang, J. Controllable Interfacial Adhesion Behaviors of Polymer-on-Polymer Surfaces during Fused Deposition Modeling 3D Printing Process. *Chem. Phys. Lett.* **2020**, *739*, 136959. https://doi.org/10.1016/j.cplett.2019.136959.
(240) Cruz, P.; Shoemake, E. D.; Adam, P.; Leachman, J. Tensile Strengths of Polyamide Based 3D Printed Polymers in Liquid Nitrogen. *IOP Conf. Ser. Mater. Sci. Eng.* **2015**, *102*, 012020. https://doi.org/10.1088/1757-899x/102/1/012020.
(241) Ghodbane, S. A.; Murthy, N. S.; Dunn, M. G.; Kohn, J. Achieving Molecular Orientation in Thermally Extruded 3D Printed Objects. *Biofabrication* **2019**, *11* (4), 045004. https://doi.org/10.1088/1758-5090/ab1d44.
(242) Vaes, D.; Coppens, M.; Goderis, B.; Zoetelief, W.; Van Puyvelde, P. The Extent of Interlayer Bond Strength during Fused Filament Fabrication of Nylon Copolymers: An Interplay between Thermal History and Crystalline Morphology. *Polymers* **2021**, *13* (16). https://doi.org/10.3390/polym13162677.
(243) Petersmann, S.; Erdely, P.; Feuchter, M.; Wieme, T.; Arbeiter, F.; Spoerk, M. Process-Induced Morphological Features in Material Extrusion-Based Additive Manufacturing of Polypropylene. **2020**, *35*, 101384. https://doi.org/10.1016/j.addma.2020.101384.
(244) Wang, L.; Gardner, D. J. Effect of Fused Layer Modeling (FLM) Processing Parameters on Impact Strength of Cellular Polypropylene. *Polymer* **2017**, *113*, 74–80. https://doi.org/10.1016/j.polymer.2017.02.055.
(245) Qi, S.; Gao, X.; Su, Y.; Dong, X.; Cavallo, D.; Wang, D. Correlation between Welding Behavior and Mechanical Anisotropy of Long Chain Polyamide 12 Manufactured with Fused Filament Fabrication. *Polymer* **2021**, *213*, 123318. https://doi.org/10.1016/j.polymer.2020.123318.
(246) Zhou, Y.-G.; Zou, J.-R.; Wu, H.-H.; Xu, B.-P. Balance between Bonding and Deposition during Fused Deposition Modeling of Polycarbonate and Acrylonitrile-Butadiene-Styrene Composites. *Polym. Compos.* **2020**, *41* (1), 60–72. https://doi.org/10.1002/pc.25345.
(247) Mileva, D.; Kolesov, I.; Androsch, R. Morphology of Cold-Crystallized Polyamide 6. *Colloid Polym. Sci.* **2012**, *290* (10), 971–978. https://doi.org/10.1007/s00396-012-2657-3.
(248) Clough, S.; Van Aartsen, J. J.; Stein, R. S. Scattering of Light by Two-Dimensional Spherulites. *J. Appl. Phys.* **1965**, *36* (10), 3072–3085. https://doi.org/10.1063/1.1702929.
(249) Vaes, D.; Coppens, M.; Goderis, B.; Zoetelief, W.; Van Puyvelde, P. Assessment of Crystallinity Development during Fused Filament Fabrication through Fast Scanning Chip Calorimetry. *Appl. Sci.* **2019**, *9* (13). https://doi.org/10.3390/app9132676.

Publications

1. Costanzo, A.; Spotorno, R.; Candal, M.V.; Fernández, M.M,; Müller, A.J.; Graham, R.S.; Cavallo, D.; McIlroy, C. Residual alignment and its effect on weld strength in material-extrusion 3D-printing of polylactic acid, *Addit. Manuf.*, **2020**, 36, 101415, DOI 10.1016/j.addma.2020.101415
2. Costanzo, A.; Croce, U.; Spotorno, R.; Fenni, S.E.; Cavallo, D. Fused Deposition Modeling of Polyamides: Crystallization and Weld Formation, *Polymers*, **2020**, 12(12), 2980, DOI doi.org/10.3390/polym12122980
3. Costanzo, A.; Spotorno, R.; Lova, P.; Smerieri, M.; Carraro, G.; Cavallo, D. Light scattering approach to the in situ measurement of polymer crystallization during 3D printing: A feasibility study, *Polym. Cryst.*, **2021**, 4, DOI doi.org/10.1002/pcr2.10182
4. Costanzo, A.; Cavallo, D.; McIlroy, C. High-performance co-polyesters for material-extrusion 3D printing: A molecular perspective of weld properties, *Addit. Manuf.*, **2022**, 49, 102474, DOI doi.org/10.1016/j.addma.2021.102474
5. Costanzo, A.; Poggi, A.; Looijmans, S.; Venkatraman, D.; Sawyer, D.; Puskar, L.; McIlroy, C.; Cavallo, D. The Role of Molar Mass in Achieving isotropy and Inter-Layer Strength in Mat-Ex Printed Polylactic Acid, *Polymers*, **2022**, 14(14), 2792, DOI doi.org/10.3390/polym14142792
6. Fenni, S.E.; Spigno, M.; Wang, W.; Costanzo, A.; Müller, A.J.; Cavallo, D. How nucleating particles migration affects the fractionated crystallization of isotactic polypropylene/polystyrene immiscible blends, *Thermochim. Acta*, **2023**, 719, 179407, DOI https://doi.org/10.1016/j.tca.2022.179407

Acknowledgments

"Here we go", come direbbe Fabrizio Romano, famoso giornalista sportivo esperto di calciomercato. Perché si, ormai siamo davvero arrivati alla fine di questo percorso che ho deciso di intraprendere proprio in *"zona Cesarini"* ma che, alla fine, mi ha permesso di arricchire profondamente il mio bagaglio scientifico-professionale e soprattutto umano.
Tra gli esperimenti per la tesi di Laurea Magistrale e quelli per il progetto di dottorato i cui risultati sono presentati in questo manoscritto, ho trascorso quasi 5 anni all'interno del gruppo dei polimeri semicristallini al Dipartimento di Chimica dell'Università di Genova, un periodo temporale talmente lungo e intenso tale da risultare faticoso ricordare tutte le circostanze che lo meriterebbero.
Posso dire, però, con assoluta certezza che molte delle soddisfazioni e dei traguardi che sono riuscito a raggiungere in questo cammino non sarebbero stati possibili senza il supporto di altre figure, motivo per il quale queste meritano una menzione speciale.

In primo luogo, vorrei ringraziare il Prof., e ormai amico, Dario Cavallo, per avermi dato la possibilità di svolgere questo dottorato sotto la sua supervisione (e finanziamento), ma soprattutto per il grande rispetto e stima sempre mostrati nei miei confronti. Farò per sempre tesoro di ogni suo consiglio e insegnamento riguardo ai materiali polimerici e non solo.

Ringrazio poi voi, i miei genitori, Susanna e Daniele. Senza i vostri sacrifici non sarebbe stato possibile intraprendere il cammino universitario e, conseguentemente, poter iniziare questo dottorato di ricerca. Vi sono grato per il vostro sostegno continuo, fatto di consolazioni a seguito di delusioni e momenti di stress e soprattutto di continuo incoraggiamento a dare sempre il massimo, in ogni occasione.

La mia gratitudine va ovviamente anche a tutte le persone che ho conosciuto e con le quali ho lavorato in questi anni. A tutti i professori, quali Roberto Spotorno e Davide Comoretto; ai colleghi dottorandi e post-doc Seif, Enrico, Magdalena e Wei; ai tecnici di laboratorio, quali Fiorenza, Roberto, Federico e Omar; agli studenti che ho affiancato nello svolgimento del tirocinio per la stesura della tesi di Laurea, Umberto e Alice; e infine, a tutti gli altri ragazzi che sono entrati a far parte del nostro splendido gruppo.

Una menzione speciale va alla ricercatrice Claire McIlroy, docente presso la Scuola di Matematica e Fisica all'università di Lincoln, con la quale abbiamo portato a termine diversi progetti a seguito di una genuina collaborazione.

Vorrei poi ringraziare tutte le persone che mi hanno accompagnato nel mio soggiorno a San Sebastián, dai professori Alejandro Müller, Roberto Hernandez e Itxaso Calafel, a tutti gli amici, connazionali e non, che ho incontrato sul posto: Maria Rosaria, Rino, Alessandra, Massimo, Enrique, Nicolas Maria, Sebastian, Jorge, Valentina e Alessio. Mi avete fatto sentire subito a casa, nonostante ne fossi parecchio distante.

E infine, ma non per importanza, ringrazio te, Erika. Sei entrata nella mia vita inaspettatamente come un fulmine a ciel sereno e hai stravolto il mio modo di vedere anche le piccole cose. Grazie per la infinita fiducia che mostri in me e per spronarmi continuamente a credere maggiormente in me stesso. Sei un bene prezioso, ti amo.